AWI Alfred-Wegener-Institut
für Polar- und Meeresforschung
in der Helmholtz-Gemeinschaft

A global Finite-Element Sea-Ice ocean model focussed on deep water formation areas: Variability of North Atlantic deep water formation and interannual to decadal climate modes

DISSERTATION
zur Erlangung des akademischen Grades eines
Doktor der Naturwissenschaften
— Dr. rer. nat. —

Vom Fachbereich für Physik und Elektrotechnik,
Universität Bremen

von

Patrick Scholz

1. Gutachter: Prof. Dr. Gerrit Lohmann

2. Gutachter: Prof. Dr. Monica Rhein

Eingereicht am: 14.06.2012

AWI Alfred-Wegener-Institut
für Polar- und Meeresforschung
in der Helmholtz-Gemeinschaft

Erklärung

Hiermit versichere ich, dass ich die vorliegende Arbeit selbstständig verfasst und keine anderen als die angegebenen Quellen und Hilfsmittel benutzt habe, dass alle Stellen der Arbeit, die wörtlich oder sinngemäß aus anderen Quellen übernommen wurden, als solche kenntlich gemacht sind und dass die Arbeit in gleicher oder ähnlicher Form noch keiner Prüfungsbehörde vorgelegt wurde.

Bremerhaven, den June 13, 2012 .....

AWI Alfred-Wegener-Institut
für Polar- und Meeresforschung
in der Helmholtz-Gemeinschaft

Zusammenfassung

Das Verständnis für die Ursache der Schwankungen in der Tiefenwasserbildung im Nordatlantik ist von entscheidender Bedeutung für die allgemeine globale Ozean Variabilität besonders im Hinblick auf zwischenjährliche bis dekadische Zeitskalen. Die starke regionale Begrenzung der Tiefenwasserbildungsgebiete erfordert die Erprobung neuer Modellansätze, die es ermöglichen lokale Gebiete hinreichend genau aufzulösen, ohne die globalen Zusammenhänge aus den Augen zu verlieren. Ziel dieser Arbeit ist es festzustellen, ob das "Finite-Element Sea-Ice Ocean Model" (FESOM) geeignet ist, eine verlässliche Tiefenwasserbildung im Nordatlantik zu simulieren, sowie die allgemeine Modellvariabilität auf zwischenjährlichen bis dekadischen Zeitskalen zu untersuchen.

Im ersten Teil der Dissertation werden die Eigenschaften des verwendeten globalen FESOM Setups vorgestellt. Dieses Setup wurde speziell dazu entworfen, die Variabilitäten in der Tiefenwasserbildung über den Zeitraum von 1958-2004 zu studieren. Die Modellkonfiguration hat eine regional erhöhte Auflösung in den Tiefenwasserbildungsgebieten Labrador See, Grönland See, Weddell See und Ross See sowie in Küstengebieten und äquatorialen Breiten. Dieser Teil der Dissertation beschreibt außerdem das verwendete Spinup-Verfahren sowie die allgemeine Validierung des Modells in Bezug auf die Meereis- und Ozean-Modellkomponenten. Basierend auf der Analyse der Umwälzrate der Atlantischen Zirkulation (AMOC: Atlantic Meridional Overturning Circulation) zeigen wir, dass der obere Ozean innerhalb des verwendeten Spinup-Verfahrens konvergiert ist. Das Meereismodell liefert sowohl auf der nördlichen als auch auf der südlichen Hemisphäre eine realistische Meereisbedeckung und eine mit Beobachtungsdaten vergleichbare Variabilität. Durch einen Vergleich der Modellergebnisse mit Beobachtungsdaten von Ozean-Wetter-Schiffen im Nordatlantik können wir zeigen, daß das Ozeanmodell in der Lage ist, die vertikale Struktur besonders in den hoch aufgelösten Gebieten wiederzugeben. Außerdem sind wir im Stande, dekadische Schwankungen im Überlauf der Dänemark Straße und des Island-Schottland-Kamms zu simulieren sowie verschiedene "Große Salzanomalien" und deren vertikale Hydrographie zu reproduzieren.

Der zweite Teil der Dissertation konzentriert sich auf die Validierung des Modells im Hinblick auf eine realistische Tiefenwasserbildung in der Labrador See. Dazu wurden

zwei Klassen von Labrador See Wasser (LSW) untersucht und mit LSW Schichtdicken aus Beobachtungszeitreihen für den Zeitraum 1988-2007 verglichen. Die simulierte zeitliche Entwicklung der potentiellen Dichte, der Temperatur und des Salzgehalts hat in der zentralen Labrador See seit den späten 1980er Jahren zwei unterschiedliche Phasen, welche sich durch eine unterschiedliche LSW Bildung auszeichnen. Die erste Phase ist durch eine verstärkte Bildung des tiefen Labrador See Wassers (dLSW: deep Labrador Sea Water) charakterisiert, wohingegen die zweite Phase durch den Abbau und die verminderte Produktion von dLSW bestimmt wird. Um die Prozesse zu verdeutlichen, die für die simulierte Schwankung der dLSW Schichtdicke verantwortlich sind, verwenden wir "Composite Maps" (CMA) des Meeresspiegeldrucks sowie der thermalen und halinen Anteile des Oberflächendichteflusses. Die "Composite Maps" bestätigen, dass ein atmosphärisches Druckmuster, welches der Nordatlantischen Oszillation (NAO) ähnlich ist einer der Hauptauslöser für die Schwankungen in der simulierten dLSW Schichtdicke ist. Unsere Modellergebnisse deuten darauf hin, dass eine massive dLSW Bildung, als Tiefpassfilter im Hinblick auf den atmosphärischen Antrieb wirken kann, so dass nur anhaltende NAO Ereignisse mit dem dLSW Index korrelieren. Zusätzlich zeigen unsere Ergebnisse, dass die zentrale Labrador See in unserem Modell durch die thermalen Anteile des Oberflächendichteflusses bestimmt wird, wohingegen die halinen Anteile des Oberflächendichteflusses in unserem Modell durch das Randstromsystem der Labrador See von der zentralen Labrador See abgeschirmt werden.

Ein weiteres Ziel dieser Dissertation ist die Untersuchung der allgemeinen Variabilitäten eines normal und eines stochastisch angetriebenen FESOM Modelllaufs im Hinblick auf zwischenjährliche bis dekadische Zeitskalen. Durch die spektrale Analyse des Nordatlantischen Tiefenwasser (NADW: North Atlantic Deep Water) Index für den normal und stochastisch angetriebenen Modelllauf konnten wir eine zwischenjährliche Variabilität von 7.1 Jahren und eine quasi-dekadische Variabilität von 14.2 Jahren identifizieren. Dabei konnten wir feststellen, dass der normal angetriebene Modelllauf durch die quasi-dekadische Variabilität dominiert wird, die dem atmosphärischen Forcing zugeordnet werden konnte, wohingegen der stochastisch angetriebene Modelllauf durch zwischenjährliche Variabilität bestimmt wird, die mit internen Moden des Ozeans verbunden ist. In Analogie zum "baroclinic mass transport index" (BMT) Index definieren wir einen $\Delta Gyre$ Index basierend auf der horizontalen Stromfunktion. Der Vergleich von BMT Index und simulierten $\Delta Gyre$ hat gezeigt, dass das Modell im Stande ist, die Variabilität des BMT Index zu reproduzieren, obgleich das Modell dazu tendiert, die Magnitude des BMT Index zu überschätzen. Um die horizontalen und vertikalen Variabilitätsmuster im Modell eingehender zu untersuchen, verwenden wir eine dreidimensionale "Principal Oscillation Pattern" (POP) Analyse. Dabei wurden zwei außerordentlich stabile zwischenjährliche Moden gefunden deren Variabilitäten propagierenden Rossby Wellen zugeordnet werden konnte.

AWI Alfred-Wegener-Institut
für Polar- und Meeresforschung
in der Helmholtz-Gemeinschaft

Abstract

The modeling and understanding of the deep-water formation variability, especially in the North Atlantic sector, is of crucial importance for the common global ocean variability, in particular on interannual to decadal time-scales. The local restriction of the deep water formation areas makes it necessary to follow new model approaches that are able to resolve these areas with a sufficient high resolution without ignoring the global context. This study aims to validate the ability of the Finite-Element Sea-Ice Ocean Model (FESOM) to reproduce a reliable deep water formation in North Atlantic ocean and to analyse its variability on interannual to decadal time-scales. The FESOM approach works on unstructured triangular surface meshes, which allows us to faithfully resolve coastlines and local areas of interest.

The first part of the thesis presents the characteristics of a global FESOM setup designed to study the variability in the deep-water formation areas over five decades for the period 1958-2004. The setup features a regionally increased resolution in the deep water formation areas in the Labrador Sea, Greenland Sea, Weddell Sea and Ross Sea as well as in equatorial and coastal areas. Further, this part of the thesis deals with the applied spinup procedure and the general validation of the FESOM model setup with respect to the performance of the sea-ice and ocean model component. Based on the analysis of the Atlantic Meridional Overturning Circulation (AMOC) we demonstrate that the upper ocean is converged within the applied spinup procedure. The sea ice model reproduces realistic sea-ice distributions and variabilities in the sea ice extent on both hemispheres as well as sea ice transport that compares well with observational data. The general ocean circulation model is validated based on a comparison of the model results with Ocean Weather Ship data in the North Atlantic. We can prove that the vertical structure is well captured in areas with improved resolution. Further, we are able to simulate the decadal ocean variability in the Nordic Sea Overflows as well as several salinity anomaly events and corresponding fingerprint in the vertical hydrography.

The second part of the thesis focuses on the validation of the model capability to reproduce a realistic deep-water formation in the Labrador Sea. Therefor, we examine

two classes of Labrador Sea water (LSW) which are analysed and compared to observed LSW layer thicknesses derived from profile data for the time interval 1988-2007. We show, that the model setup reproduces in the temporal evolution of the potential density, temperature and salinity two different phase since the late 1980s. These two phases are well known in observational data and are characterized by a significantly different LSW formation. Whereas the first phase features a dominant increase in the layer thickness of the deep Labrador Sea water (dLSW), is the second phase characterized by a degeneration of dLSW. To highlight the processes that are responsible for the variability in dLSW layer thickness we apply a Composite Map Analysis (CMA) between an index of dLSW and sea level pressure, as well as the thermal and haline contributions to the surface density flux. The composite maps reveal that a North Atlantic Oscillation like pattern is one of the main triggers for the variability of LSW formation in the model. Our model results indicate that a massive dLSW formation can act as a low-pass filter to the atmospheric forcing, so that only persistent NAO events correlate with the dLSW index. Additionally our results show that the central Labrador Sea in the model is dominated by the thermal contributions of the surface density flux, while the haline contributions are shielded from the central Labrador Sea by the branch of the Labrador Sea Boundary Current system. In our model, this shielding allows only a minor haline interaction with the central Labrador Sea by lateral mixing.

Another aim of the thesis is to examine the general model variability on interannual to decadal time scales. Therefore we study the variability in a normal and random forced FESOM run. By definition of a North Atlantic Deep Water (NADW) index for the normal and random forced FESOM run we could identify an interannual and quasi decadal variability of 7.1 yr and 14.2 yr, respectively. It is found that the normal forced run is dominated by the quasi decadal variability and the random forced run by the interannual variability. The quasi decadal variability could be attributed to the atmospheric forcing, while the interannual variability could be linked to internal modes of the ocean. We defined in analogy to the baroclinic mass transport index (BMT) a $\Delta Gyre$ from the horizontal barotropic streamfunction. The comparison of the observed BMT index and the modeled $\Delta Gyre$ index reveals that the model is able to reproduce the variability of the index comparing to the observed one, although the model tends to overestimate the magnitude of the index. To further isolate the horizontal but also the vertical variability in the model we apply a principal oscillation pattern (POP) analysis in a three dimensional context. We discovered two exceptional strong interannual modes whose variability could be attributed to a propagating Rossby wave structure.

AWI Alfred-Wegener-Institut für Polar- und Meeresforschung in der Helmholtz-Gemeinschaft

Contents

AWI Alfred-Wegener-Institut für Polar- und Meeresforschung in der Helmholtz-Gemeinschaft

1 Introduction

The understanding of the complex earth climate system is essential for the prediction of the future climate evolution. The key components that influence the earth climate are the atmosphere and the world ocean. The atmosphere influences the climate mainly on short time-scales, while the surface ocean influences the climate on time-scales of decades to centuries. The deeper layers of the ocean can even respond on millennial time-scales [*Gill*, 1982]. The world oceans are the largest reservoir for heat and freshwater. The local heat content of the ocean mainly changes due to heating and cooling with the overlying atmospheric surface layers. The local freshwater content increases due to precipitation, river runoff and sea-ice melting and decreases due to evaporation and sea-ice formation [*Stewart*, 2008]. The aforementioned mechanisms change the local water mass properties to higher or lower densities. These local differences in the water mass properties can than further advect and redistribute with the large-scale ocean circulation which makes the response of ocean and atmosphere to a non-local effect.

The concept of the global oceanic Meridional Overturning Circulation (MOC) also referred as the "global conveyor belt circulation" [*Broecker*, 1991] connects the basin wide large-scale oceanic circulation of the Atlantic, Indian, Pacific and Southern Oceans to each other. The MOC is characterized in general by wind-driven, thermohaline-driven and mixing-driven upwelling which exchange waters between deep and surface ocean. Subsequently light surface waters are transported by surface currents into high latitudes. In certain deep water formation areas, the surface waters lose their buoyancy due to intensified cooling and ventilates downward by deep water formation. These dense and cold water masses are then advected by deep ocean currents towards lower latitudes which closes the loop of the overturning circulation [*Kuhlbrodt et al.*, 2007].

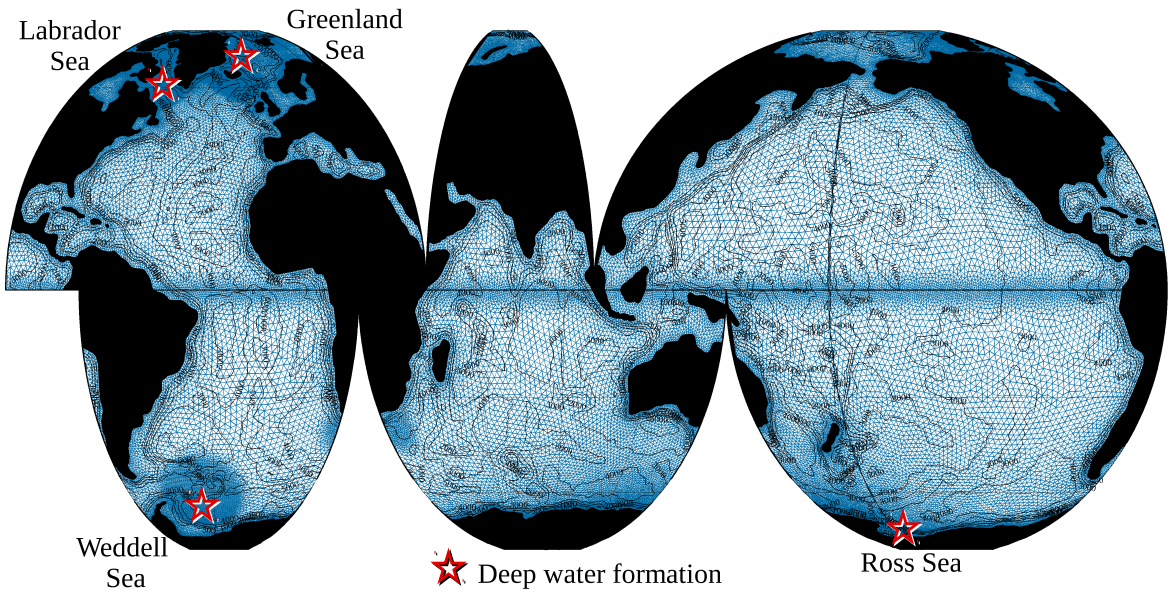

Fig. 1.1: *Unstructured triangular surface mesh of the Finite-Element Sea-Ice Ocean Model (FESOM) setup used in this work. Northern hemispheric (e.g. Labrador Sea, Greenland Sea) and southern hemispheric (e.g. Weddell Sea, Ross Sea) deep water formation areas are highlighted by red stars.*

The conditions to favour high latitude deep convection, exists only in a few unique locations of the world ocean. In the Southern Hemisphere, deep water formation mainly occurs close to the Antarctic continental shelf in the Weddell Sea and Ross Sea (Fig.1.1). There the Antarctic Bottom Water (AABW) is formed which is the deepest and densest water mass that spreads northward along the abyssal ocean or recirculates in the system of the Antarctic Circumpolar Current (ACC). In the Northern Hemisphere deep water formation occurs only in the North Atlantic Ocean, where the overturning circulation can be described in terms of the Atlantic Meridional Overturning Circulation (AMOC). The AMOC is characterized by the transport of warm and saline waters from the equatorial Atlantic into northern latitudes by the Western Boundary current, the Gulf Stream current and the North Atlantic current. Europe owes its mild climate to the large quantities of heat that these currents transport to the northeast [e.g., *Rahmsdorf*, 1996; *Broecker*, 1997]. The northern branch of the AMOC features the formation of dense and cold North Atlantic Deep Water (NADW). The unique conditions that

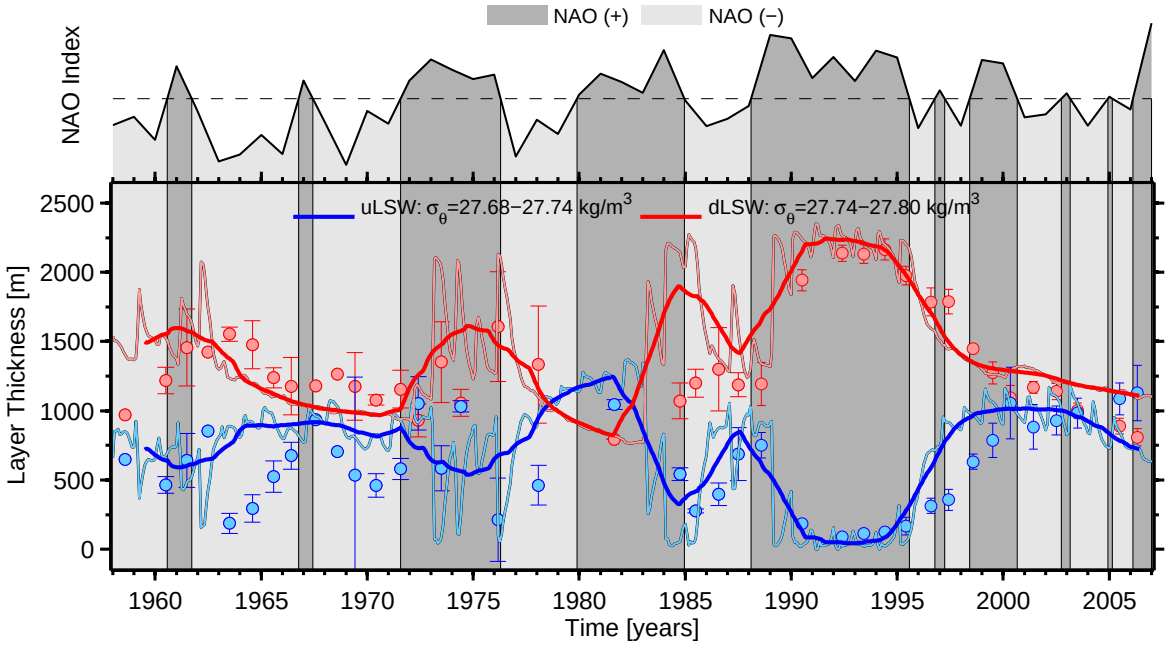

Fig. 1.2: *Five decades of monthly (thin lines) and 3-years-running-mean filtered (thick lines) layer thickness variability in the upper LSW (uLSW) and deep LSW (dLSW) simulated with the FESOM setup used in this study. Red: dLSW, blue: uLSW. The dLSW and uLSW layer thickness time series derived from observations are shown as filled circles including the uncertainties [Curry et al., 1998; Rhein et al., 2011]. The positive and negative phase of the normalized winter NAO index [Hurrell, 1995] derived from the COREv2 data set [Large and Yeager, 2009] are superimposed by dark- and light grey areas, respectively.*

favour the formation of NADW are only present in a few locations of the northern and subpolar Atlantic Ocean. The deepest and densest water mass in the branch of the AMOC is the AABW which enters the Atlantic from the Southern Ocean.

The deep branch of the NADW is fed by deep water formation in the Nordic Seas consisting of Greenland Sea, Iceland Sea and Norwegian Sea (GIN). This part of the NADW spreads over the Greenland-Scotland ridge and forms the dense overflow waters of the Denmark Strait Overflow (DSOW) and Island-Scotland Overflow (ISOW) that spills into the abyssal plain of the North Atlantic Ocean [*Dickson and Brown*, 1994].

The intermediate branch of the NADW is mainly formed by deep convection in the

central Labrador Sea. The most prominent water mass that is part of this deep convection process is the Labrador Sea Water (LSW), which can be separated into the lighter branch of the upper LSW and the denser branch of the deep LSW (dLSW), which is also referred as "classical LSW" [*Rhein et al.*, 2002; *Pickart et al.*, 2002; *Stramma et al.*, 2004]. Both LSW water masses are formed by intense winter deep convection, which is induced by the severe cooling of the surface waters due to strong surface winds over the Labrador Sea that are fed by a cyclonic atmospheric circulation that brings very cold air from the Canadian Archipelago. The severe surface heat loss leads to a increase in the near surface density which is accompanied by a loss of surface buoyancy. This breaks up the weak density stratification and initiates the sinking of cold and dense waters, which produces a homogeneous and thick LSW layer. The fact whether uLSW or dLSW is formed depends on the intensity of the deep convection and density stratification that was build up in the preceding winters [*Yashayaev*, 2007]. This decides how much buoyancy forcing is necessary to form water of a certain density and thus whether the uLSW or dLSW body is feed from the deep ventilation (Fig. 1.2).
The North Atlantic sector is strongly influenced by the variability of the westerly wind system [*Curry and McCartney*, 2001]. The intensity of the westerlies can be described in terms of the North Atlantic Oscillation (NAO) (Fig. 1.2). This dominant atmospheric mode over the Northern Hemisphere, refers to an oscillation in the atmospheric Azores High and Icelandic Low pressure centers [*Walker and Bliss*, 1932; *Hurrell*, 1995]. During positive NAO, westerlies are stronger than normal and their flow is shifted towards north above the North Atlantic ocean which brings colder temperature with it over the eastern North Atlantic Ocean. This leads to an increased take out of heat in the Labrador Sea by sensible heat flux and favors the vertical ventilation of the ocean. Knowing about trends and variabilities of the large-scale ocean circulation and their response to changing external influences is essential for the understanding of the climate system and for the prediction of how future climate will develop. The identification and understanding of relevant climate modes on human timescales, that means interannual to decadal or even centennial timescales, that are responsible for the observed variabilities is an ongoing topic. Different modes of climate variability have been identified by [e.g., *Deser and Blackmon*, 1993; *Mann and Park*, 1994; *Dima and Lohmann*, 2004] using stochastic climate models introduced by *Hasselmann* [1988] and *von Storch et al.*

[1995].

The identification of important climate modes in observational data can be difficult because the spatial and temporal coverage of observational hydrographic data in many regions of the world ocean is rather sparse. Further, observational data are often superimposed by measurement errors, signals from wave processes and tides. Especially the limited temporal coverage of hydrographic data complicates the identification of climate mode variability in observational hydrographic data. One of the longest hydrographic records in the subpolar North Atlantic is carried out by the Ocean Weather Ship (OWS) program. These records contain long term observations in the vertical structure of the ocean at isolated locations in the North Atlantic since the late 1920s until the early 1990s, so provides the OWS-B in the central Labrador Sea, temperature and salinity time-series for the interval 1964-1974 [*Lazier*, 1980; *Levitus et al.*, 1994].

Numerical ocean models provide the capability to overcome the spatial and temporal limitations of observational data and to simulate the general ocean circulation based on a set of simplified equations and parametrizations to substitute processes that can not be resolved by the model discretisation. Due to the progress in numerical modeling the community is able to model the ocean on very high resolutions. There are a series of regional model studies [e.g., *Böning et al.*, 1996; *Chanut et al.*, 2008] that simulate particular areas of the subpolar North Atlantic on a eddy resolving resolution. However, global high resolution modeling on a conventional regular Finite-Difference discretisation [*Bryan and Cox*, 1972; *Arakawa and Lamb*, 1977] is rather difficult due to the necessity of complicated grid nesting methods and high numerical costs. At this point new numerical model approaches that are based on the Finite-Element (FE) method which follow the early work of *Fix* [1975] provide an alternative. The FE method provides an easy conservation of energy and a natural treatment of geometric boundaries [*Danilov et al.*, 2004; *Timmermann et al.*, 2009] and works on unstructured triangular meshes that have the capability to faithfully resolve coastlines and to highly resolve areas of interest without losing the global context of a model setup. So far, there have been only a few Finite-Element general ocean circulation models developed that employ the capability of unstructured meshes (Fig. 1.1) and that are able to reproduce the large-scale ocean circulation in a global framework [*Danilov et al.*, 2004; *Ford et al.*, 2004; *White et al.*, 2008]. In this thesis we use the Finite-Element Sea-Ice

Ocean Model (FESOM) developed at the Alfred Wegener Institute for Polar and Marine Research [*Danilov et al.*, 2004, 2005; *Wang et al.*, 2008a; *Timmermann et al.*, 2009], which is an ocean general circulation model based on solving the primitive equations under Boussinesq approximation coupled to a dynamic thermodynamic sea-ice model. FESOM was successfully used in a regional model study on the tidal impacts of the overflow dynamics and bottom water formation in the Ross Sea by *Wang et al.* [2008b]. Further, FESOM proved its capability to simulate a large-scale ocean circulation that is comparable with other Ocean General Circulation Models (OGCM) [*Griffies et al.*, 2009; *Sidorenko et al.*, 2011].

Content of the thesis

The structure of the thesis is organized in 4 main chapters 4-7, besides the general introduction (chapter 1), methodology (chapters 2-3) and the conclusions and future perspectives (chapter 8).

Chapter 2:
Chapter 2 introduces the general ocean model equations and the Finite-Element discretisation. Additionally, this chapter presents the model setup specially created for the purpose of this thesis as well as the applied forcing setups and the spinup procedure.

Chapter 3:
Chapter 3 describes the multivariante stochastical analysis method of the principal oscillation pattern (POPs) analysis which find its application in chapter 7, as well as the expansion in empirical orthogonal functions (EOFs) to reduce the degrees of freedom of a space-time system.

Chapter 4 and 5:
Chapter 4 validates the ability of the sea-ice model to reproduce a reliable sea-ice cover and variability. Further the ocean model is validated 5 in chapter based on a comparison with ocean weather ship data. We show the ability of the model to reproduce Great Salinity Anomaly (GSA) events and the temperature and salinity evolution of

the Nordic Sea overflows. At the end of chapter 5 some first variability that the model generates is analysed.[1]

Chapter 6:

Chapter 6 validates the performance of the global FESOM setup to reproduce a realistic deep water formation in the central Labrador Sea. For this purpose we identify the modelled location of the main deep convection cell in the Labrador Sea and examine the dynamics of the model LSW index. We analyse the evolution of the potential density, temperature and salinity over depth and time and the simulated variability in the layer thickness of uLSW and dLSW. To validate our results we compare the evolution of the modelled LSW layer thicknesses to time-series of LSW layer thicknesses derived from hydrographic observations from the central Labrador Sea. In addition, we highlight the atmospheric processes in our model that are responsible for the fluctuation in the formation of dLSW and analyse the thermal and haline surface density flux and their contributions to the model deep water formation using composite map analysis.

Chapter 7:

The aim of chapter 7 is to analyse the underlying model variability on interannual to decadal time-scales. For this purpose we employ a realistic (normal) sea surface forcing to analyse the variability of the North Atlantic gyre circulation as well as the response time to the NAO. To distinguish the underlying variability (if it refers to the atmospheric forcing or to the internal modes of the ocean) we employ a further model run under random forcing condition. Based on the time evolution of the normal and random forced NADW index and their corresponding spectra we are able to assign different interannual to decadal variabilities to the atmosphere and internal ocean modes. By use of a principal oscillation pattern (POP) analysis that is applied to a three dimensional temperature field in the North Atlantic Ocean we are able to isolate horizontally but also vertically, propagating patterns of exceptional stable oscillatory modes in the North Atlantic Ocean.

[1] A great part of these chapters is identical to a publication of *Scholz et al.* [submitted, 2012] which is submitted to the journal "Ocean Dynamics".

AWI Alfred-Wegener-Institut für Polar- und Meeresforschung in der Helmholtz-Gemeinschaft

2 Finite-Element Sea-Ice Ocean Model (FESOM) description and experimental setup

The FESOM model, developed at the Alfred Wegener Institute for Polar and Marine Research [*Danilov et al.*, 2004, 2005; *Wang et al.*, 2008a] is a new approach to simulate the global ocean circulation. The model consists of the Finite-Element ocean model (FEOM) and a Finite-Element dynamic thermodynamic Sea-Ice Model [*Timmermann et al.*, 2009]. The current version of FEOM does not differ significantly from the numerical principals described by *Wang et al.* [2008a], except that tetrahedral discretization instead of prismatic is used. The numerical core of the sea-ice model is described in detail by *Timmermann et al.* [2009].

2.1 FEOM model description

2.1.1 Basic equations

For the introduction of the basic model equations we follow here the explanations of *Danilov et al.* [2004], who first introduced the numerical core of the Finite-Element Ocean Model (FEOM) as well as the description of *Wang et al.* [2008a]. The governing equations in the model are split into two subsets, which are solved separately. This avoids the simultaneous treatment of non-linear dynamics and thermodynamics. The first subset that is to solve is the dynamical part, which consist of solving the momentum

equation and the integral continuity equation:

$$\partial_t \mathbf{u} + \mathbf{v} \cdot \nabla_3 \mathbf{u} + f\mathbf{k} \times \mathbf{u} = -\frac{1}{\rho_0}\nabla p - g\nabla\eta + \nabla \cdot A_h \nabla \mathbf{u} + \partial_z A_\nu \partial_z \mathbf{u} \tag{2.1}$$

$$\partial_t \eta + \nabla \cdot \int_{z=-H}^{\eta} \mathbf{u}\, dz = 0 \tag{2.2}$$

$$\partial_z p = -g\rho \tag{2.3}$$

where $\mathbf{v} \equiv (\mathbf{u},\ w) \equiv (u\ , v\ ,\ w)$ is the velocity in the spherical coordinate system, ρ_0 and ρ are the density and the deviation from the mean density. p is the hydrostatic (baroclinic pressure) estimated by integrating the hydrostatic relation from $z = 0$. η is the sea surface elevation, $\mathbf{k}$ is the vertical unit vector and f is the Coriolis parameter. $A_h,\ A_\nu$ are the lateral and vertical viscosities (vertical momentum diffusion coefficients) and g is the gravitational acceleration. ∇_3, ∇ are the 3D and 2D divergence operators, respectively.

The physical domain Ω on which the model (eqs. 2.1-2.3) is solved can contain four types of boundaries $\partial\Omega = \bigcup_{i=1}^{4} \Gamma_i$, where: $\Gamma_1 : \{z = 0\}$ is the ocean surface, $\Gamma_2 : \{z = -H\}$ is the ocean bottom, Γ_3 are the vertical rigid walls and Γ_4 stands for the vertical open boundary. The boundary conditions on Γ_1, Γ_2 and Γ_3 are:

$$A_\nu \partial_z \mathbf{u} = \tau,\ p = 0 \text{ on } \Gamma_1 \tag{2.4}$$

$$A_\nu \partial_z \mathbf{u} + A_h \nabla H \cdot \nabla \mathbf{u} = C_d \mathbf{u}|\mathbf{u}| \text{ on } \Gamma_2 \tag{2.5}$$

$$\mathbf{u} \cdot \mathbf{n} = 0, \quad \text{on } \Gamma_3 \tag{2.6}$$

where τ is the wind stress, C_d is the bottom drag coefficient and $\mathbf{n}$ is the 2D normal unit vector, respectively

The vertical velocity is derived from the continuity equation

$$\partial_z w = -\nabla \cdot \mathbf{u} \tag{2.7}$$

with the corresponding kinematic surface and bottom boundary conditions:

$$w = \partial_t \eta \text{ or } w = 0 \text{ on } \Gamma_1 \tag{2.8}$$

$$w = -\nabla H \cdot \mathbf{u} \text{ on } \Gamma_2 \tag{2.9}$$

The thermodynamical part of the model solves the tracer equations for potential temperature T and salinity S as well as the density ρ which is computed via the equation of state.

$$\partial_t T + \mathbf{v} \cdot \nabla_3 T - \nabla \cdot K_h \nabla T - \partial_z K_v \partial_z T = 0 \tag{2.10}$$

$$\partial_t S + \mathbf{v} \cdot \nabla_3 S - \nabla \cdot K_h \nabla S - \partial_z K_v \partial_z S = 0 \tag{2.11}$$

$$\rho = \rho(T, S, p) \tag{2.12}$$

where K_h, K_v are the lateral and vertical diffusion coefficients. The tracer fulfill the boundary conditions:

$$K_v \partial_z T = -q_T, \; K_v \partial_z S = -q_S \text{ on } \Gamma_1 \tag{2.13}$$

$$(\nabla T, \partial_z T) \cdot \mathbf{n_3} = 0, \; (\nabla S, \partial_z S) \cdot \mathbf{n_3} = 0 \text{ on } \Gamma_2 \cup \Gamma_3 \tag{2.14}$$

where q_T, q_S are the surface fluxes for T and S, respectively. $\mathbf{n_3}$ is the 3D unit vector normal to the respective surface.

2.1.2 Finite-Element discretisation

The model uses tetrahedral elements for spatial discretisation of the functional domain as well as linear basis functions for $\mathbf{u}$, η, p, T and S. The tetrahedral elements are derived by vertical expansion of the surface into prisms, where each prism is divided into three tetrahedral.

The linear basis functions used in this model are not twice differentiable, which requires the reformulation of eqs. (2.1)- (2.6) and (2.7)- (2.14) in the weak sense. Therefor (2.1) and (2.2) are multiplied by an arbitrary vector field $\tilde{\mathbf{u}}$ and a scalar function $\tilde{\eta}$ that does not depend on z. By use of the Greens formula and the boundary conditions one of the double differentials is transferred to the arbitrary vector field $\tilde{\mathbf{u}}$ and we obtain for the

dynamical part:

$$\int_\Omega [(\partial_t \mathbf{u} + f[\mathbf{k}\times\mathbf{u}] + g\nabla\eta)\cdot\tilde{\mathbf{u}} + A_v\partial_z\mathbf{u}\cdot\partial_z\tilde{\mathbf{u}} + A_h\nabla\mathbf{u}\cdot\nabla\tilde{\mathbf{u}}]\, d\Omega$$
$$= -\int_\Omega [(\mathbf{u}\cdot\nabla + w\partial_z)\mathbf{u}]\cdot\tilde{\mathbf{u}}\, d\Omega - \int_\Omega \frac{1}{\rho_0}\tilde{\mathbf{u}}\cdot\nabla p\, d\Omega$$
$$+ \int_{\Gamma_1} \tau\cdot\tilde{\mathbf{u}}\, d\Gamma_1 - \int_{\Gamma_2} C_d\mathbf{u}|\mathbf{u}|\cdot\tilde{\mathbf{u}}\, d\Gamma_2 \tag{2.15}$$
$$\int_{\Gamma_1} \partial_t\eta\tilde{\eta}\, d\Gamma_1 - \int_\Omega \mathbf{u}\cdot\nabla\tilde{\eta}\, d\Omega = 0. \tag{2.16}$$

The eqs. (2.15)-(2.16) fulfil the solution of the original problem (eqs. (2.1)-(2.6)) for the case $\tilde{\mathbf{u}} = 0$ on Γ_3 where Dirichlet boundary conditions for the velocity $\mathbf{u}$ are imposed [*Danilov et al.*, 2004]. For the thermodynamical part where C stands for the tracers T and S follows the equations

$$\int_\Omega (\partial_t C\tilde{C} + (\mathbf{u}\cdot\nabla + w\partial_z)C\tilde{C} + K_h\nabla C\cdot\nabla\tilde{C} + K_v\partial_z T\partial_z\tilde{C})\, d\Omega = -\int_{\Gamma_1} q_C\tilde{C}\, d\Gamma_1 \tag{2.17}$$

The model variables $\mathbf{u}$, T and S are expressed as linear combinations of 3D linear basis function N_j:

$$\mathbf{u} \simeq \sum_{j=1}^{N_{3D}} (u_j,\ v_j)N_j\ ,\quad T \simeq \sum_{j=1}^{N_{3D}} T_j N_j\ ,\quad S \simeq \sum_{j=1}^{N_{3D}} S_j N_j \tag{2.18}$$

while the sea surface height η is represented using 2D linear basis functions M_j:

$$\eta \simeq \sum_{j=1}^{N_{2D}} \eta_j M_j \tag{2.19}$$

The linear basis function are equal to one at node j and go linearly to zero at neighboring nodes. After T and S are computed, the nodal values of ρ are computed from the equation of state. The nodal values of the pressure p are then derived from the hydrostatic equation that is considered in the FD sense and expressed by linear basis

functions:

$$\mathbf{p} \simeq \sum_{j=1}^{N_{3D}} p_j N_j \tag{2.20}$$

The solving of the first order problem for w requires the introduction of a vertical velocity potential Φ, that holds $w = \partial_z \Phi$. So the weak formulation of eq. (2.7) can be written as [*Danilov et al.*, 2004]

$$\int_\Omega \partial_z \Phi \partial_z \tilde{\Phi} \, d\Omega = -\int_\Omega \mathbf{u} \cdot \nabla \tilde{\Phi} \, d\Omega. \tag{2.21}$$

By computing Φ, w can be obtained as an elementwise constant function. Using this scheme for the continuity equation, conserves the volume only locally within a cluster of elements that share the same node (weighted with the test function defined at this node), and globally [*Danilov et al.*, 2004].
The further stability procedures of the model are described in detail in *Danilov et al.* [2004] and *Wang et al.* [2008a]. The FE method results in a system of linear equations that are obtain by the Galerkin method in conjunction with the Finite-Element discretisation. These linear equations are than solved by iterative solvers for the nodal values of u_j,v_j,η_j,T_j,S_j and w_j. The exact solving procedure of the dynamical equations and tracer equations are described by *Wang et al.* [2008a].

2.2 Description of global model setup

The setup that we created for our purpose includes an unstructured triangular surface mesh, which is shared by the ocean and sea-ice model. The vertical discretization employs a z level approach, where the mesh nodes are aligned under each other. This prevents difficulties in resolving the hydrostatic balance [*Danilov et al.*, 2004; *Sidorenko et al.*, 2011]. The combination of triangular surface mesh and the vertical alignment of nodes under each other creates at first prismatic volumes. Each of this prism is than split into 3 tetrahedral elements on which the model is working.
Fig. 2.1 shows the approximated mesh resolution used in this setup. The setup is configured on a longitude-latitude mesh, where the latitude coordinate is scaled with $\cos(\Theta)$ to provide a uniform triangular grid in polar areas. The mesh itself is rotated so

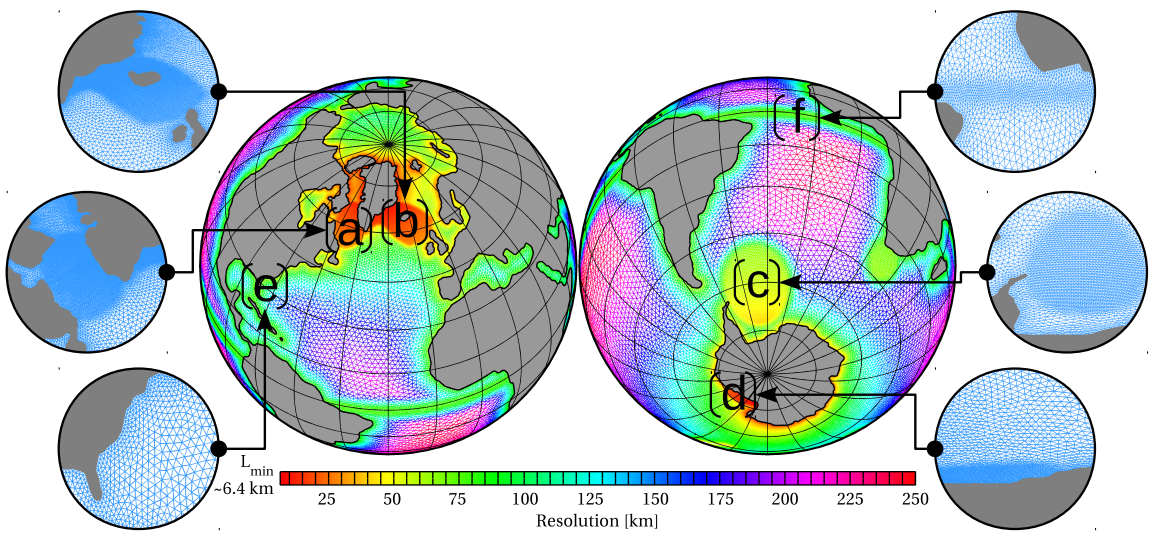

Fig. 2.1: *Global resolution of the model setup and highlighted areas with increased resolution on the northern hemisphere in Labrador Sea (a), Greenland Sea (b) and on the southern hemisphere in Weddell Sea (c) and Ross Sea (d). The resolution in Equatorial (f) and coastal areas (e) is increased as well.*

that the poles are over Greenland and Antarctic continent. The resulting convergence of the meridians increases the resolution around the coast of Greenland and Antarctica to a minimum value of $\sim$ 7 km and $\sim$ 30 km, respectively. The bulk of the model domain has a resolution of $\sim 2^\circ \times 2^\circ \cos(\Theta)$.

To adapt the setup for our special purposes to adequately simulate the deep-water formation, we further increased the resolution in important deep-water formation areas. On the northern hemisphere we increased the resolution to $7 - 20$ km in the Labrador Sea (LS) and to $10 - 20$ km near the Greenland Scotland Ridge. On the Southern Hemisphere, we increased the resolution in the central Weddell Sea to $35 - 75$ km and in the Ross Sea with minimum values that are in the order of 10 km. Because coastal and equatorial upwelling regions can also play an important role in driving the large-scale ocean circulation we tried to refine them as well. The coastal resolution is scaled with $S_{min} + (S_{max} - S_{min}) \cdot \tanh(d_i)$, where d_i is the minimum distance of each mesh point to the coast. S_{min} is the resolution at the coast and S_{max} is the resolution in

the ocean interior. With this method we reach a globally refined coastal area with a resolution of $50 - 75$ km. Additionally, we refined the mesh in a belt of 10° around the equator with a resolution of 70 km. The locally achieved minimum resolution is a trade-off of: i) the global coverage of our setup, ii) the locally increased resolution and iii) the maximum availability of mesh points due to a limitation in computational RAM.

For the time discretisation of the model uses a 20 minuts time step, which is determined by the finest resolution on the mesh. The bottom topography of the model setup is derived from the ETOPO5 gridded elevation data [*Edwards*, 1989]. We use 41 vertical levels with a vertical resolution of 10 m near the surface and a stepwise increasing maximum layer thickness of 300 m after a depth of 2700 m. We avoid to prescribe overflows or to artificially tune the bottom topography in critical areas like Denmark Strait and Iceland Scotland Ridge as in many other OGCMs [e.g., *Campin and Goose*, 1999], due to the anyway increased resolution of the model setup in these regions.

To prevent the model from a sudden blowing up due to unstable conditions that are created by exceptional high wind forcing we increased the vertical background viscosity ($1 \cdot 10^{-3}$ m^2/s) for the upper three layers by a factor of 3.

2.3 Normal forcing setup and spinup procedure

For our studies regarding the ocean variability over the last five decades we applied first a realistic sea surface forcing for the period 1958-2004. For the sea surface forcing we used the data from the Common Ocean-Ice Reference Experiment version 2 (COREv2) [*Large and Yeager*, 2008]. It includes surface air temperature, specific humidity, surface wind speed, radiation flux and precipitation. The implementation of the forcing uses the bulk formula of *Large and Yeager* [2008] and includes turbulent fluxes for heat (sensible and latent), water (evaporation), momentum (wind stress), radiative heat fluxes (shortwave and longwave) and water fluxes such as precipitation and river runoff. The sea surface salinity (SSS) is restored with a piston velocity of 50 m/300 days, using the Simple Ocean Data Assimilation (SODA v2.0.3) [*Carton and Giese*, 2008] salinity data from 1958-2004. All our simulations were run with a linear free surface.

Spinup procedure

The model is initialised with the temperature and salinity data from the World Ocean Atlas (WOA) (2001) [*Stephens et al.*, 2002]. After that the model is run with the combined COREv2 and SODA forcing for the period of 1958-2004 with four repeating cycles to reach a quasi-equilibrium state in the upper and intermediate ocean. The result of the last simulation year (2004) is than taken as the initial condition of the subsequent cycle. Due to the relatively high numerical cost of the FESOM approach its not possible to spinup the model for 1000 years like in the case of other OGCMs with our present computer resources. The spinup procedure and convergence of the model is analysed in terms of AMOC profiles and variability. The calculation of transport quantities (e.g. streamfunction) that require a differentiation or integration of data can cause some problems when we use an unstructured mesh with the FE method. *Sidorenko et al.* [2009] described in detail the common problem of interpreting the data not in a Finite-Element sense when interpolating them to regular meshes. Here we use a different approach when calculating the AMOC streamfunction Ψ and calculate Ψ via the vertical velocity w:

$$\begin{aligned} \frac{d\Psi}{dy} &= \int_{x_W}^{x_E} w(x,y,z)\,dx \\ \Psi(y,z) &= -\int_{y}^{y_S}\left(\int_{x_W}^{x_E} w(x,y',z)\,dx\right)dy' \end{aligned}$$

We find that the interpolation of the vertical velocity from the unstructured FESOM mesh to an regular mesh is much less affected by numerical errors than the meridional velocity. This results in a smoother and less noisy representation of the AMOC and the avoidance of filter algorithms.

The progress of the spinup process of the model is shown in Fig. 2.2 (a)-(d) in terms of the AMOC averaged from 1958-2004 for each cycle and the time evolution of the annual maximum AMOC index at 40°N (Fig. 2.2e). The first cycle (Fig. 2.2a) shows a pronounced upper circulation cell with a maximum value of ~ 10 Sv ($1\ \text{Sv} = 10^6\ \text{m}^3/\text{s}$) and a weakly developed bottom circulation cell with a magnitude of ~ -1 Sv. The inversion layer between the upper and the bottom circulation cell shows a light slope with a mean depth of ~ 3000 m. In the subsequent cycle (Fig. 2.2b) the magnitude of

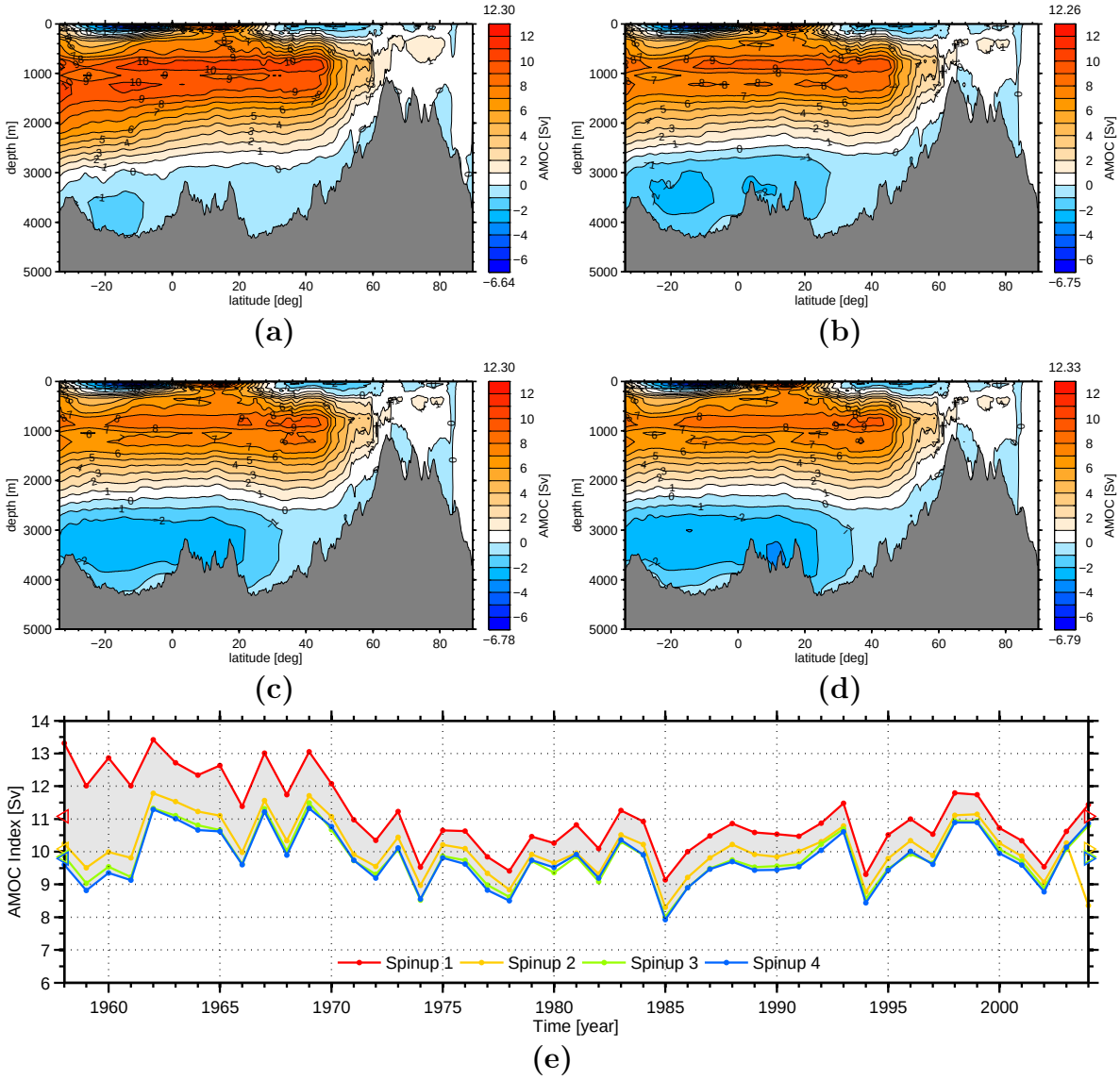

Fig. 2.2: *Mean Atlantic Meridional Overturning Circulation (AMOC) of the first (a), second (b), third (c) and fourth (d) spinup cycle. The simulation period of each spinup cycle goes from 1958-2004. Panel (e) shows the time evolution of the annual maximum AMOC index at 40°N for all four spinup runs. Triangles mark the values of the mean maximum AMOC index.*

the upper circulation cell decreases to a value of 9 Sv while the magnitude of bottom cell is slightly increasing and extending more northward. The slope of the boundary

between the upper and the bottom cell is decreasing and the mean depth of the upper cell is becoming shallower with a value of $\sim$ 2700 m. In the third spinup cycle (Fig. 2.2c), the upper circulation cell of the AMOC is still becoming slightly weaker, while the magnitude of the bottom cell further extends to values of ~ -2 Sv. The slope of the boundary between upper and bottom cell becomes almost horizontally with an even shallower depth of $\sim$ 2500 m. The upper circulation cell of the last cycle (Fig. 2.2d) shows almost no changes in shape and magnitude comparing to the previous spinup run. Also the slope and the depth of the boundary between upper and the bottom cell is staying almost constant. These large-scale quantities seem to widely converge within the four spinup cycles. Only the magnitude of the bottom cell further increase slightly to a value of ~ -3 Sv.

The time evolution of the annual maximum AMOC index at 40°N for all four spinup cycles is shown in Fig. 2.2e. The AMOC time evolution of the first spinup cycle reveals a strong negative trend in the first third of the simulation period from 1958-1975. In this period the maximum AMOC dropped by a value of $\sim$ 2.5 Sv. After this period the decrease in the AMOC index is moderate. The following spinup cycles do not show such pronounced trends in the time evolution of the AMOC index. Also the variability in the AMOC strength indicate common pattern in time for the subsequent spinup cycles. Only the mean AMOC is slightly decreasing as indicated by triangles.

The fact that the maximum AMOC index and the upper circulation cell of the AMOC reaches a quasi-equilibrium state within the first $\sim$ 100 years of simulation agrees well with the findings of *Sidorenko et al.* [2011] regarding the model spinup of his setup. Our spinup results show in addition that the extent of the AMOC bottom cell is almost converged within our four spinup cycles, whereas the magnitude of the bottom cell still shows a weak upward trend. The decadal AMOC variability is comparable to other model results from *Biastoch et al.* [2008] and *Huang et al.* [2012], but its upper cell magnitude of 9.75 Sv is at the lower range of values as shown by different models [*Griffies et al.*, 2009] as well as when compared to observations [*Ganachaud and Wunsch*, 2000; *Ganachaud*, 2003; *Bryden et al.*, 2005]. However, a principal problem for estimate AMOC is related to the fact that one has to take into account for both variability and observational uncertainty.

All results of chapter 4, 5 and 7 regarding the normal forcing are based on the last

spinup cycle of the normal forcing setup.

2.4 Random forcing setup

To be able in chapter 7 to distinguish between ocean modes that are associated to the atmospheric forcing or that are related to internal modes of the ocean, we simulated another run, where we forced the model with a random distributed COREv2/SODA forcing for the period 1958-2004. For this forcing field we distributed the years of the normal COREv2/SODA randomly over time so that the normal variability is replaced by white noise. Also for this run we initialised the model with the temperature and salinity data from the World Ocean Atlas (WOA) (2001) [*Stephens et al.*, 2002] and applied the same four spinup cycles as described in section 2.3. All results that are shown in chapter 7 regarding the random forced run are related to the last spinup cycle of the random forced COREv2/SODA simulation.

2.5 Adjustment of normal forcing setup for the validation of LSW variability

For the validation of the Labrador See Water variability (see chapter 6) we initialized the model with the last output year of the last spinup cycle of the normal forcing setup and applied the same sea surface forcing except for the SSS.
Model tests (not shown) revealed that, if the model is forced with the salinity climatology provided by COREv2 [*Large and Yeager*, 2009], the model results show a better comparability with the observational data towards the end of the simulation period than with the SODA SSS forcing. For that reason we used in chapter 6 for the validation of Labrador Sea Water variability the COREv2 salinity climatology as SSS forcing which allows us additionally to take advantage of the full temporal coverage of the COREv2 data set and to extent the simulation period until 2007.

AWI Alfred-Wegener-Institut für Polar- und Meeresforschung in der Helmholtz-Gemeinschaft

3 Principal Oscillation Patterns (POP) analysis

3.1 POP analysis

The principal oscillation patterns (POP) are a multivariante analysis method to empirically derive the space and time variations of a complex system. The POP method considers the full space-time structure of a data set, by identifying and fitting a linear dynamical system to the space-time data set that describes with a minimum degrees of freedom a maximum of its variability [*von Storch et al.*, 1995].
The evolution of a stochastical space-time system $\mathbf{x}(r,t)$ with n space degrees of freedom can be modeled by the linear vector process [*Gallagher et al.*, 1991; *Johnson et al.*, 2000]:

$$\frac{d\mathbf{x}(t)}{dt} = B\mathbf{x}(t) + \mathbf{r}(t) \tag{3.1}$$

where B is a constant $(n \times n)$ system matrix, $\mathbf{x}(t)$ is the state vector and $\mathbf{r}(t)$ is a external stochastic forcing which drives the system. B describes the internal dynamics of the stochastic system. The discretisation of (3.1) has the form:

$$\mathbf{x}(t+1) = A\,\mathbf{x}(t) + \mathbf{r}(t)\ , \quad A = \exp(B) \tag{3.2}$$

where A is a $(n \times n)$ matrix that depends on B and that is also referred as the propagator matrix. In the following the matrix A can be estimated by fitting it to the process (3.2) by [*Gallagher et al.*, 1991; *von Storch et al.*, 1995]:

$$A = \frac{\langle \mathbf{x}(t+1)\mathbf{x}(t)^T \rangle}{\langle \mathbf{x}(t)\mathbf{x}(t)^T \rangle} \quad \text{if} \quad \langle \mathbf{r}(t)\mathbf{x}(t)^T \rangle = 0 \tag{3.3}$$

The discretized homogenous real system (3.2), with $r = 0$ has a complete set of linearly independent eigenmodes (normal modes), that are characterized by the eigenvectors $\mathbf{p_k}$, $k = 1 \dots n$ and corresponding eigenvalues λ_k, $k = 1 \dots n$ of the matrix A. The eigenvectors $\mathbf{p_k}$ are referred as the Principal Oscillation Pattern of the linear discretized real system.

$$A\ \mathbf{p_k} = \mathbf{p_k}\ \lambda_k \tag{3.4}$$

Due the fact that the matrix A is not symmetric, some or all of its eigenvalues λ_k and eigenvectors $\mathbf{p}$ are complex. Because $\mathbf{x}$ and B are real all complex eigenvalues and eigenvectors occur in conjugate complex pairs λ_k^*, $\mathbf{p_k^*}$ that also satisfy the eigenequation (3.4). The eigenvectors form a linear basis, which allows to reconstruct the state vector $\mathbf{x}$ in terms of the eigenvectors $\mathbf{p_k}$:

$$\mathbf{x}(t) = \sum_{k=1}^{n} \mathbf{z_k}(t) \cdot \mathbf{p_k} \tag{3.5}$$

where $z_k(t)$ describe the POP coefficients which satisfies the standard diagonalized damped harmonic oscillator equation:

$$\mathbf{z_k}(t+1) = \lambda_k \mathbf{z_k}(t) + \mathbf{r_k} \tag{3.6}$$

If we express the complex eigenvalue $\lambda_k = \lambda_k' + i\lambda_k''$ by $|\lambda_k| \exp(i\omega_k)$ the homogenous equation has the solution [*Gallagher et al.*, 1991]:

$$\mathbf{z_k}(t) = \mathbf{z_k}(0) \exp\left(\frac{-t}{\tau_k}\right)\ \exp\left(\frac{i2\pi t}{T_k}\right). \tag{3.7}$$

with

$$\tau_k = -\frac{1}{\ln|\lambda_k|} \tag{3.8}$$

$$T_k = \frac{2\pi}{\omega_k}\ ,\quad \omega_k = \tan^{-1}\left(\frac{\lambda_k''}{\lambda_k'}\right) \tag{3.9}$$

where λ_k' and λ_k'' describes the real part and imaginary part of the complex eigenvalue λ, respectively. τ_k, ω_k and T_k describes the damping time, frequency and period of the

kth POP mode. Let $\mathbf{X}_k(t)$ be the contribution of the conjugate pair of eigenvectors to the state process $\mathbf{x}(t)$

$$\mathbf{X_k}(t) = \mathbf{z_k}(t) \cdot \mathbf{p_k} + \mathbf{z_k}(t)^* \cdot \mathbf{p_k}^* \tag{3.10}$$

with $\mathbf{p_k^i} = \mathbf{p_k}^r + i \cdot \mathbf{p_k}^i$ and $2\mathbf{z_k^i}(t) = \mathbf{z_k}^r(t) - i \cdot \mathbf{z_k}^i(t)$ equation (3.10) transforms to

$$\mathbf{X_k}(t) = \mathbf{z_k}^r(t) \cdot \mathbf{p_k}^r + \mathbf{z_k}^i(t) \cdot \mathbf{p_k}^i. \tag{3.11}$$

Insert (3.7) into (3.11) gives:

$$\mathbf{X_k}(t) = |\lambda_k| \left(\cos(\omega_k t) \cdot \mathbf{p_k}^r - \sin(\omega_k t) \cdot \mathbf{p_k}^i\right) \tag{3.12}$$

where eq. (3.12) describes a trajectory spiral in the phase space spanned by $\mathbf{p_k}^r$ and $\mathbf{p_k}^i$ with the consecutive order:

$$\cdots \rightarrow \mathbf{p_k}^r \rightarrow -\mathbf{p_k}^i \rightarrow -\mathbf{p_k}^r \rightarrow \mathbf{p_k}^i \rightarrow \mathbf{p_k}^r \rightarrow \cdots \tag{3.13}$$

where the period T_k is the time-span to fulfill one complete cycle [*von Storch et al.*, 1995].

Due to the unsymmetry of the propagator matrix A POPs can be real $\mathbf{p_k^r}$ as well as complex $\mathbf{p_k^i}$, where k describes the index of the POP mode. The real POPs describe a non-propagating damped standing oscillations, while the complex POPs that are characterized by its real $Re\{\mathbf{p_k^i}\} = \mathbf{p_k}^r$ and imaginary part $Im\{\mathbf{p_k^i}\} = \mathbf{p_k}^i$ describe damped propagating oscillations. The corresponding real and complex coefficient time series $\mathbf{z_k^r}$ and $\mathbf{z_k^i}$, respectively satisfies the standard damped harmonic oscillator equation [*von Storch et al.*, 1995; *Park and Latif*, 2010]. The time evolution of the complex system in the two dimensional POP space, spanned by the real and imaginary part, is described by the trajectory spirals (eq. (3.13)). The evolution can be interpreted as a sequence of consecutive spatial patterns at intervals of $T_k/4$, The propagating oscillations are than characterized by the period T_k and damping time τ_k. A POP mode can be regarded as stable, when there damping time exceeds their period, which means $\tau_k/T > 1$.

3.2 Expansion in empirical orthogonal functions

To reduce the noise level of the original space-time process $\mathbf{x}(r,t)$ and to limit the degrees of freedom of the POP analysis, a Empirical Orthogonal Function (EOF) analysis can be applied prior the POP analysis. The EOF method helps to identifies structures that explain the maximum amount of variance in the original space-time data set. Therefor the space-time data set is transformed into the empirical orthogonal function space which is a set of time-invariant orthogonal functions in the real space. The EOFs $\mathbf{E_i}$, $i = 1 \ldots n$ are the eigenvectors of the covariance matrix $\Sigma_0 = \langle\, \mathbf{x}(r,t), \mathbf{x}(r,t)^T \rangle$ of the space-time data set $\mathbf{x}(r,t)$

$$\Sigma_0\ \mathbf{E_i} = \beta_i\ \mathbf{E_i}. \tag{3.14}$$

Thus, the original space-time vector $\mathbf{x}(r,t)$ can be expressed as a linear combination of the n eigenvectors $\mathbf{E_i}$

$$\mathbf{x}(r,t) = \sum_{i=1}^{n} \mathbf{c_i}(t)\ \mathbf{E_i}(r) \tag{3.15}$$

where $\mathbf{c_i}(t)$ are a set of coefficients also referred as Principal Components (PC), which are derived from the projection of $\mathbf{x}(r,t)$ on the EOFs $\mathbf{E_i}$

$$\mathbf{c_i}(t) = \sum_{r=1}^{n} \mathbf{x}(r,t)\, \mathbf{E_i}(r). \tag{3.16}$$

Whereas $\mathbf{x}(r,t)$ describes the space-time variability in euclidean coordinates, describes $\mathbf{c_i}(t)$, $i = 1 \ldots n$ the same variability expressed in EOF-space coordinates [*Gallagher et al.*, 1991].

To reduce the size of the original space-time data set $\mathbf{x}(r,t)$ and to remove noisy components, we may now limit the EOF space to m ($m < n$) EOFs which should describe enough fraction of variance of the original space-time data set to preserve most of the original signal. The reduced EOF space-time data set $\hat{\mathbf{x}}(r,t)$ is given by

$$\hat{\mathbf{x}}(r,t) = \sum_{i=1}^{m} \mathbf{c_i}(t)\ \mathbf{E_i}(r). \tag{3.17}$$

The POP analysis is then performed like in the preceding section with the reduced EOF space-time data set $\hat{\mathbf{x}}(r,t)$. The resulting POP modes $\hat{\mathbf{p}}_\mathbf{k}$ are defined in EOF-space coordinates and need to be transferred back to euclidean coordinates by

$$\mathbf{p_k} = \sum_{i=1}^{m} \hat{\mathbf{p}}_{\mathbf{k,i}}\, \mathbf{E_i}. \tag{3.18}$$

For our work we follow the recommended EOF analysis routine of *von Storch and Hannoschöck* [1984], which comprise an optimization for large space-time systems.

AWI Alfred-Wegener-Institut für Polar- und Meeresforschung in der Helmholtz-Gemeinschaft

4 Validation of the Sea Ice Model

Sea ice has global effects on deep water formation and thus the AMOC. Therefore, it is crucial that the sea ice model reproduces realistic sea ice distributions in the polar regions. In this chapter we present the validation of the coupled sea ice model component for the global FESOM setup described in section 2.2 using the realistic forcing conditions of section 2.3. We validate the sea ice model results based on a comparison with observational sea ice fields from *Cavalieri et al.* [1996, updated 2007] and *Meier et al.* [2006, updated 2007] as well as observed sea ice extent indices of *Fetterer et al.* [2002, updated 2009]. All following model results of this chapter are based on the last spinup cycle of the normal COREv2/SODA forcing setup presented in section 2.3.

4.1 March and September sea ice distribution

Fig. 4.1 shows the mean Arctic sea ice concentration of the model (Fig. 4.1 (a),(b)) and observational fields (Fig. 4.1 (c),(d)), derived from *Cavalieri et al.* [1996, updated 2007] and *Meier et al.* [2006, updated 2007] in March (left column) and September (right column) averaged over the period from 1979-2004. The Arctic winter sea ice cover in March (Fig. 4.1a) reveals a large coverage over the entire central Arctic region. The March mean sea ice extent (the area where the sea ice concentration was $> 15\%$) reached a value of $14.86 \cdot 10^{12}$ m^2, which is in the order of observational mean sea ice extent values of $15.69 \cdot 10^{12}$ m^2 [*Fetterer et al.*, 2002, updated 2009]. The 15% boundary of the winter sea ice concentration extends into the Barents Sea until 75°N and along the east coast of Greenland and the Labrador peninsula until 53°N. The modelled and observational mean sea ice concentration fields in March are in good agreement. The

pronounced retreat in the summer Arctic sea ice coverage is clearly seen (Fig. 4.1b). During boreal summer, the Arctic sea ice extent is reduced by around 40% and retreats to a value of $8.91 \cdot 10^{12}$ m^2. The observed Arctic September sea ice extent features a smaller value of $6.91 \cdot 10^{12}$ m^2 *Fetterer et al.* [2002, updated 2009]. Our model results indicate a slight overestimation of the Arctic summer sea ice extent comparing to the observations. The modelled results for the summer Arctic sea ice concentration show a relatively high concentration in the region of the Baffin Bay, that is not identifiable in the observational data showed in Fig. 4.1d.

Fig. 4.2 shows the mean Southern Ocean sea ice concentration of the model (Fig. 4.2 (a),(b)) and observational field (Fig. 4.2 (c),(d)), derived from *Cavalieri et al.* [1996, updated 2007] and *Meier et al.* [2006, updated 2007] in March (left column) and September (right column) averaged over the period from 1979-2004. The Southern Ocean sea ice concentration in March (Fig. 4.2a) reveals a region of maximum sea ice concentration of 80% in the Weddell Sea that extends northward at the east coast of the Antarctic peninsula and gradually decreases, as well as a stripe of sea ice with concentrations up to $\sim$ 50% that extends along the western Antarctic coast from the Amundsen Sea to the Ross Sea and Victoria Land coast. The 15% boundary of the Southern Ocean austral summer sea ice concentration barley extends above 70°S. Only in the Weddell Sea it extends until $\sim$ 66°S. The minimum sea ice extent in March reached a value of $2.85 \cdot 10^{12}$ m^2, which underestimates the observed March sea ice extent of $4.36 \cdot 10^{12}$ m^2 [*Fetterer et al.*, 2002, updated 2009] by a factor of 1.4. The Southern Ocean mean sea ice concentration in March, reproduced with our model setup, agrees reasonably with the observational results shown in Fig. 4.2c. The March sea ice extent in the Amundsen Sea and Ross Sea in our model is underestimated compared to the observational data derived from *Cavalieri et al.* [1996, updated 2007] and *Meier et al.* [2006, updated 2007]. Furthermore, the observational data does not show an increased sea ice concentration around the Victoria Land coast in contrast to our model results. In austral winter (September), entire Southern Ocean is enclosed by a compact sea ice cover. The sea ice extends until 65°S and encloses an area of $20.16 \cdot 10^{12}$ m^2, which is in the vicinity of the observed value of $18.7 \cdot 10^{12}$ m^2. Comparing to the observational results shown in Fig. 4.2d, the area with a sea ice concentration $> 90\%$ in our model extends more northward, but the 15% boundary of the sea ice concentration is in a

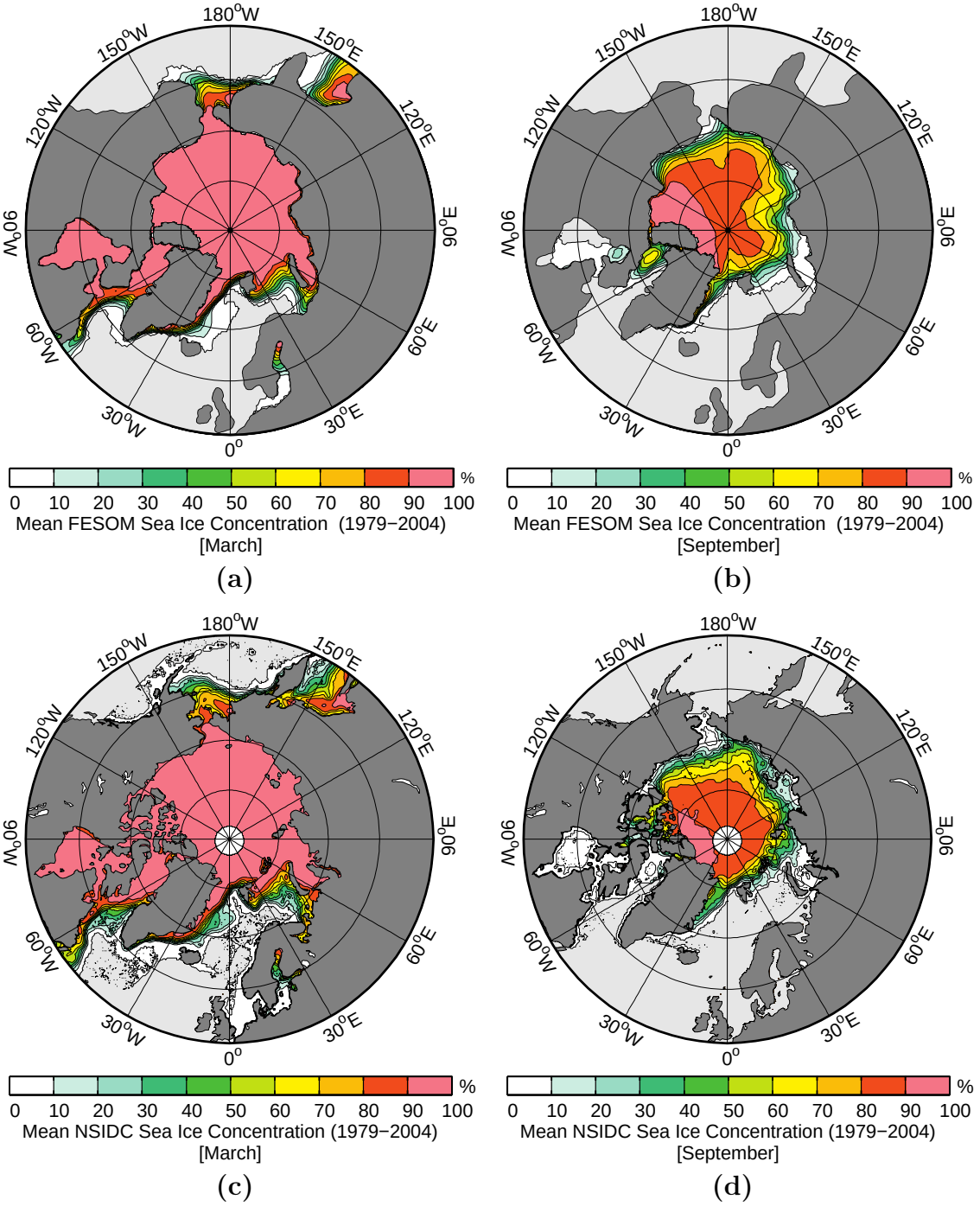

Fig. 4.1: *Simulated (a), (b) and observed (c), (d) mean Arctic sea ice concentration in March (left column) and September (right column). Ice-free areas are marked light grey. The observed fields have been derived from Cavalieri et al. [1996, updated 2007] and Meier et al. [2006, updated 2007].*

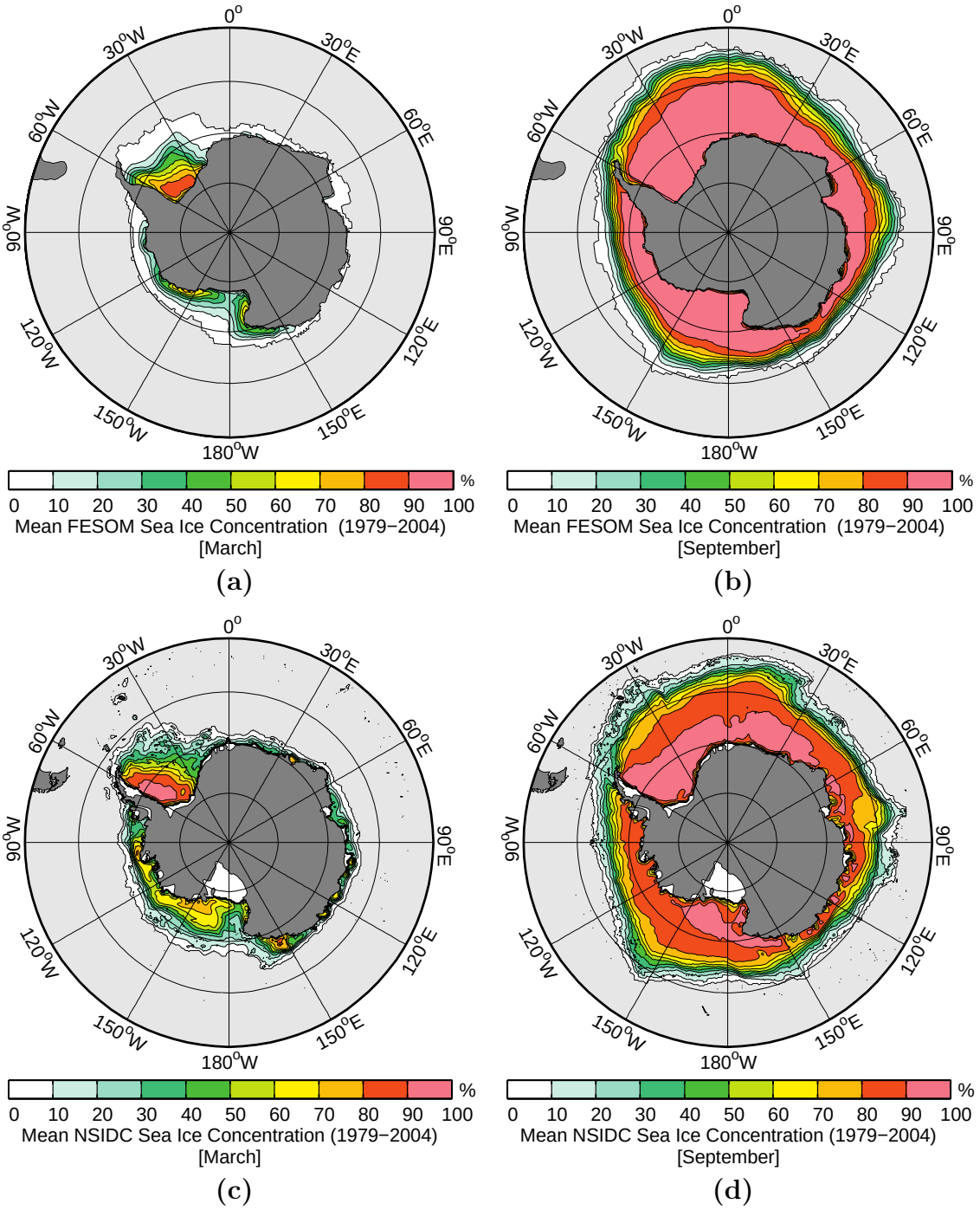

Fig. 4.2: *Simulated (a), (b) and observed (c), (d) mean Antarctic sea ice concentration in March (left column) and September (right column). Ice-free areas are marked by light grey. The observed fields have been derived from Cavalieri et al. [1996, updated 2007] and Meier et al. [2006, updated 2007].*

good agreement with the observations.

4.2 Northern and Southern Hemispheric sea ice variability

Fig. 4.3 (a), (b) shows the time evolution of the mean annual Arctic and Southern Ocean sea ice extent of the model (black) and observational (red) data, derived from *Fetterer et al.* [2002, updated 2009]. The time evolution of Arctic (Fig. 4.3a) and Southern Ocean (Fig. 4.3b) sea ice extent has a mean value of $11.75 \cdot 10^{12}$ m^2 and $11.7 \cdot 10^{12}$ m^2, respectively. Both time series show a pronounced decadal variability that are in good agreement with the variability of the observational data. The Arctic sea ice extent reveals a slight decreasing trend over the entire simulation period of $-8\,500$ km^2/yr. This trend is even stronger for the second half of the simulation period from 1979-2004, with a value of $-18\,500$ km^2/yr. The observed Arctic sea ice extent (red) in the interval 1979-2004, shows by a factor of ~ 2 decreased trend of $-40\,000$ km^2/yr. The trends in the time evolution of the Southern Ocean sea ice extent (Fig. 4.3b) depends on the period that is considered. For the interval from 1979-2004 the model reveals a rise in the Southern Ocean sea ice extent of 11 800 km^2/yr. This trend agrees quite well with the trend in the observed sea ice extent with a value of 12 700 km^2/yr. But the observed Southern Ocean sea ice extend for the interval 1979-2004 is in general compared to the modeled values $\sim 0.6 \cdot 10^{12}$ m^2 higher.
We furthermore calculated the 3 year-running-mean filtered sea ice transport over time for a Denmark Strait (Fig. 4.3c) and Fram Strait (Fig. 4.3d) cross section. Both time series feature an outstanding high sea ice transport around 1967-1968 followed by smaller events around 1977, 1982, 1988 and 1994. The variability of the model Fram Strait sea ice transport is in good agreement with the observed time series of *Schmith and Hansen* [2003] (Fig. 4.3d). Although the model features compared to the observed time series a constant high sea ice transport between 1970 and 1980 and a general offset of ~ 0.03 Sv. The mean sea ice transport through the Fram Strait for the interval of 1990-1995, with 0.15 Sv, overestimates the upper boundary value of *Kwok and Rothrock* [1999] with 0.106 Sv by a factor of 1.4.

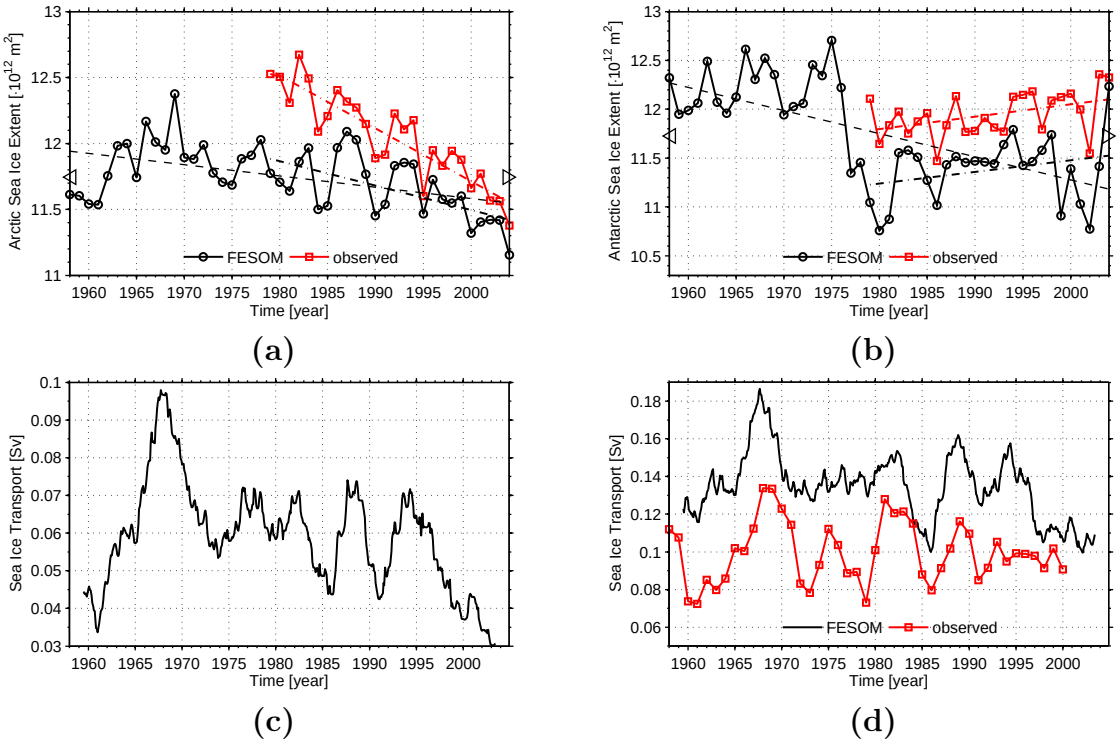

Fig. 4.3: *(a)-(b): Time evolution of the simulated (black) and observed (red) annual sea ice extent in the Arctic (a) and Southern Ocean (b). Dashed lines indicate the trend in sea ice extent for the interval 1958-2004 and 1979-2004. The observed sea-ice extent indices has been derived from Fetterer et al. [2002, updated 2009].*
(c)-(d): Time evolution of the 3 year-running-mean filtered sea-ice volume transport through Denmark Strait (c) and Fram Strait (d) (black). The observed (red) annual Fram Strait Sea-Ice volume transport in (d) is derived from Schmith and Hansen [2003].

4.3 Sea ice model validation

In this chapter we presented the validation of the sea ice model for Northern and Southern Hemisphere a global FESOM setup with locally refined resolution in a global context.

The validation of the sea ice model revealed that the sea ice concentration in the Arctic and Southern Ocean resembles quite well the observational fields from *Cavalieri et al.* [1996, updated 2007]. The sea ice shows a more realistic sea ice concentration distribu-

tion than the FESOM setup shown by *Timmermann et al.* [2009] under NCEP forcing. The increased summer sea ice concentration in the Baffin Bay was neither found in the observational fields or in the modelled FESOM results of *Timmermann et al.* [2009] which might be related to the forcing. In this respect, our model results resembles quite well the modelled FESOM sea ice concentration distribution of *Sidorenko et al.* [2011], which used the Coordinated Ocean Ice Reference Experiment version 1 (COREv1) data as forcing.

The comparison of modelled and observed Arctic and Southern Ocean sea ice extent time series indicates that the sea-ice model is able to reproduce most of the variability that is shown in observational data [*Fetterer et al.*, 2002, updated 2009]. The model underestimates in general the observed sea-ice extent by $0.6 \cdot 10^{12}$ m^2 and the decreasing trend in Arctic sea ice extent. The comparison of modelled and observed sea ice transport through the Fram Strait revealed that the model is also capable to reproduce the variability, although the model tends to overestimate here the observational data from *Schmith and Hansen* [2003].

AWI Alfred-Wegener-Institut für Polar- und Meeresforschung in der Helmholtz-Gemeinschaft

5 Validation of the Ocean Model

To challenge the task of future ocean modelling, we will need the ability to faithfully resolve coastlines and regional areas of interest without loosing the global context of the ocean general circulation. It has been shown, since the early work of *Fix* [1975] that the Finite-Element (FE) method in conjunction with an unstructured mesh can be a suitable approach to fulfil this requirement. There have been only a few FE ocean general circulation models developed so far that employ the capability of unstructured meshes [*Danilov et al.*, 2004; *Ford et al.*, 2004; *White et al.*, 2008]. In this study we use the Finite-Element Sea-Ice Ocean Model (FESOM) [*Danilov et al.*, 2004, 2005; *Wang et al.*, 2008a; *Timmermann et al.*, 2009] as described in chapter 2. FESOM uses unstructured triangular meshes, that allow for local refinement in an otherwise global setup.

In this chapter we present the validation of the ocean model component using the global FESOM setup described in section 2.2 under realistic forcing conditions (see section 2.3). For the purpose of simulating an adequate deep-water formation we took advantage in this FESOM setup, of the unstructured mesh functionality and resolved locally the deep-water formation areas in the Labrador Sea, Greenland Sea, Weddell Sea and Ross Sea with higher resolution (see section 2.2).

For the validation of the ocean model results we focus mainly on the region of the North Atlantic ocean. Due to the increased resolution in that area, our model setup is able to compete against other regional models [*Böning et al.*, 1996; *Chanut et al.*, 2008], with the difference that we are able to preserve the global context of the model.

To validate the results of the ocean model, we first compared the model data with data from the Ocean Weather Ships (OWS) Bravo (OWS-B) and Charly (OWS-C) [*Lazier*, 1980; *Levitus et al.*, 1994]. These OWS data provide unique long time series in the

vertical structure of the North Atlantic ocean and can be used for estimating ocean hydrography and circulation changes [*Haak et al.*, 2003; *Lohmann et al.*, 2008]. The specific location of OWS-B and OWS-C (see Fig. 5.3) gives us the opportunity to validate and compare the model for an area with the highest resolution and an area with coarser resolution to long term observations.
In this chapter we present the modelled variability of the temperature and salinity of the general Nordic Sea Overflows across the Denmark Strait and the Iceland-Scotland Ridge for different depth layers as well as of the dense water masses of the Denmark Strait Overflow Water (DSOW) and Iceland-Scotland Overflow Water (ISOW). The Denmark Strait and the Iceland-Scotland Ridge are the bottleneck for water masses and temperature and salinity anomalies of Arctic origin that enters the Atlantic basin via the Nordic Seas. From there the dense water masses of DSOW and ISOW, which are the main contributors to the North Atlantic Deep Water, spill into the abyssal plain and combine in their later pathway to the water masses of the Deep Western Boundary Current [*Sarafanov et al.*, 2009]. We test the ability of the model to reproduce an interannual variability in the overflows as its described by *Macrander et al.* [2005] from observations of the overflow at the sill of the Denmark Strait as well as from observations of *Dickson et al.* [2002].
In the subsequent section we check the ability of the model to reproduce several fresh water anomalies, in the Labrador Sea, the so called Great Salinity Anomalies (GSA) [*Dickson et al.*, 1988]. These fresh water anomalies, that are remotely driven by Arctic sea ice export, occupied several times the surface waters of the North Atlantic deep water mass formation regions [*Dickson et al.*, 1988; *Belkin et al.*, 1998; *Belkin*, 2004]. There they had a major influence on the vertical stratification and the strength of deep convection in the North Atlantic Ocean [*Haak et al.*, 2003].
All following results of this chapter are based on the last spinup cycle of the normal COREv2/SODA forcing setup presented in section 2.3.

5.1 Comparison of the Model results with OWS data

To further validate our model setup and results, we compared the model data with data from Ocean Weather Ships (OWS) [*Lazier*, 1980; *Levitus et al.*, 1994]. OWS-data

provide temperature and salinity profiles between 1950s and 1990s at different positions in the North Atlantic. We compare temperature and salinity time series for different depth layers: 0 m – 100 m, 125 m – 520 m, 620 m – 1640 m and 1880 m – 6600 m at the position of OWS-Bravo (OWS-B, 50.98°W, 56.49°N) and Charly (OWS-C, 35.5°W, 52.75°N) (Fig. 5.8). We choose these two positions because they allow us to compare the model results of an area with the highest resolution (OWS-B) and an area with coarse resolution (OWS-C) to long term observational data. Although the temperature and salinity of the most upper surface layer (0 m) is mostly prescribed by the surface forcing, it should be mentioned that we averaged her for the surface depth layers over the upper 100 m of the ocean to visualize the model performance beyond the prescribed ocean surface. The temperature evolution of the OWS-B (orange) and model (green) data shown in Fig. 5.1a reveal a good agreement for the seasonal cycle in the surface layers for the interval of 1958-1974. Also the intermediate layers of 125 m – 520 m and 620 m – 1640 m show a good agreement between the model and the OWS-B data. Both layers show a minimum temperature of ∼ 3.4 °C around 1962, followed by a gradual increase until 1971 with a maximum temperature of ∼ 3.9 °C and a subsequent decrease. The OWS-B data of temperature and salinity of the very deep layers of 1880 m – 6600 m show a wide spread of ∼ 1 °C (Fig. 5.1). This spread is not captured by the model, which only captures the underlying trend. Fig. 5.1b shows the salinity evolution of the OWS-B (red) and model (blue) data, where the surface layers show a minimum (∼ 34.3 psu) and the intermediate layers (620 m – 1640 m) shows a maximum (∼ 34.9 psu) in the early 1970s. This salinity minimum is well know as a fingerprint of the GSA event that occupied the Labrador Sea around 1970 (see also section 5.3) [*Dickson et al.*, 1988; *Haak et al.*, 2003]. The model and OWS-B time series of the salinity compares quite well in the intermediate layers (125 m – 520 m, 620 m – 1640 m). The deep ocean layers reveal an offset of ∼ 0.04 psu between the OWS-B and model data, but the underlying trend is maintained.

Fig. 5.2 shows the modelled (blue) and measured (red) temperature and salinity time evolutions at the position of the OWS-C for the four different depth layers and the interval between 1976 and 1986. The measured (orange) and simulated (green) temperature time series in Fig. 5.2a features again a good agreement in the seasonal cycle of the surface layer, while the simulated intermediate (125 m – 520 m) and deep

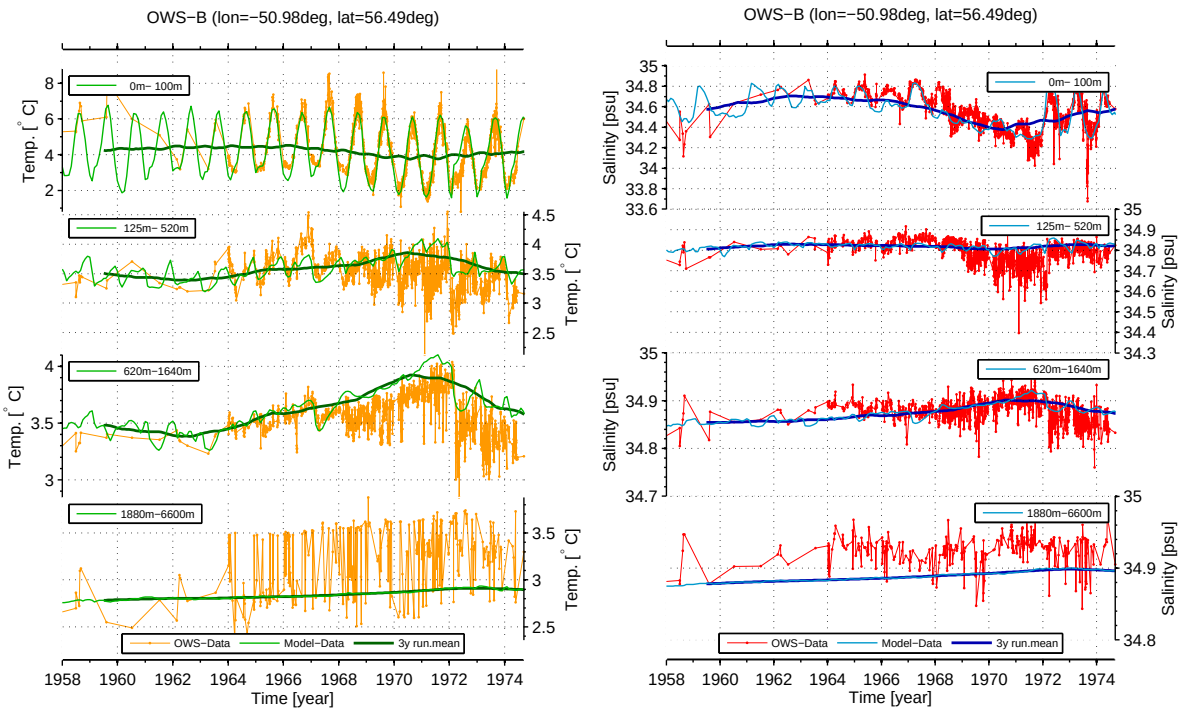

Fig. 5.1: *Time evolution of model and Ocean Weather Ship Bravo (OWS-B) temperature (a) and salinity (b) for the period 1958-1974. The modelled monthly and 3 year-running-mean filtered temperature are indicated by light green and dark green lines, respectively. Whereas the modelled monthly and 3 year-running-mean filtered salinity are indicated by light blue and dark blue lines, respectively. The OWS temperature and salinity data are indicated by orange and red dots, respectively.*

(1880 m − 6600 m) layers show a negative and positive offset, respectively. The overall temperature time evolution of the simulated and measured intermediate layers of 620 m − 1640 m agrees well. The salinity time evolutions of the modelled (blue) and measured (red) OWS-C data shown in Fig. 5.2b reveal a general offset between the modelled and measured data through all layers, which decreases with increasing depth. The surface and intermediate layers (125 m − 520 m) show an offset of ~ 0.3 psu and ~ 0.1 psu, respectively, while the model is able to reproduce the interannual variability.

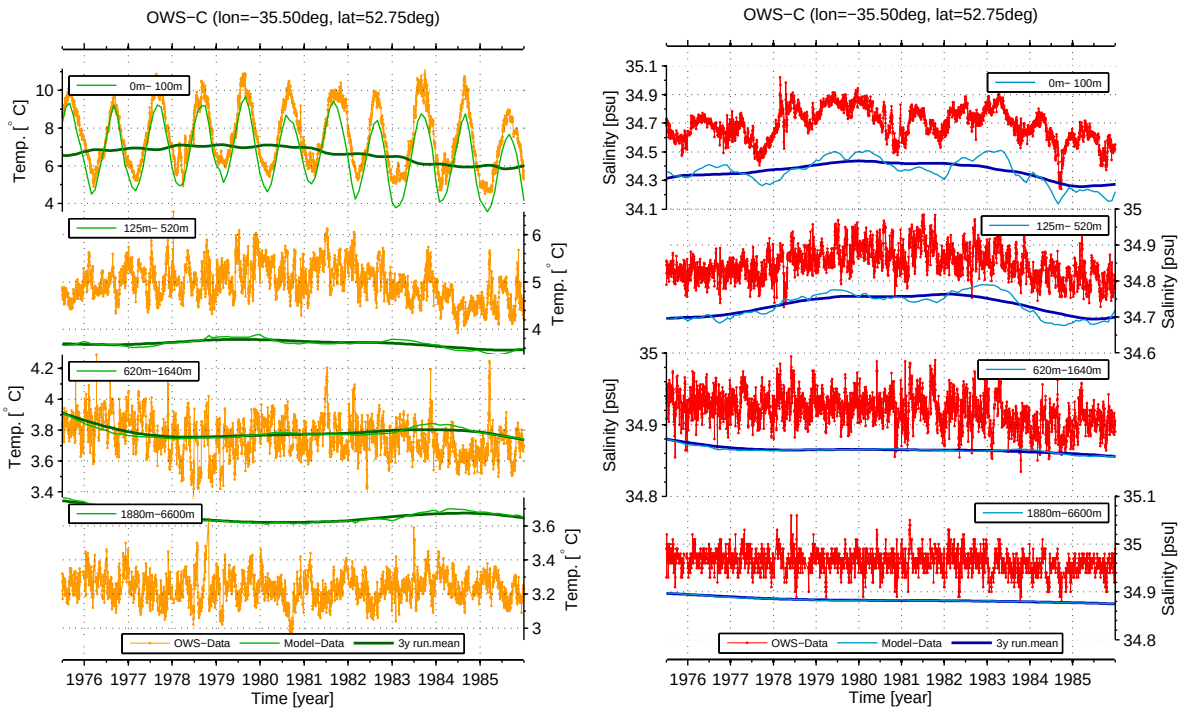

Fig. 5.2: *Time evolution of model and Ocean Weather Ship Charly (OWS-C) temperature (a) and salinity (b) for the period 1958-1974. The modelled monthly and 3 year-running-mean filtered temperature are indicated by light green and dark green lines, respectively. Whereas the modelled monthly and 3 year-running-mean filtered salinity are indicated by light blue and dark blue lines, respectively. The OWS temperature and salinity data are indicated by orange and red dots, respectively.*

5.2 Nordic Seas Overflow, DSOW and ISOW

The Nordic Sea overflow water is one of the main sources of the deep water in the North Atlantic. To observe the overflow quantities over time, we calculated for cross sections through the Denmark Strait (Fig. 5.3a) and the Iceland-Scotland Ridge (Fig. 5.3b) the 3 year-running-mean filtered mean temperature (Fig. 5.4a, 5.5a) and mean salinity (Fig. 5.4b, 5.5b), for different depth layers of 0 m − 100 m, 125 m − 350 m and 430 m − 880 m, respectively.

The filtered temperature and salinity in the surface layer (0 m − 100 m) of the Denmark

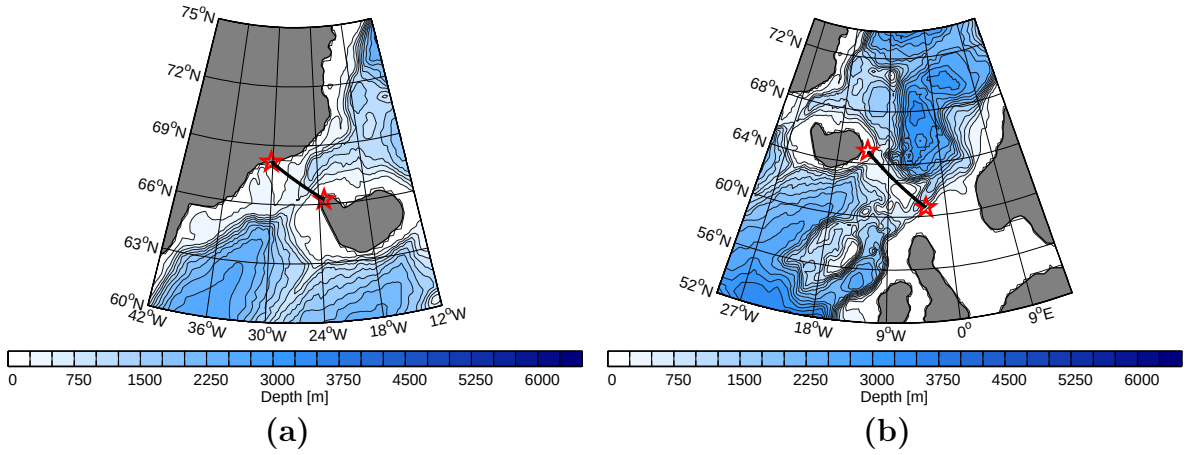

Fig. 5.3: *Position of the Denmark Strait (a) and Iceland-Scotland Ridge (b) cross-section.*

Strait cross section reveals a distinct decadal variability. The filtered time evolution shows a pronounced minimum in the temperature and salinity around 1967 (Fig. 5.4). The analysis of horizontal salinity distribution (not shown) revealed that this minimum corresponds to a negative salinity anomaly that passes the Denmark Strait and travels within the subpolar gyre. Similar, but weaker negative salinity anomalies passed the Denmark Strait around 1976, 1987 and 1995 (Fig. 5.4b). The negative salinity anomaly events corresponds also with a negative temperature anomaly on the surface (Fig. 5.4a). These four anomaly events coincide with a high sea ice transport from Arctic as shown in Fig. 4.3c and 4.3c.

The temperature evolution of the filtered time series in the intermediate layers (125 m − 350 m) shows a strong decadal variability with increasing amplitude until the late 1980s. The minima events in the temperature of the intermediate layers corresponds to the ones on the surface (Fig. 5.4a). The salinity evolution in the intermediate layers reveals a slight freshening trend almost over the entire simulation period from 1958 until 1995. The negative surface salinity anomalies of 1967, 1987 and 1995 are also identifiable in the intermediate layers except the surface salinity anomaly of 1975 (Fig. 5.4b). In 1995 the filtered time evolution of the intermediate layers of temperature and salinity reached its lowest level with a value of -0.45 °C and 33.84 psu, respectively. After that, the temperature and salinity in the intermediate layers increases again until the

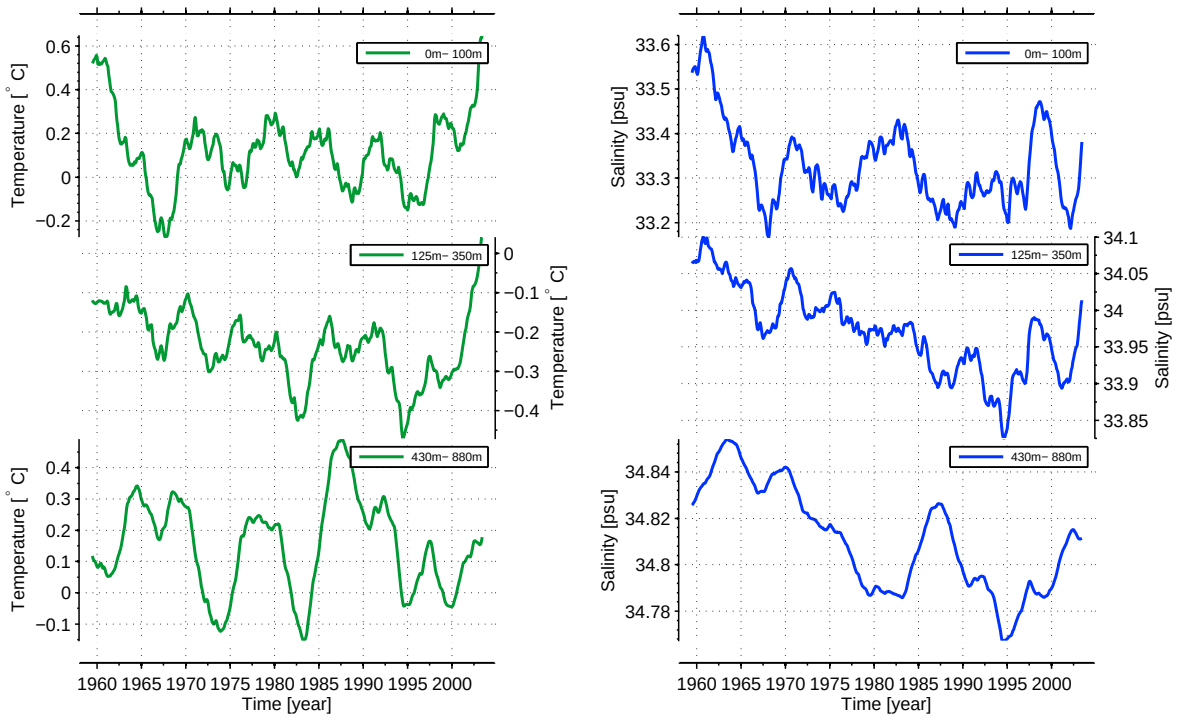

Fig. 5.4: *Time evolution of the 3 year-running-mean filtered Temperature (a) and Salinity (b) (light lines) averaged on the cross section through the Denmark Strait for three different depth layers:* $0\ m - 100\ m$ *(upper),* $125\ m - 350\ m$ *(middle) and* $430\ m - 880\ m$ *(lower).*

end of the simulation period.

The freshening trend in the salinity of the intermediate layers is continued in the deep layers ($430 - 880$ m) (Fig. 5.4b). While the salinity evolution in the deep layers shows again a slight minima around 1967 and 1995 that originate from the surface anomaly, it features also a salinity minima around 1982. This salinity minima is neither identifiable in the surface or intermediate layers. The time evolution of the deep-layer temperature shows a pronounced decadal variability with an amplitude of 0.5 °C and an underlying slight cooling trend over the entire simulation period. All negative temperature anoma-

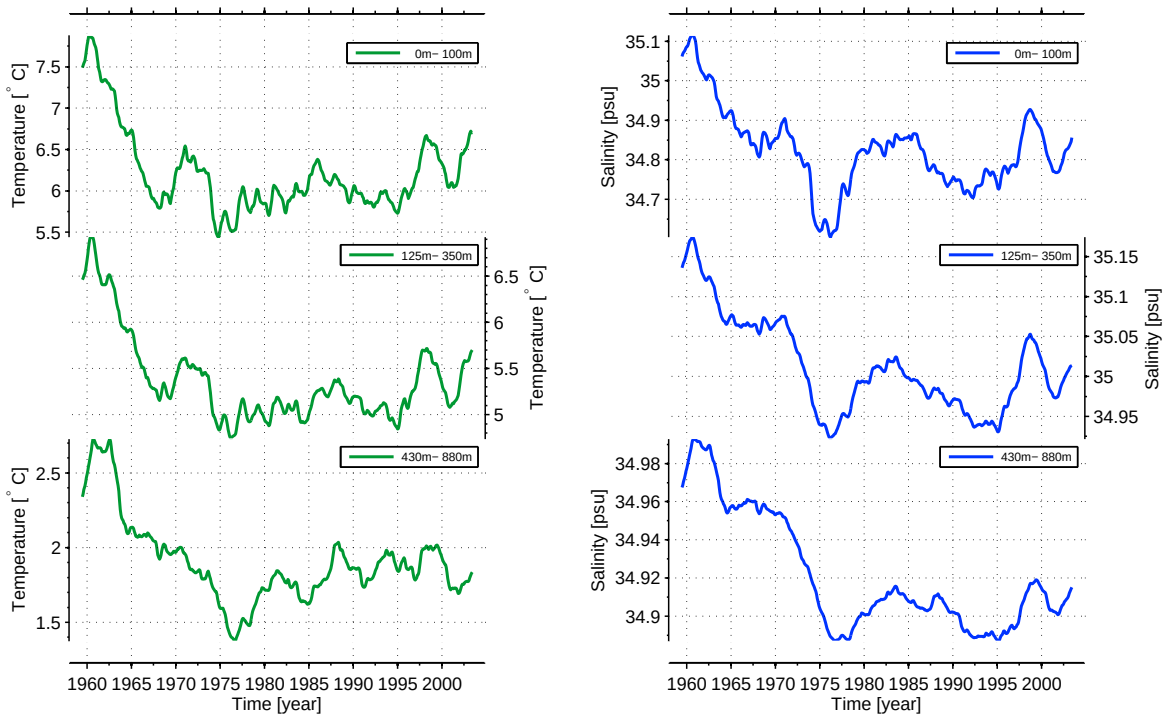

Fig. 5.5: *Time evolution of the 3 year-running-mean filtered Temperature (a) and Salinity (b) (light lines) averaged on the cross section through the Iceland-Scotland Ridge for three different depth layers:* $0\ m - 100\ m$ *(upper),* $125\ m - 350\ m$ *(middle) and* $430\ m - 880\ m$ *(lower).*

lies from the surface are also detected in the deep layers.

Fig. 5.5 shows the time evolution of the 3 year-running-mean filtered temperature and salinity, averaged on a cross section through the Iceland-Scotland Ridge for the layers: 0 m – 100 m, 125 m – 350 m and 430 m – 880 m, respectively. The temperature in all layers features a pronounced cooling trend of almost 2.3 °C until 1976 with a minimum value in the surface and deep layers of 5.5 °C and 1.7 °C. After that, the temperature shows a slight warming trend of around 0.7 °C until the end of the simulation period. The temperature evolution in all three layers runs synchronously. From 1958 until 1976,

the salinity time series in the Iceland-Scotland Ridge reveals a strong freshening trend of ~ 0.5 psu in the surface layers and ~ 0.22 psu and 0.15 psu in the intermediate and deep layers, respectively. The minimum value is reached around 1976 with a value of ~ 34.6 psu on the surface. After 1976, the salinity increases again until the middle of the 1980s, followed by a renewed freshening that reaches its lowest level around 1995. Analysis of horizontal salinity distribution in the intermediate layers revealed that both salinity minima from 1976 and 1995 could originate from a negative salinity anomaly that passed the Denmark Strait around 1967 and 1987, travelled within the subpolar gyre and recirculated over the Iceland-Scotland Ridge back to the Greenland Sea (not shown).

DSOW and ISOW

The densest water masses that spills via the Denmark Strait and the Iceland-Scotland Ridge into the abyssal basin of the North Atlantic are the Denmark Strait Overflow Water (DSOW) and the Iceland Scotland Overflow Water (ISOW). The presence of both water masses can be found throughout large parts of the Atlantic basin below a depth of 1000 m *Curry et al.* [2003]. DSOW and ISOW are part of the bulk water masses that form the southward-flowing lower limb of the AMOC. In this study we define the overflow water masses of DSOW and ISOW by potential densities $\sigma_\theta > 28.80\,\mathrm{kg\,m^{-3}}$ [*Dickson and Brown*, 1994; *Girton and Sanford*, 2001] and southward directed flow that pass the Denmark Strait and Iceland-Scotland Ridge cross-section of Fig. 5.3.
The vertical cross-section of the normal directed volume transport through the Denmark Strait and the Iceland-Scotland Ridge cross-section averaged for the time interval 1958-2004 is presented in Fig. 5.6a and 5.6b, respectively. The $\sigma_\theta = 28.80\,\mathrm{kg\,m^{-3}}$ isopycnal is highlighted by a thick contour line and southward directed flow is indicate by white to reddish colors. The vertical mean cross-section of the normal directed Denmark Strait volume transport (Fig. 5.6a) indicates a major southward directed maximum transport of 0.04 Sv in the density branch of the DSOW in a narrow band at the southern flank of the Denmark Strait. Whereas the normal directed volume transport of the Iceland-Scotland Ridge cross-section (Fig. 5.6a) reveals a pronounced southward directed maximum transport of 0.025 Sv in the density branch of the ISOW in the

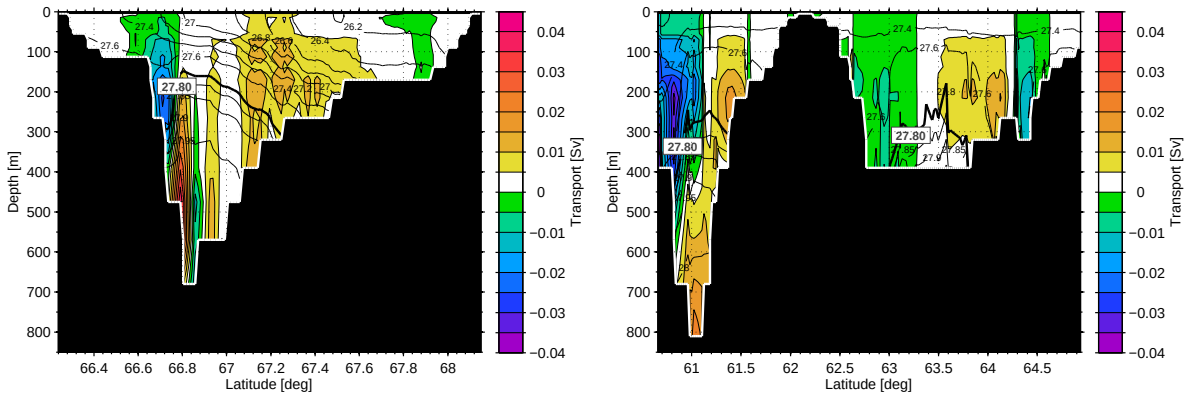

Fig. 5.6: *Vertical sections of normal directed volume transport (color code) through Denmark Strait (a) and Iceland-Scotland Ridge (b) cross-sections (see Fig. 5.3). White to reddish colors mean southward directed transport, while green to purple colors mean northward directed transport. Superimposed are the contour lines of the potential density, where the* $\sigma_\theta = 27.80\ kg\,m^{-3}$ *isopycnal is highlighted by a thick contour line.*

Faroe-Shetland Channel.

The time evolution of the 3 year-running-mean filtered modelled DSOW and ISOW, volume transport, temperature and salinity through the Denmark Strait and Iceland-Scotland Ridge cross-section is displayed in Fig. 5.7a and Fig. 5.7b, respectively. The time evolution of the DSOW volume transport (black line) reveals a mean value of $\sim$ 1.4 Sv and a significant decreasing trend for the interval 1958-1995 followed by an increasing trend until the end of the simulation period. Beside the underlying trends the DSOW volume transport features maxima around 1960, 1972, 1983, 1990 and 1997. The filtered DSOW temperature (green line) and salinity (blue line) time evolution reveals a mean value of 0.24 °C and 34.76 psu, respectively. Whereas the time-series of the DSOW salinity reveals a general freshening trend for the period 1958-1995. Both time-series feature several maxima, that match the aforementioned time evolution of the temperature and salinity of the 125 m $-$ 350 m and 430 m $-$ 880 m depth layers in Fig. 5.4.

The 3 year-running-mean filtered time-series of ISOW volume transport shows a mean value of $\sim$ 1.4 Sv, where no distinct trend is visible. There are two outstanding maxima

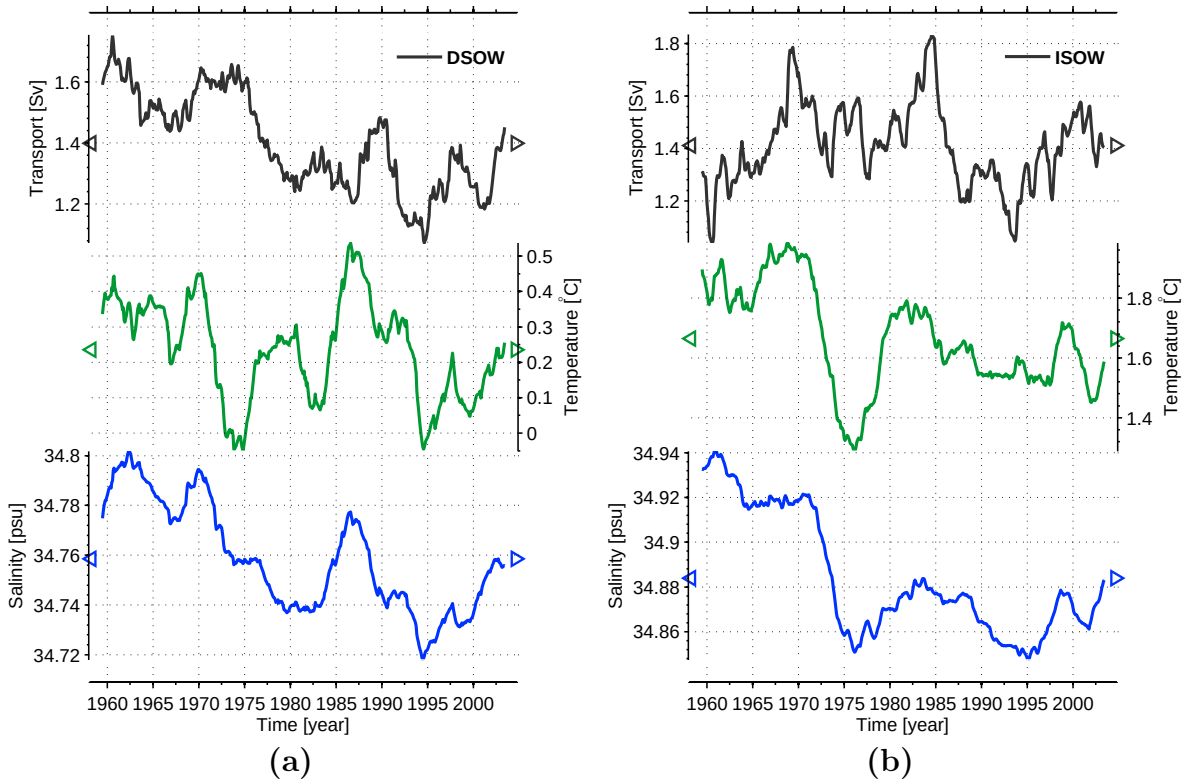

Fig. 5.7: *Time evolution of the 3 year-running-mean filtered normal volume transport (black), temperature (green) and salinity (blue) of the Denmark Strait Overflow Water (DSOW) (a) and Iceland Scotland Overflow Water (ISOW) (b). Triangles denote the time averaged values of the corresponding quantity. The overflow waters are defined by potential density* $\sigma_\theta > 27.8\ kg\,m^{-3}$ *and southward directed transport.*

in the ISOW volume transport at the end of the 1960s and in the middle of the 1980s. The time-series of the 3 year-running-mean filtered ISOW temperature and salinity show a trend to colder and fresher overflow waters over the entire simulation period. Both time-series are characterize by a strong drop in temperature and salinity in the early 1970s that reach its minimum values $\sim$ 1976 followed by a temperature and salinity increase until the early 1980s. This decrease in temperature and salinity is accompanied by a reduction in the ISOW volume transport.

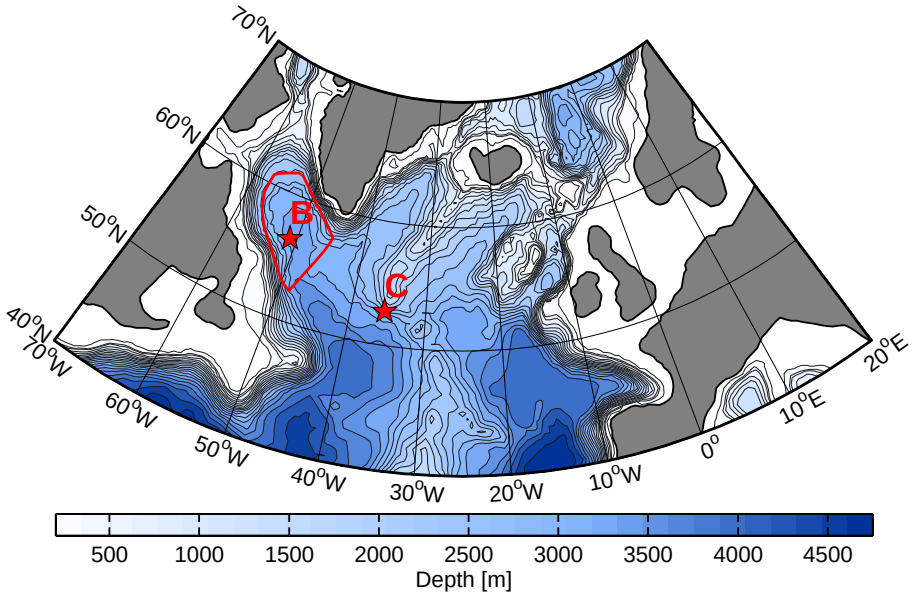

Fig. 5.8: *Position of the index selection area (red contour) in the Labrador Sea that was used to compute the temperature and salinity indices of Fig. 5.9. The index was computed as the mean of all node points that are located within the red contour line. The Position of the Ocean Weather Ships (OWS) Bravo (B) and Charly (C) are marked by red stars.*

5.3 Great Salinity Anomaly events

To have a closer look at the evolution of the deep ocean temperature and salinity we calculate for an area in the Labrador Sea (Fig. 5.8, red contour) a detrended and 3 year-running-mean filtered, temperature (Fig. 5.9a) and salinity (Fig. 5.9b) index over depth and time. The filtered temperature and salinity index reveals several positive and negative anomalies at the surface and deep ocean layers, that reach into depths of $2000 - 2500$ m. In the early 1960s, the surface layers of both indices to a depth of $\sim$ 100 m are occupied by a positive temperature and salinity anomaly of ~ 0.3 °C and ~ 0.12 psu, respectively. While the lower layers to a depth of $\sim$ 2500 m show a maximum cooling and freshening anomaly of ~ -0.3 °C and ~ -0.02 psu. In the late 1960s to the early 1970s the situation is reversed. Now the surface layers show a cooling and strong freshening event of around ~ -0.2 °C and ~ -0.1 psu, while the lower layers to a depth of $\sim$ 2000 m show a maximum warming and increase in

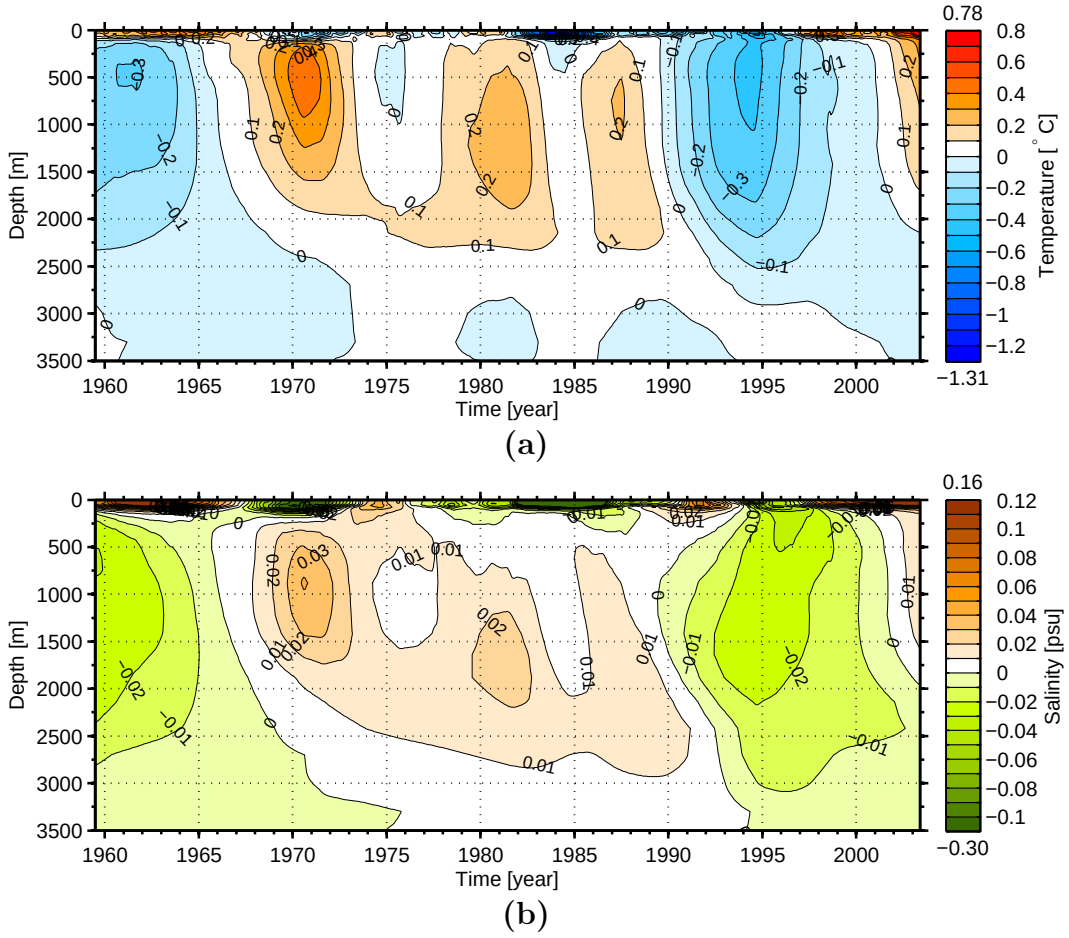

Fig. 5.9: *Temperature (a) and salinity (a) index over depth and time for the index selection area described in Fig. 5.8. The data are detrended and smoothed with a 3 year-running-mean filter.*

the salinity of ∼ 0.4 °C and 0.04 psu. This event shows the typical fingerprint of the Great Salinity Anomaly (GSA) event of 1970, that is described by *Dickson et al.* [1988]. At the beginning and at the end of the 1980s there are two similar but weaker warming and increased salinity events of the deeper ocean layers, with a maximum warming and salinification of ∼ 0.2 °C and ∼ 0.02 psu. These two GSA events are also present in observational data and are further described by *Belkin et al.* [1998] and *Belkin* [2004]. These two events are separated by a strong surface cooling and freshening of ∼ −1.3 °C and ∼ 0.1 psu in the upper 100 m of the ocean around 1984. The surface

freshening event extends thereby over the entire 1980s. In the middle of the 1990s, the temperature and salinity index reveals again a pronounced cooling and freshening anomaly of ~ -0.4 °C and ~ -0.02 psu, respectively. This negative temperature and salinity anomaly reaches from the surface into depths of 2500 m. Towards the end of the simulation period, the model indicate a new warming and positive salinity anomaly that reaches from the surface to intermediate depths.

5.4 Variability in the Atlantic Meridional Overturning Circulation

To visualize the large scale variability of the model, we will use the maximum annual AMOC index at 40°N shown in Fig. 5.10a, which feature a strong decadal variability that varies between 7.9 - 11.4 Sv with a mean value of 9.75 Sv. The maximum and minimum phase of the AMOC index are indicated by dark and light grey shadings, respectively. There are pronounced maxima in the intensity of the AMOC around 1963, 1967, 1969, 1983 and 1993 while the intensity minima are around 1959, 1974, 1978, 1985, 1994 and 2002.

To further extract the important patterns that coincide with a maximum and minimum AMOC index, we applied a Composite Map Analysis [*von Storch and Zwiers*, 2003] between the AMOC index and different meridional and horizontal quantities. For the calculation of the high (low) composites we used all time slices that are above (below) 75% of the standard deviation of the AMOC index. The time slices for the high (low) composites are marked in Fig. 5.10 by red (blue) circles.

Fig. 5.10 (b) and (c) shows the high and low composite maps of the annual mean AMOC profile, respectively. The upper circulation cell of the high AMOC composite (Fig. 5.10b) is ~ 2 Sv stronger comparing to the low AMOC composite (Fig. 5.10c) and reaches at 40° N around 300 m deeper. The magnitude of the counter clockwise wind-driven surface circulation cell at ~ 55°N is increased by ~ 1 Sv comparing to the low AMOC composite. The magnitude of the bottom circulation cell is the same for the high and low AMOC composites, but the -1 Sv streamline of the bottom circulation cell in the low AMOC composite (Fig. 5.10c) extents more northward until 52°N.

Fig. 5.11 (a) and (b) shows the the high and low composite maps for the winter mean

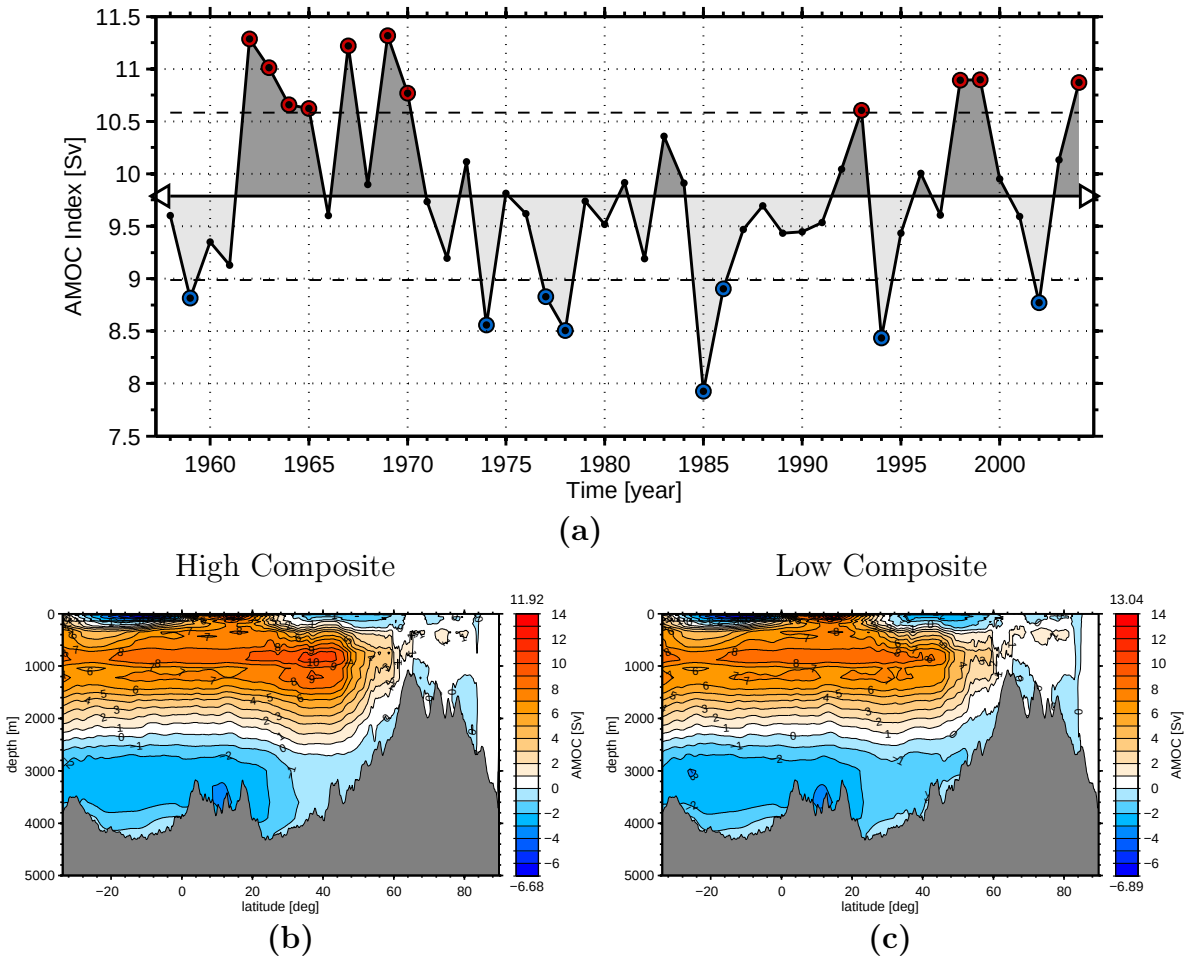

Fig. 5.10: *(a): Annual time evolution of the maximum AMOC at 40°N (black line). The maximum and minimum phase of the AMOC are marked by dark- and light grey shaded areas, respectively. The 75% limits of above (below) standard deviation are indicated by dashed lines. Time slices when the AMOC index was above (below) 75% of standard deviation are marked by red (blue) circles. Black empty triangles mark the value of the time averaged AMOC index.*
(b)-(c): High (b) and low (c) composite maps of the annual mean AMOC with the annual maximum AMOC index (a). The numbers above (below) the colorbar denote the maximum (minimum) values of the wind-driven surface Ekman cells.

mixed layer depth, respectively. In general, four regions with significant mixed layer depth are detected in the North Atlantic Ocean: in the Labrador Sea, in the Irminger Sea, northwest of the British Islands and in the Greenland-Norwegian Sea. The latter region is split into a larger deep-water formation area close to the continental slope of Greenland and smaller spots with increased MLD close the the entrance of the Fram Strait and the coast of Norway. The most dominant deep-water formation areas for high AMOC (Fig. 5.10b) are at the continental slope of eastern Greenland with a MLD of $\sim$ 1000 m and in the Labrador Sea with a MLD of $\sim$ 825 m. The MLD in the remaining two areas in the Irminger Sea and northwest of the British Islands reach only at intermediate depths of $\sim$ 375 m and $\sim$ 525 m, respectively. For low AMOC (Fig. 5.10c) the MLD at the continental slope of eastern Greenland and in the Labrador Sea decreases to a depth of $\sim$ 675 m and 600 m, respectively. The MLD at the continental slope northwest of the British Islands is decreases as well by $\sim$ 100 m during low AMOC.

Fig. 5.11 (c) and (d), shows the modelled and observational climatological March MLD, respectively. Compared with the observational MLD in March our model features quite well the location of the deep-water formation areas in the Labrador Sea, Irminger Sea and Greenland Sea, although the deep convection area in the model Labrador Sea is slightly shifted to the northwest. The increased MLD at the continental slope northwest of the British Islands in the model is shifted in the observational MLD towards Iceland. Furthermore, the model tends to overestimates the magnitude of the MLD in the Labrador Sea and Greenland Sea comparing to the observational data.

Fig. 5.12 shows the difference composite maps (high-low) for the zonal averaged meridional temperature (Fig. 5.12a) and salinity (Fig. 5.12b) profiles in the Atlantic and Arctic Ocean with respect to the annual maximum AMOC index above and below 75% of its standard deviation. Both profiles show a strong positive temperature and salinity anomaly between 44°N-64°N with values of $\sim$ 0.3 °C and $\sim$ 0.04 psu, respectively that reach a depth of $\sim$ 1000 m. The subtropical Atlantic and in the middle Atlantic at $\sim$ 35°N at a depth of 400-900 m show a strong negative temperature and salinity anomaly of ~ -0.7 °C and ~ -0.12 psu, respectively. Also the northern branch between 66°N-78°N indicates a negative temperature anomaly of ~ -0.1 °C.

5.5 Discussion of the ocean model validation

In this chapter we study the ocean model validation for the North Atlantic Ocean of a global FESOM setup designed to resolve the deep water formation areas in the Northern Hemisphere (Labrador Sea, Greenland Sea) as well as in the Southern Hemisphere

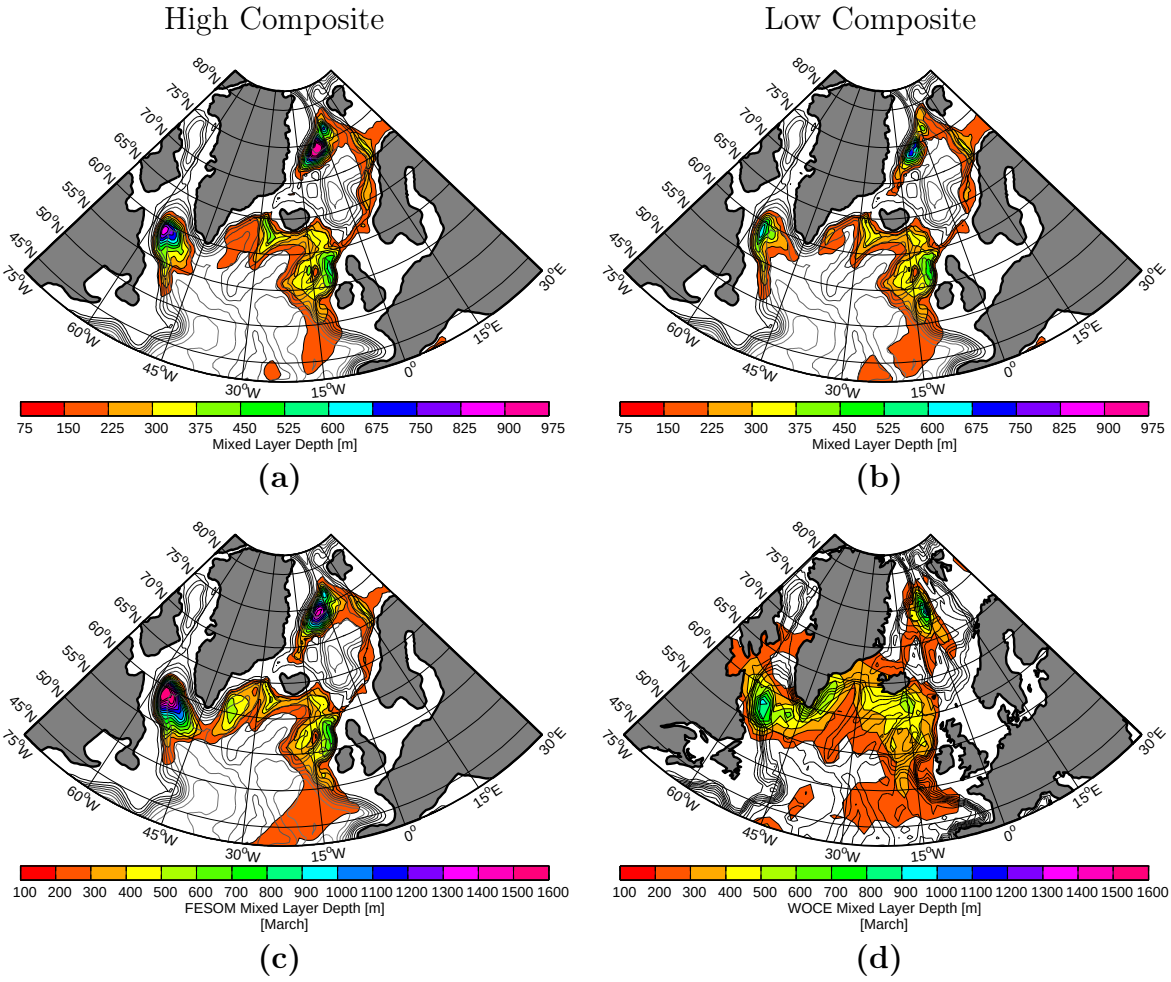

Fig. 5.11: *(a)-(b): High (a) and low (b) composite maps of the winter mean mixed layer depth with annual maximum AMOC index (Fig. 5.10). (c)-(d): Modelled (c) and observed (d) climatological maximum mixed layer depth in March. The observational data are derived from de Boyer Montegut et al. [2004]. Contour lines indicate the bottom topography in steps of* 500 *m.*

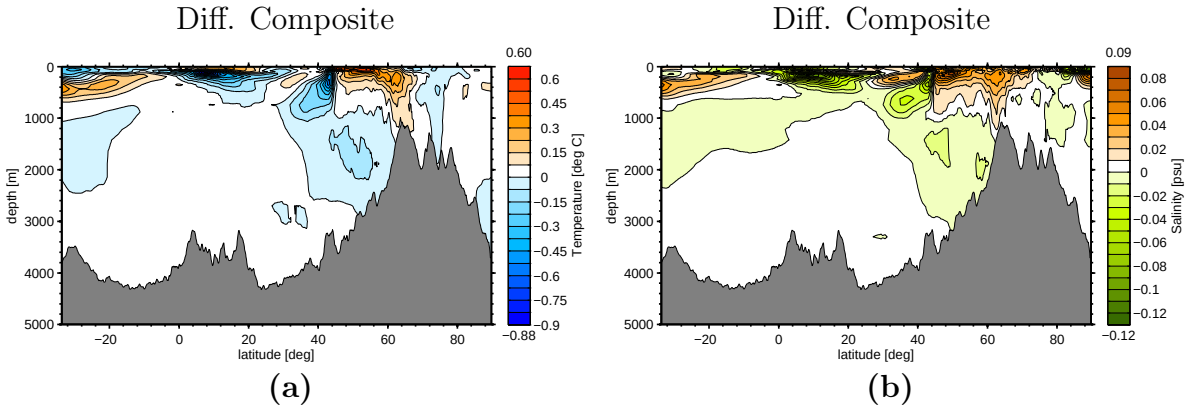

Fig. 5.12: *Difference composite maps (high-low) of the monthly mean meridional Temperature (a) and Salinity (b) profile with annual maximum AMOC index (Fig. 5.10).*

(Weddell Sea, Ross Sea) with locally refined resolution in a global context.

The comparison of model and OWS data [*Levitus et al.*, 1994; *Lohmann et al.*, 2008] shows a reasonable good agreement of the temperature and salinity time series especially at the higher resoluted position of the OWS-B. Although the surface temperature and salinity in our model is mostly prescribed by the forcing, we are able to reproduce very well the vertical signal of the GSA event that occupied the Labrador Sea in the early 1970s and was captured by the OWS-B [*Dickson et al.*, 1988; *Haak et al.*, 2003]. At the position of the OWS-C, where the resolution is already coarser, the model tends to overestimate the salinity by around 0.1-0.3 psu. The offset in the intermediate ($125-520$ m) and deep layers of the temperature time series but also the general offset in the salinity time series is mostly related to a shift in the ocean circulation pattern due to the coarser mesh.

GSA events or negative salinity anomalies are substantial signals in the North Atlantic Ocean which had a far-reaching influence on many aspects of the climate. The model features several negative salinity anomalies that pass the Denmark Strait around 1967, 1976, 1987 and 1995 and coincide with a high sea-ice volume export from the Arctic region. Long term observations of the Denmark Strait salinity document similar negative anomalies around 1967, 1978 and 1995 [*Dickson et al.*, 2002; *Eldevik et al.*, 2009]. The analysis of the DSOW and ISOW volume transport revealed for both water masses a mean transport of approximately 1.4 Sv. Observational estimations of the DSOW

transport [*Girton and Sanford*, 2001; *Macrander et al.*, 2007; *Sarafanov et al.*, 2009] suggest a general stronger overflow in the range of 2.5 Sv-3.0 Sv. Further, the modelled mean salinity range of the DSOW (34.78 psu) and ISOW (34.89 psu) is to fresh compared to observed estimates, which suggest a DSOW and ISOW salinity in the range of $34.88 - 34.94$ psu and $34.98 - 35.03$ psu, respectively [*Warren and Wunsch*, 2007]. The model generally tends to underestimate the transport and salinity of the DSOW and ISOW overflows, which is an explanation for the reduced strength and size of the upper AMOC circulation cell in the model as described by different authors [e.g., *Döscher and Redler*, 1997; *Latif et al.*, 2006; *Zhang et al.*, 2011]. Nevertheless, the underlying trends and variabilities in the salinity time-series of the DSOW overflow water matches well the observation of *Dickson et al.* [2002], which reveal a freshening trend of the DSOW over the last four decades as well as a salinity minimum in the late 1970s to early 1980s. Further the modelled time evolution of the DSOW volume transport features a distinct interannual to decadal variability as its mentioned in the first long-term overflow observation at the Denmark Strait by *Macrander et al.* [2005].

The negative salinity anomalies that are passing the Denmark Strait with the East Greenland Current enter subpolar gyre and reach the Labrador Sea around 2 to 3 years later. Here they cause the Great Salinity Anomaly (GSA) events, which result in a reduction of the vertical ventilation of cold and fresh water [*Dickson et al.*, 1988]. After the negative salinity anomalies are passing the Labrador Sea they recirculate further within the subpolar gyre. The most pronounced negative salinity anomaly in the model that passed the Denmark Strait around 1967 can be tracked through their whole pathway in the subpolar gyre and needs around $8 - 9$ years to finally recirculate with the North Atlantic Current (NAC) over the Iceland-Scotland Ridge back to the Greenland Sea. The estimated travel times within the subpolar gyre agree well with the GSA travel times mentioned by *Belkin et al.* [1998]. The GSA events in the model, which coincides with a high sea ice transport from the Arctic, agrees with the findings of *Haak et al.* [2003], who showed that all GSAs are remotely triggered by abnormal sea-ice and freshwater exports from the Arctic. It is noted that in their model configuration, the surface salinity was restored to climatological values. The other two simulated GSA events at the beginning of the 1980s and 1990s are in agreement with the findings of [*Belkin et al.*, 1998; *Häkkinen*, 2002; *Belkin*, 2004].

The negative temperature and salinity anomalies of the early 1960s and 1990s are both related to an enhanced heat loss in the Labrador Sea due to a strong positive phase of the North Atlantic Oscillation (NAO). This produced cold and dense surface waters which favoured a deep ventilation of cold and fresh water [*Yashayaev*, 2007; *Yashayaev and Loder*, 2009].

Our model run features an oscillation between a high and low AMOC phase, where the high AMOC phase is characterized by a strong deep convection in the Labrador- and Greenland Sea, while the low AMOC phase shows a massive drop in the mixed layer depth of these two regions. A waxing and waning of Labrador Sea and Greenland Sea deep convection is documented in observational evidences by several authors [*Schlosser et al.*, 1991; *Dickson et al.*, 1996]. CMA of the horizontal temperature and salinity distributions with respect to the maximum AMOC index (not shown) revealed that the positive temperature and salinity anomalies between 44°N-64°N are caused by an increased meridional heat transport and deep convection of the warm and salty North Atlantic waters at the continental slope northwest of the British Isles and southwest of Iceland. Because the AMOC is a crucial limb of the global conveyor belt and its responsible for transporting heat and salt into the high latitudes, a weakening of this circulation causes also a reduction in the heat and salt transport northward. The composite maps (High - Low) of the mean meridional temperature and salinity profile features in the subtropical and middle Atlantic, at $\sim 35^{\circ}$N and a depth of $400-900$ m, a strong negative temperature and salinity anomaly of ~ -0.7 °C and ~ -0.2 psu, respectively. These anomalies are caused by an accumulation of heat and salt in the tropical and subtropical Atlantic during the low AMOC state and the reduced northward transport of heat and salt. The negative temperature anomaly of ~ -0.1 °C between 66°N - 78°N is related to the strong MLD and the associated intensified deep ventilation of cold surface waters in the northern Greenland Sea for the high AMOC phase. For the low AMOC, the MLD in that area is clearly reduced, which also reduces the deep ventilation and causes warmer temperatures there.

5.6 Conclusions of the model validation

The model setup used in this thesis (see section 2.2) is able to reproduce large scale features of the ocean circulation and with the ability of locally refined resolution it can simulate the main characteristics of the deep water formation. From the validation of our model setup we can summarize:

(1) The sea-ice model produces realistic sea ice concentration on both hemispheres and is able to generate a sea ice variability that is in good agreement with observational data [*Schmith and Hansen*, 2003; *Fetterer et al.*, 2002, updated 2009].

(2) On the basis of a comparison with OWS data, we could prove that the model setup performs very well in areas with a high resolution.

(3) The model features the fingerprint of several GSA events in the vertical that are also documented in observational data by several authors [*Dickson et al.*, 1988; *Belkin et al.*, 1998; *Belkin*, 2004].

(4) The analysis of the Denmark Strait cross section indicates that the model captures the freshening trend of the last four decades in the North Atlantic as its described by *Dickson et al.* [2002].

(5) The model generally tends to underestimate the strength and salinity of the Nordic Sea overflows, which could be an explanation for the slenderness and weakness of the upper AMOC circulation cell.

(6) The model shows a pronounced variability in the AMOC which is accompanied by a corresponding fluctuation in the deep water formation of the Labrador Sea and Greenland Sea.

AWI Alfred-Wegener-Institut für Polar- und Meeresforschung in der Helmholtz-Gemeinschaft

6 Validation of Labrador Sea Water formation in a global FESOM setup, based on a comparison with observational data

In the Labrador Sea basin a major component of the cold limb of the Atlantic meridional overturning circulation (AMOC) is formed [e.g., *Rhein et al.*, 2011]. The intermediate water mass that is part of this deep convection process is the Labrador Sea Water (LSW) which can be separated into two different classes: the deep LSW (dLSW), in some publications referred as "classical LSW", and the less dense upper LSW (uLSW) [e.g., *Rhein et al.*, 2002; *Stramma et al.*, 2004; *Kieke et al.*, 2006]. Both LSW modes are formed by convection, which is accompanied by a strong surface cooling during winter conditions. This formation leads to an increase in the near-surface density and to an unstable stratification and a homogenization of the water column. The formation of LSW is crucial for the heat and freshwater exchange between the atmosphere and deep ocean layers as well as for the oceanic input of anthropogenic tracers like chlorofluorocarbons (CFC) due to vertical ventilation in the ocean [*Kieke et al.*, 2006]. The formation of either uLSW or dLSW, that means the extent of the deep convection, depends on various factors. One major factor is the intensity of deep convection in the preceding winter and the amount of horizontal advection of heat and salt which mainly influence the density stratification in the Labrador Sea [*Yashayaev*, 2007]. This determines how much buoyancy flux is necessary to transform water of a certain density. Another major factor is the strength of the atmospheric forcing in winter which provides the necessary buoyancy forcing to form either uLSW or dLSW. Many authors [*Dickson et al.*, 1996; *Pickart et al.*, 2003; *Yashayaev et al.*, 2007a] suggest that the last factor is mostly controlled by the strength of the North Atlantic Oscillation (NAO).

The NAO index is defined as the normalized pressure gradient between the Azores High and the Icelandic Low [*Hurrell*, 1995]. Other factors that can affect the formation of dLSW or uLSW are the density stratification that remains from preceding winters or large fresh water pools that propagate within the subpolar gyre like the Great Salinity Anomaly (GSA) of 1970 described by [*Dickson et al.*, 1988] or the later salinity anomalies described by [*Belkin et al.*, 1998; *Belkin*, 2004].

Due to the harsh weather conditions, the temporal and spatial availability of ship data for the Labrador Sea, especially regarding the properties of the LSW, is limited especially to the summer season. At this point, numerical ocean model approaches with high resolutions provide the possibility to analyse the spatial and temporal variability patterns. Such model allow to investigate the processes and mechanisms responsible for setting the strength of the deep-water formation, especially in regions that are usually difficult to access.

In the recent years regional model studies regarding the ventilation and transformation of LSW have been carried out [e.g., *Böning et al.*, 1996; *Marshall and Schott*, 1999; *Brandt et al.*, 2007]. However, regional modelling has the necessity to predefine boundary condition at the open domain borders. The complexity of these boundary conditions is of course limited, which in turn restricts the degrees of freedom (DOF) of the model. In contrast, global model studies do not have this restriction and allow to analyse the full variability of a model in a global context. Due to the high numerical costs global setups are usually limited in their resolution and have deficiencies in reproducing regional effects. The FESOM model approach which is used in this thesis provides the opportunity to local increase the resolution in an otherwise global setup [*Scholz et al.*, submitted, 2012].

In this chapter we will focus on the ability of the global FESOM setup which is introduced in section 2.2 and general validated in chapter 4 and 5 to reproduce a realistic deep water formation in the Labrador Sea. Therefore, we analyse the variability in the different LSW modes in our model and compare the results to LSW layer thickness time-series derived from hydrographic observations from the central Labrador Sea [*Kieke et al.*, 2006; *Rhein et al.*, 2011]. The approximated mesh resolution of the global setup in the Northwest Atlantic is shown in Fig. 6.1a.

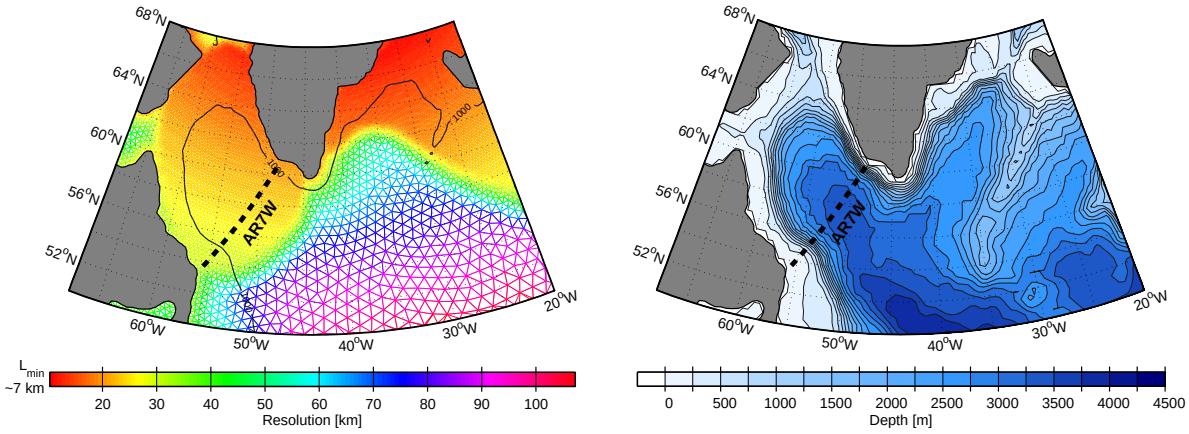

(a) (b)

Fig. 6.1: *Regional resolution (a) and bottom topography (b) of the global model setup in the Northwest Atlantic Ocean. The dashed line marks the position of the AR7W cruise line [Lazier et al., 2002].*

For the analysis of the Labrador Sea Water variability we use the forcing adjustments to the normal focing setup (see section 2.3) as described in section 2.5. Although the temporal coverage of the so performed model simulation is from 1958-2007 we will focus in this study on the time interval 1988-2007, which is characterized by an exceptional high activity in the change of the Labrador Sea Water formation [*Kieke et al.*, 2006; *Yashayaev et al.*, 2007a].

6.1 LSW index derived from hydrographic observations

For the comparison between model and experimental data we analyse the layer thicknesses of uLSW and dLSW as calculated by *Kieke et al.* [2006] and *Rhein et al.* [2011] for the central Labrador Sea. They reconstructed an uLSW and dLSW layer thickness time series from different hydrographic databases (Bedford Institute of Oceanography, Hydrobase, National Oceanographic Data Center, WHPO, SFB 460 and BMBF Nordatlantik) for the period from 1948-2009 by choosing profiles from the central Labrador Sea close to the position of the former Ocean Weather Station Bravo (OWS-B, 56°30′N,

51° W). The applied methods for the data acquisition and selection are described in *Kieke et al.* [2006]. We use this historical time series of the dLSW and uLSW layer thickness to cover the period from 1988-2004. The time-series of the dLSW and uLSW layer thicknesses is directly connected to the formation of the corresponding water mass and can therefore act as an index for the produced LSW mode volume. The period from 1988-1996 is of potential importance because the atmospheric forcing has its strongest influence on the convective activity in the Labrador Sea [*Yashayaev et al.*, 2007a; *Rhein et al.*, 2011]. To quantify the strength of the westerly wind, we use the NAO index derived from the COREv2 SLP via the normalized pressure gradient between the Azores High and the Icelandic Low [*Hurrell*, 1995].

In general, different definitions for LSW limits can be found in the literature [e.g., *Pickart et al.*, 2002; *Stramma et al.*, 2004]. To ensure a better comparability of modelled and measured LSW properties, we followed the definitions of *Stramma et al.* [2004] and *Kieke et al.* [2006, 2007] and define the density range $\sigma_\theta = 27.68 - 27.74\,\mathrm{kg\,m^{-3}}$ as uLSW, and $\sigma_\theta = 27.74 - 27.80\,\mathrm{kg\,m^{-3}}$ as the dLSW layer. They first oriented on the Labrador Sea Water mass definition of *Pickart et al.* [1997] (uLSW: $\sigma_\theta = 27.68 - 27.72\,\mathrm{kg\,m^{-3}}$, dLSW: $\sigma_\theta = 27.75 - 27.78\,\mathrm{kg\,m^{-3}}$) and adapted their definition for the water mass limits for an optimal distribution of the water mass characteristics especially in the mid-1990s when their measurements began [*Stramma et al.*, 2004]. They used the same upper limit for the uLSW as *Pickart et al.* [1997] but decided to define a new lower uLSW limit to have a common boundary with the dLSW. *Stramma et al.* [2004] also found that a lower dLSW boundary of $\sigma_\theta = 27.80\,\mathrm{kg\,m^{-3}}$ is a reasonable better approximation for the period of the mid-1990s.

6.2 Modelled Mixed Layer Depth in the Northeast Atlantic Ocean

Fig. 6.2a shows the model mixed layer depth in spring (MAM), when the northern hemispheric deep convection has its highest values, averaged over the years 1988-2007. There are three major deep convection areas which are located in the Labrador Sea, Irminger Sea and at the continental slope southwest of Iceland. The most important convective area in the northwestern Atlantic Ocean is located in the Labrador Sea with

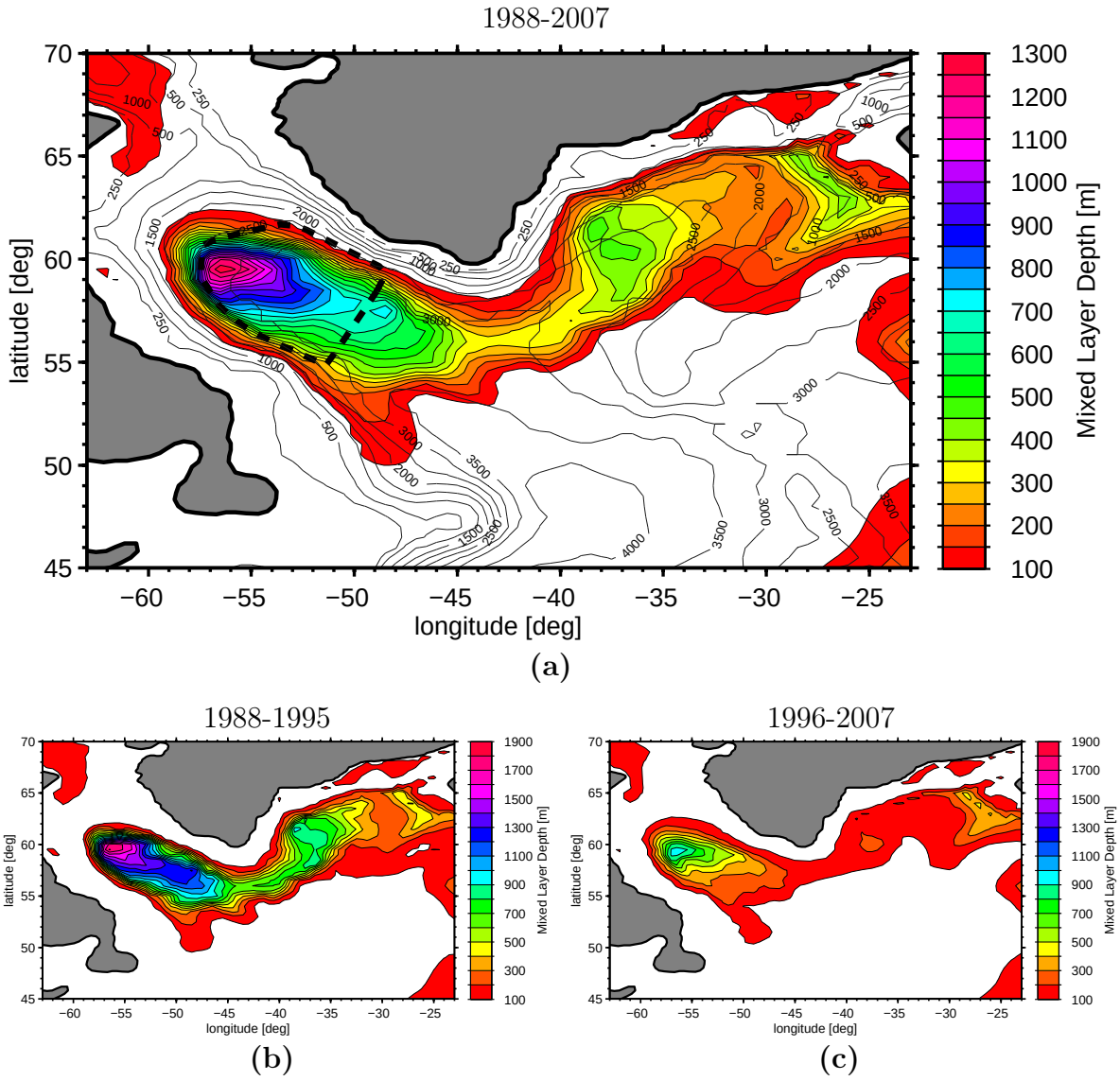

Fig. 6.2: *(a) North Atlantic Ocean mean mixed layer depth* $\geq$ *50 m for boreal spring (MAM) season when the mixed layer depth has its highest values, averaged over the period 1988-2007. Superimposed is the bottom topography (black contour line) of the model and the area (dashed line) for the time evolution indices in Fig. 6.3 and Fig. 6.4.*
(b)-(c): Mean mixed layer depth for spring, averaged over the years 1988-1995 (b) and 1996-2007 (c).

a maximum mean spring mixed layer depth of $\sim$ 1300 m. The modelled center of the maximum convective cell in the Labrador Sea is not located in the central Labrador Sea at the maximum depth of 3300 m, being shifted northwestward to 59.5°N, 65.5°W at a bottom depth of $\sim$ 2750 m. In the Irminger Sea and southwest of Iceland, the mixed layer depth is shallower and reaches only a maximum value of $\sim$ 450 m. Over the time period from 1988 to 2007 the mixed layer depth in the northwestern Atlantic shows a strong change (Fig. 6.2b, 6.2c). Fig. 6.2b shows the mean mixed layer depth for the time period from 1989-1995. This period is characterized in the model by an intensified convection in the northwestern Labrador Sea, Irminger Sea and south of Greenland. The mixed layer depth in the Labrador Sea and Irminger Sea, reaches a maximum depth of $\sim$ 1849 m and $\sim$ 974 m, respectively. The following period from 1996-2007 (Fig. 6.2c) is characterized by a drastic decrease in the deep convection at the northwestern Atlantic Ocean. The mixed layer depth in the Labrador Sea declines by a factor of almost two, from 1849 m to 936 m. The decline in the Irminger Sea is even stronger, the mixed layer depth drops from 974 m to 233 m.

To select the areas for the calculation of dLSW and uLSW index we apply the same methodology as *Kieke et al.* [2006]. They have used only those hydrographic profiles located in the vicinity of the AR7W cruise line, a hydrographic repeat section crossing the central Labrador Sea and the Ocean Weather Station Bravo where the bottom topography exceeded 3300 m. Due to the fact that the modelled location of the convective area in the Labrador Sea is shifted to the northwest, we expand our area for the calculation of the indices. We select a box from the northwestern boundary until the position of the AR7W cruise line and identify all surface nodes that were located within this box. To further eliminate the influences of the boundary currents, like in *Kieke et al.* [2006], we exclude from the remaining surface nodes all surface nodes with a bottom depth shallower than 2500 m. The area of the resulting surface nodes includes now the central Labrador Sea and the area with the highest mixed layer depths (Fig. 6.2a, dashed contour line). Tests with different index definition areas revealed that the results are less influenced by the exact size of the index definition area.

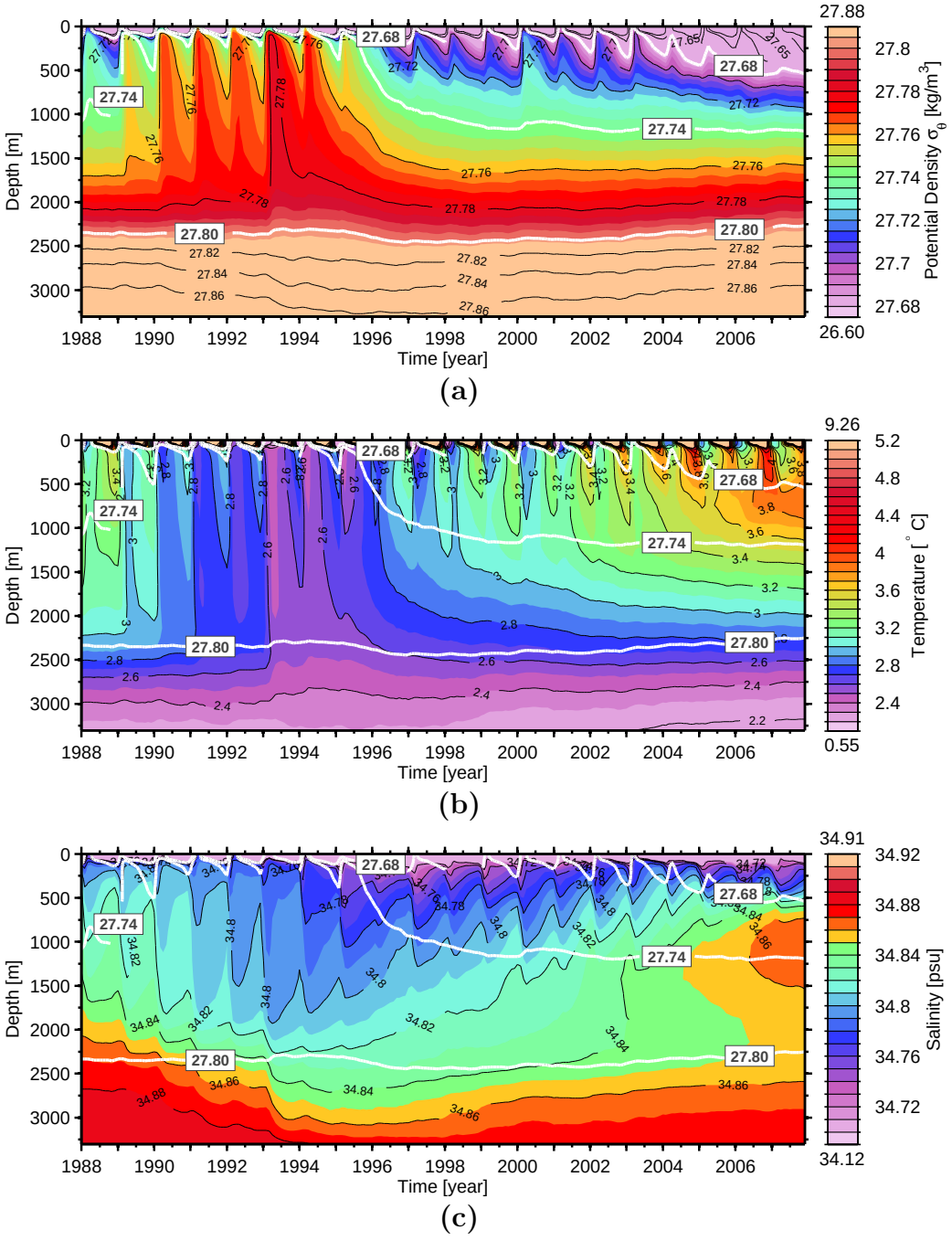

Fig. 6.3: *Time evolution of the monthly mean potential density (a), temperature (b) and salinity (c) over depth at the central Labrador Sea index area (Fig. 6.2) for the years 1988-2007. Thick white lines indicated the* $\sigma_\theta = 27.68\ kg\,m^{-3}$, $\sigma_\theta = 27.74\ kg\,m^{-3}$ *and* $\sigma_\theta = 27.80\ kg\,m^{-3}$ *isopycnals to separate between light (uLSW) and dense (dLSW) Labrador Sea Water.*

6.3 Modelled Labrador Sea Hydrography

Fig. 6.3 shows the development of the model potential density $\sigma_\theta(z,t)$, temperature $T(z,t)$ and salinity $S(z,t)$ for the index definition area (Fig. 6.2a, dashed contour) over time and depth for the period from 1988 to 2007. The isopycnals of $\sigma_\theta = 27.68\,\mathrm{kg\,m^{-3}}$, $27.74\,\mathrm{kg\,m^{-3}}$ and $27.80\,\mathrm{kg\,m^{-3}}$, which are used for the definition of the dLSW and uLSW, are indicated as thick lines.

The time evolution of the potential density over depth (Fig. 6.3a) changes considerably during this time range. As described by other authors [e.g., *Kieke et al.*, 2006; *Yashayaev*, 2007; *Yashayaev and Loder*, 2009], the model reproduces two, quite different periods. The first period, from 1989-1995, is characterized by a gradual increase in the potential density of around $\Delta\sigma_\theta = 0.04\,\mathrm{kg\,m^{-3}}$ at intermediate depths with a maximum of $27.8\,\mathrm{kg\,m^{-3}}$ around 1993. For each winter in the time span from 1989-1995, the dLSW layer (between the $\sigma_\theta = 27.74 - 27.8\,\mathrm{kg\,m^{-3}}$ isopycnals) has a connection to the cold surface layers. This has led to a fast build up of a homogeneous cold, fresh and dense water body, reaching from the surface to a depth of 2000 m. The winters 1993 and 1994 reveal an exceptional strong vertical ventilation. In these two years the coldest and freshest water is ventilated down to a depth greater than 2000 m. It should be mentioned that in comparison to the abrupt decrease in temperature (Fig. 6.3b), the salinity (Fig. 6.3c) features a more gradual decrease. This suggests that the underlying mechanism that dominates the decrease in salinity is different from a fast vertical deep convection process and will be discussed in section 6.6.

At the beginning of the second period from 1996-2007, the dLSW mode water starts to get isolated from the surface and the supply of cold and fresh waters (Fig. 6.3a). The horizontal mixing with a warmer and more saline Labrador Sea Boundary Current system (LSBC) that consists of the West Greenland Current in the northeast and the Labrador Current in southwest, leads to a gradual decrease of the density in intermediate depths and a lowering of the $\sigma_\theta = 27.74\,\mathrm{kg\,m^{-3}}$ isopycnal of ~ 700 m until 1998. After that, the $\sigma_\theta = 27.74\,\mathrm{kg\,m^{-3}}$ isopycnal remains at a level of ~ 1200 m. The mean depth of the $\sigma_\theta = 27.68\,\mathrm{kg\,m^{-3}}$ isopycnal between 1996 and 2002 remains at a mean level of ~ 120 m. During the same time, the strong increase in the depth of the $\sigma_\theta = 27.74\,\mathrm{kg\,m^{-3}}$ isopycnal indicates a thickening of the lighter uLSW layer. After

2002 the mean depth of the $\sigma_\theta = 27.68\,\mathrm{kg\,m^{-3}}$ isopycnal shows a continuous sinking until a depth of ~ 500 m. The sinking of the $\sigma_\theta = 27.68\,\mathrm{kg\,m^{-3}}$ isopycnal, that means the accumulation of less dense water on the surface and the suppressed heat and salinity exchange of deep ocean layers in that time (Fig. 6.3 (b), (c)) might indicate the occurrence of a GSA-like event in the model towards the end of the simulation period. After 2004 the ocean levels between 500 m and 1500 m warm up by 0.4 °C and an increase in the salinity is detected. This can be an indicator for a reduction of the wintertime deep convection, which ventilated the cold and fresh surface waters downward.

6.4 Labrador Sea - model data comparison

6.4.1 Comparison of simulated and observed LSW layer thickness

Fig. 6.4 shows the time evolution of the monthly uLSW and dLSW layer thickness of the model (thin line), the 3 year-running-mean filtered time series (thick line) and the summer layer thicknesses estimated from observational data (filled) [*Kieke et al.*, 2006, 2007; *Rhein et al.*, 2011]. The positive and negative phase of the 3 year-running-mean filtered NAO index is shown by dark and light grey shaded areas, respectively. The simulated and observed dLSW and uLSW layer thicknesses are in good agreement. Both time series of simulated and observed dLSW (uLSW) show an increase (decrease) in the layer thickness between 1988-1990. A big homogeneous dLSW body is build up and the system gets "charged with dense water" from the surface and is undergoing a transition to deep convection depths. In comparison to the observations, the model seem to have a slightly higher dLSW layer thickness. Between 1990-1994 the simulated and measured layer thicknesses reveal that the Labrador Sea remained for several years in the deep convection phase, when the dLSW and uLSW layer thickness reaches its maximum and minimum value, respectively. The maximum and minimum values of the simulated and observed dLSW and uLSW layer thickness are in close proximity. In the period from 1995-1999, the data of the simulated and observed layer thicknesses show a gradual transition to thinner dLSW layer thicknesses. The dLSW index in Fig. 6.4 and the temporal evolution of the potential density and temperature in Fig.

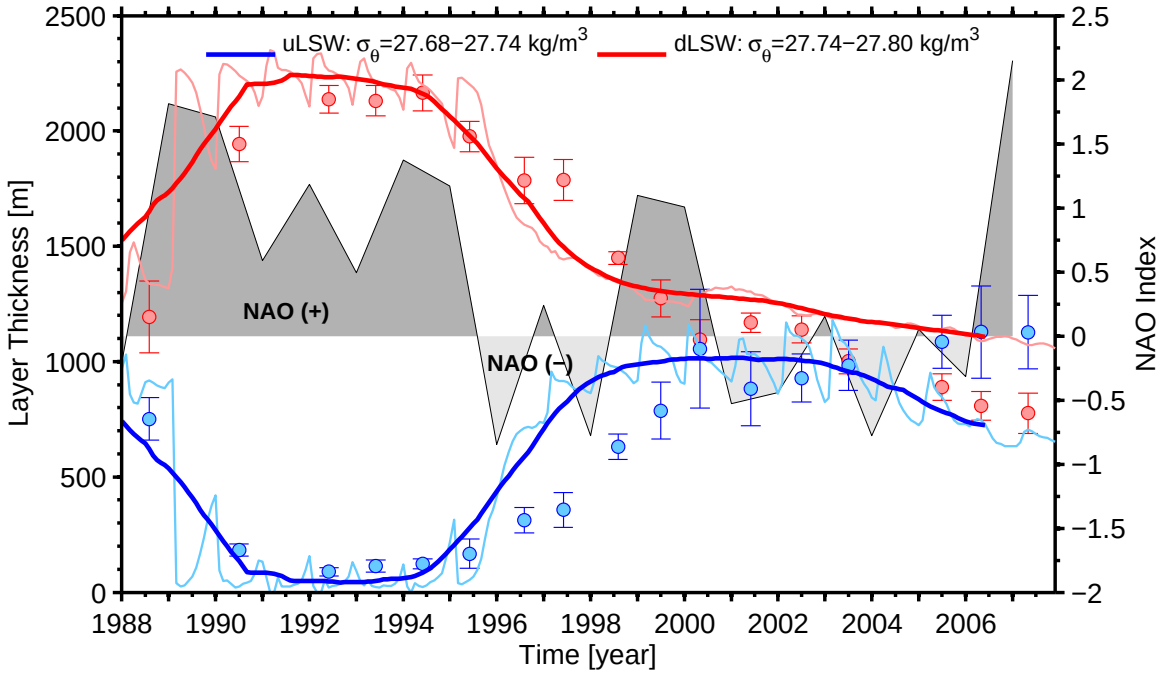

Fig. 6.4: *Temporal evolution of the layer thickness of upper and deep Labrador Sea Water (LSW) for the years 1988-2007. Blue: upper LSW (uLSW), bounded by the isopycnals* $\sigma_\theta = 27.68 - 27.74\ kg\,m^{-3}$*; Red: deep LSW (dLSW), bounded by the isopycnals* $\sigma_\theta = 27.74 - 27.80\ kg\,m^{-3}$*. The monthly values and the 3 year-running-mean filtered dLSW and uLSW data of the model run are shown by thin and thick lines, respectively. The dLSW and uLSW time series derived from observations are shown as filled circles including the uncertainties [Rhein et al., 2011]. The positive and negative phase of the normalized winter (DJF) NAO index derived from the COREv2 data set [Large and Yeager, 2009] are indicated by dark- and light grey areas, respectively.*

6.3 reveal that the system does not react instantaneous to a change in the winds as indicated by the NAO index. After 1995, production of the uLSW increases at the cost of the dLSW production. The increase in the layer thickness of the model uLSW layer seems to be more rapidly, compared to the measurements and reaches a clear maximum between winter 1999 and summer 2002, with a layer thickness of $\sim$ 1000 m. After 2002, the uLSW layer thickness of the model decreases again. This is caused by a sinking of the $\sigma_\theta = 27.68\ \mathrm{kg\,m^{-3}}$ isopycnal and the accumulation of less dense water in

the surface layers that might be triggered by the formation of a new GSA-like event in the Labrador Sea. The uLSW layer thickness calculated via the profile data shows no clear maximum and increases gradually from 1995 until 2007. In the period from 1995 until 1999 the decrease in the layer thickness of the dLSW mode water is quite similar between the simulated and observed values. After 1999 the decrease of the model dLSW layer thickness slows down, while the observed layer thickness decreases further.

6.4.2 Comparison of model and measured Labrador Sea AR7W cruise sections

Due to rough winter conditions in the Labrador Sea, most available cruise sections were measured in late spring to late summer. We compare two simulated and measured hydrographic AR7W sections of the World Ocean Circulation Experiment (WOCE) [*WOCE Data Product Committee*, 2002] that took place in a year of strong and weak dLSW formation. We choose the R/V Hudson cruise 93019/1 in June 1993 and the R/V Hudson cruise 99022/1 in July 1999 as a representative for an event with thicker and thinner dLSW layer thickness (Figs. 6.5 (a), (b)), respectively. Figs. 6.5 (c), (d) show the corresponding AR7W cross sections in the model. Data from the AR7W line in June 1993 (Fig. 6.5a) show a thick layer of dLSW mode water. This massive dLSW body was gradually built up by a strong vertical mixing in the spring of 1993 and an intense winter time convection in the preceding three years. The observational data feature a maximum dLSW layer thickness of 2150 m in the central Labrador Sea and a minimum dLSW layer thickness of $\sim$ 1000 m on the continental slope. The uLSW mode water has here a very limited thickness of around 200 m. Fig. 6.5c shows the corresponding cross section in the model run. On the first view, there is a difference between the measured and simulated cruise section. In the western part of the model Labrador Sea a lighter water body reaches from $\sim$ 300 m down to a depth of 2200 m. The lighter water body is a direct consequence of the northwestward shift of the deep convection area in the model (see Fig 6.2b). Fig. 6.6a shows a horizontal mean density distribution in the northwest Atlantic, which indicates that the dense water is more concentrated on the northwestern part of the Labrador Sea. This leads in the model to the formation of a tongue of lighter water in the southern part of the Labrador

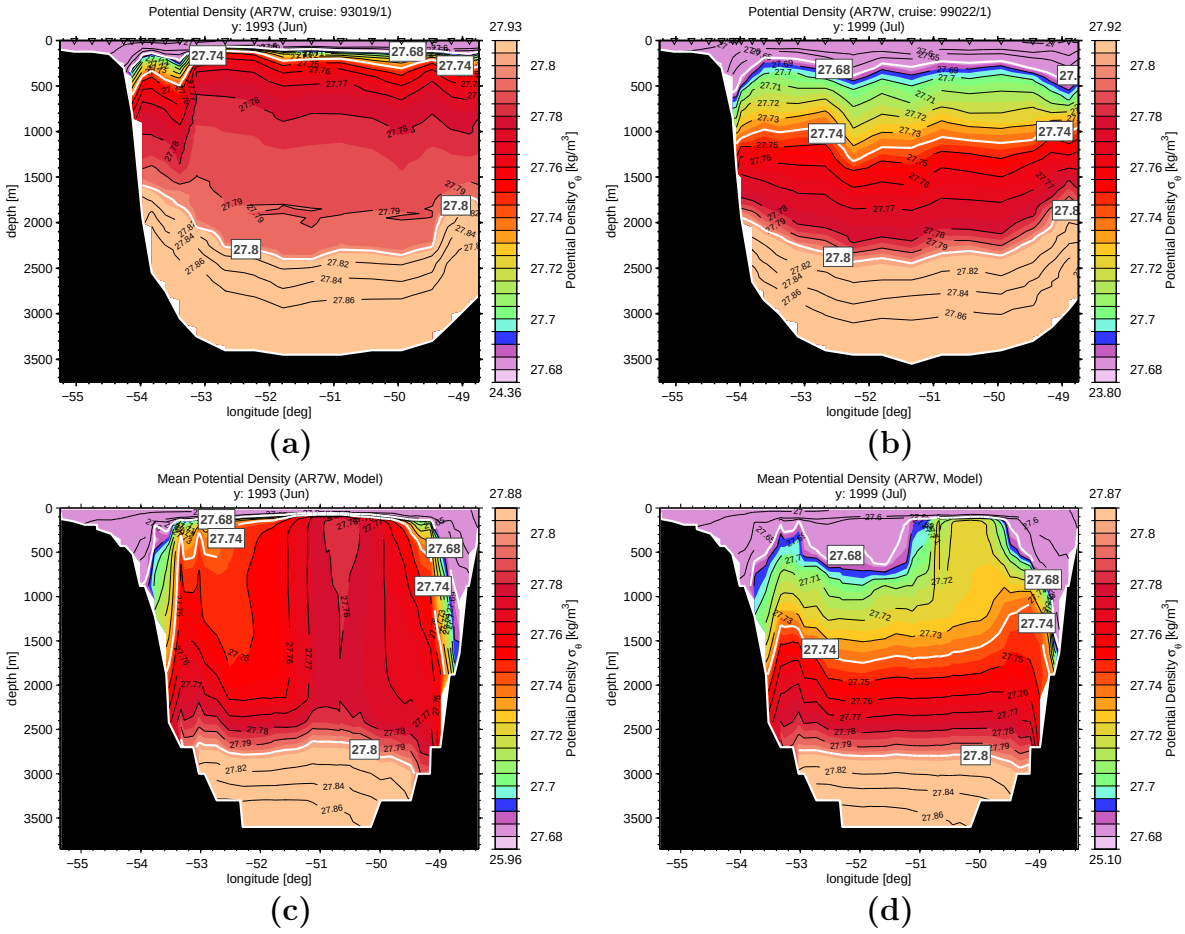

Fig. 6.5: *Potential density of the observed [Boyer et al., 2009] (a)-(b) and modelled (c)-(d) AR7W cross sections in June and July for years with a thicker (1993, left column) and thinner (1999, right column) dLSW layer thickness. Thick white lines indicate the* $\sigma_\theta = 27.68\ kg\,m^{-3}$, $\sigma_\theta = 27.74\ kg\,m^{-3}$ *and* $\sigma_\theta = 27.80\ kg\,m^{-3}$ *isopycnals to separate between uLSW and dLSW.*

Sea, which is crossed by the AR7W line. Nevertheless, the potential density of this tongue is still in the defined range of the dLSW. Due to this fact, the position of the $\sigma_\theta = 27.68$, 27.74 and 27.80 $\mathrm{kg\,m^{-3}}$ isopycnals and the layer thickness of the dLSW and uLSW are hardly affected. The depth of the $\sigma_\theta = 27.8\ \mathrm{kg\,m^{-3}}$ isopycnal within the model is around 350 m lower than in the observed cruise section. This is related to an insufficient production rate of Denmark Strait Overflow water (DSOW) in the model, which is usually the main contributor to the densest and deepest water mass in the

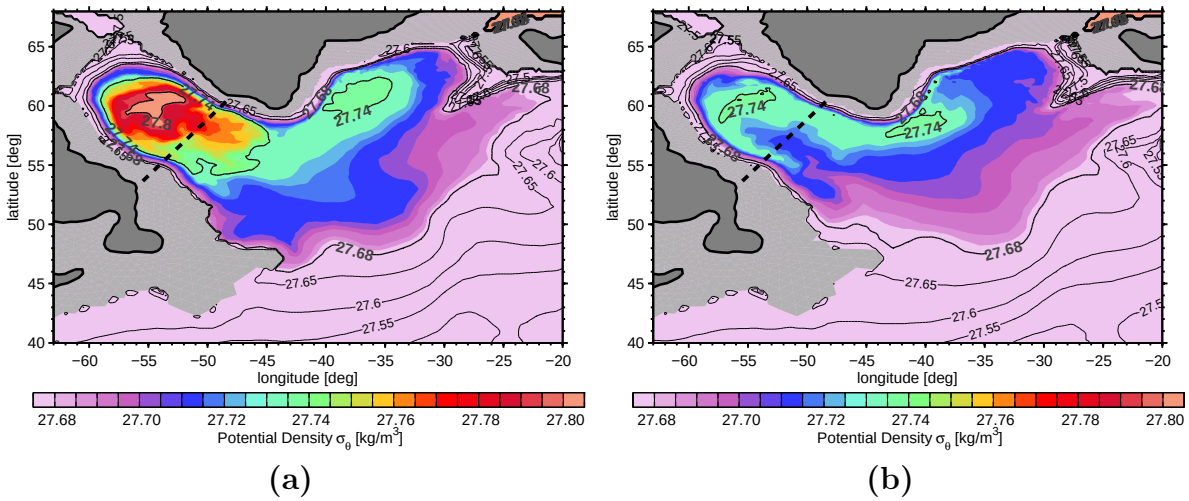

Fig. 6.6: *Horizontal mean potential density of the model data in the northwest Atlantic Ocean averaged over a depth from 500 m - 1000 m. In (a): June 1993 and (b): July 1999 for events with thicker and thinner dLSW layer thickness, respectively. Thick lines indicate the* $\sigma_\theta = 27.68\ kg\,m^{-3}$, $\sigma_\theta = 27.74\ kg\,m^{-3}$ *and* $\sigma_\theta = 27.80\ kg\,m^{-3}$ *isopycnals. The dashed line marks the location of the AR7W cruise line.*

Labrador Sea. But the depth of the measured and simulated $\sigma_\theta = 27.68$, $27.74\ \mathrm{kg\,m^{-3}}$ isopycnal in the central Labrador Sea is quite similar. On the eastern and western boundary of the Labrador Sea the $\sigma_\theta = 27.68$, $27.74\ \mathrm{kg\,m^{-3}}$ isopycnals differ from the measured cruise section, but this is also a consequence of the northwestward shift of the deep convection cell in the model.

The AR7W cruise section in July 1999 (Fig. 6.5b), shows, in comparison to 1993, a quite thick uLSW layer, with an average layer thickness of $\sim$ 850 m. The thickness of the dLSW layer has decreased clearly and lost its winter connection to the surface layers (Fig. 6.3a). This decrease occurs due to the deepening of the $\sigma_\theta = 27.74\ \mathrm{kg\,m^{-3}}$ isopycnal. Also the depth of the $\sigma_\theta = 27.68\ \mathrm{kg\,m^{-3}}$ isopycnal deepens by $\sim$ 200 m in the central Labrador Sea. The depth of the $\sigma_\theta = 27.8\ \mathrm{kg\,m^{-3}}$ isopycnal remains almost the same between summer 1993 and 1999. The corresponding model section of July 1999 (Fig. 6.5d) shows a similar behaviour. We can see an increase in the uLSW layer thickness especially in the eastern Labrador Sea where water mass production occurs in the model. The western Labrador Sea has a lower uLSW layer thickness, which is

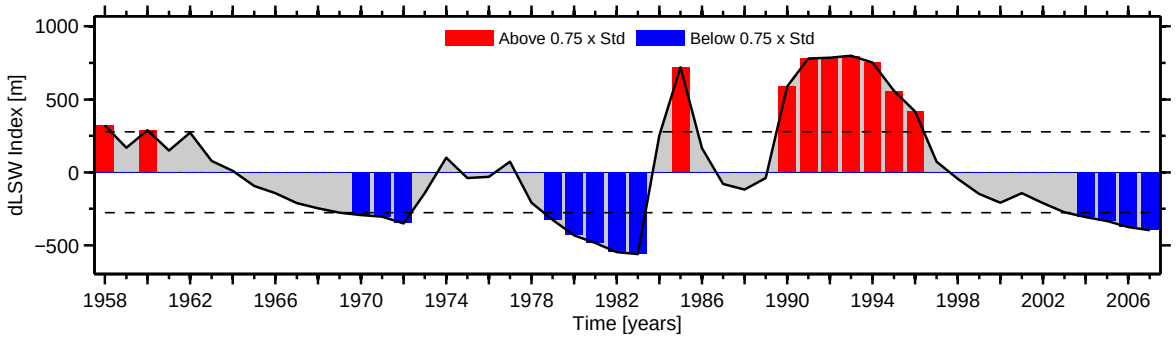

Fig. 6.7: *Detrended winter (DJF) seasonal dLSW index (solid line) and the 75% of standard deviation limits (dashed lines). Time slices when the dLSW layer thickness was above and below 75% of standard deviation are marked by red and blue bars, respectively. These time slices are used in the composite map analysis (CMA) (Figs. 6.8, 6.9, 6.10 and 6.11b).*

again a consequence of the northwestward shift of the deep convection area (see Fig. 6.6b). The $\sigma_\theta = 27.74\,\mathrm{kg\,m^{-3}}$ isopycnal sinks down to a depth of ~ 1600 m, while the $\sigma_\theta = 27.8\,\mathrm{kg\,m^{-3}}$ isopycnal remains at the same depth. This leads to a decrease in the dLSW layer thickness. The sinking of the $\sigma_\theta = 27.74\,\mathrm{kg\,m^{-3}}$ isopycnal is a consequence of the reduced deep ventilation and the lack of associated dLSW formation. Due to this fact the dLSW mode waters lost its connection to the surface and the ability to renew itself with cold and fresh surface waters.

6.5 Relationship of dLSW with the surface temperature, net heat flux, Ekman velocity and thermal/haline surface density flux

To analyse the relationship of the dLSW index with different atmospheric fields like atmospheric surface temperature, net heat flux to the ocean, sea level pressure and surface density flux and to analyse the responsible forcing processes that can cause the fluctuation in the activity of the Labrador Sea mode water formation we apply a Composite Map Analysis (CMA) [*von Storch and Zwiers*, 2003] between the detrended dLSW time series (Fig. 6.7) and the aforementioned atmospheric forcing fields for bo-

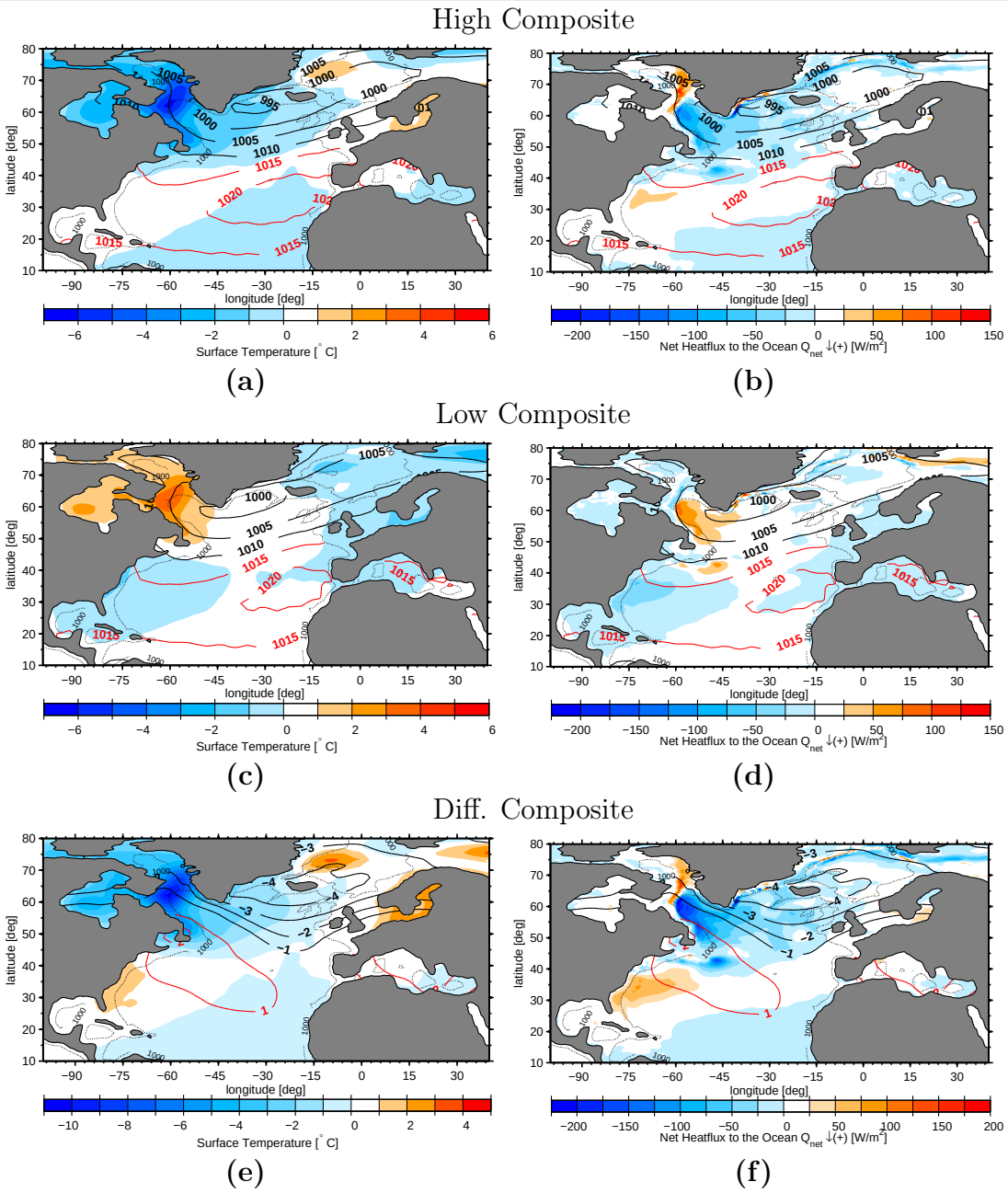

Fig. 6.8: *Composite maps of the winter (DJF) seasonal atmospheric surface temperature (left column) and net heat flux to the ocean (right column, downward heat flux positive) with the winter dLSW index. (a)-(b): high composite maps, (c)-(d): low composite maps and (e)-(f): difference between high and low composite maps. Contour lines show the composite maps of SLP (units SLP: hPa). Black and red contour lines mark the low and high pressure systems, respectively. The* 1000 *m bathymetry is indicated by a dotted contour line.*

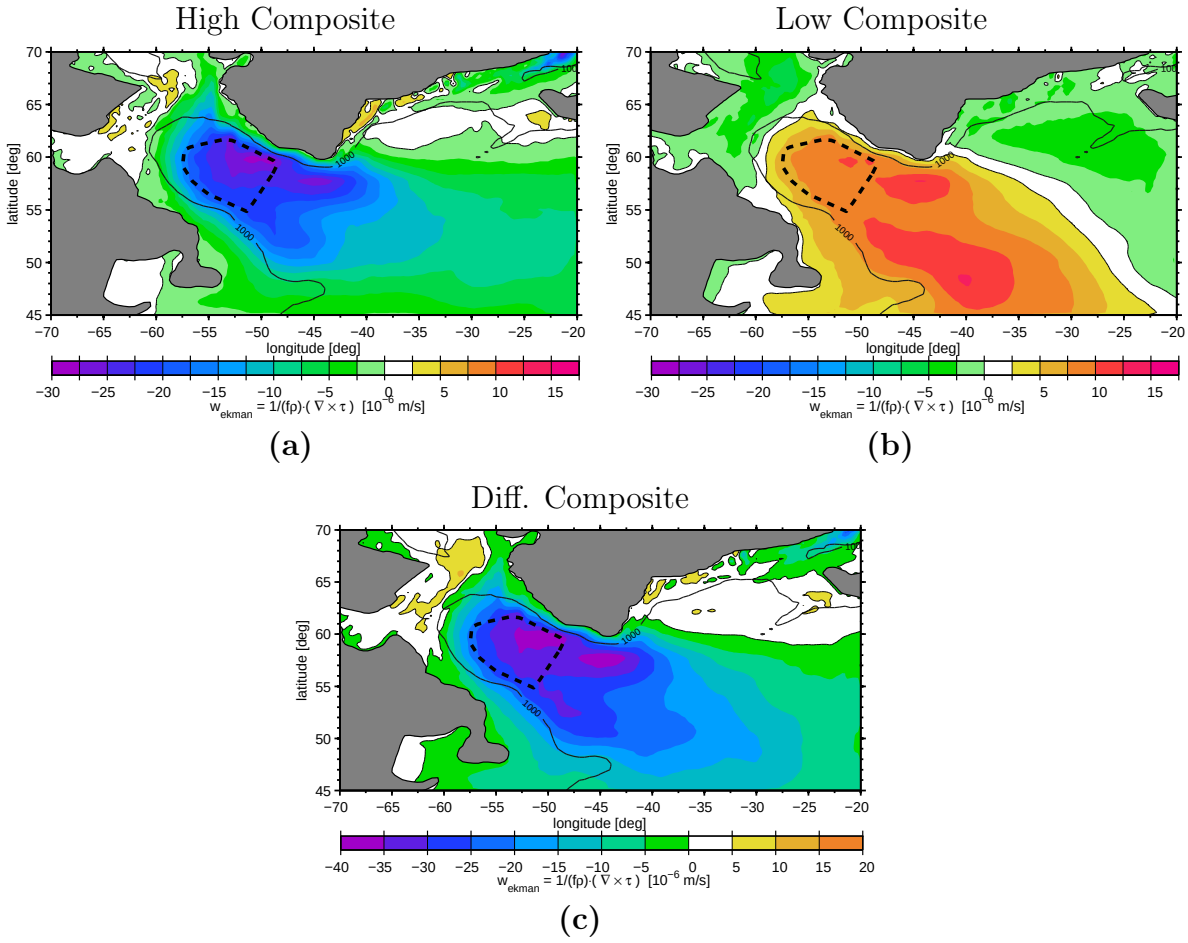

Fig. 6.9: *High (a), low (b) and difference (c) composite maps of the winter (DJF) seasonal Ekman surface velocity with the winter dLSW index. Positive and negative values in the Ekman velocity refer to upwelling (Ekman suction) and downwelling (Ekman pumping), respectively. The dashed contour line marks the area of the LSW index definition. The* 1000 *m bathymetry is indicated by a solid contour line.*

real winter (DJF). We choose for the CMA only years when the dLSW time series was higher than +0.75 standard deviation (High) and lower than −0.75 standard deviation (Low), respectively. This threshold was chosen as a compromise between the strength of the oceanic signal and the number of maps that are necessary to have an appropriate representation of the mean field. The analysis revealed that the results are less influenced by the exact threshold values in our CMA (not shown). First, we determine the

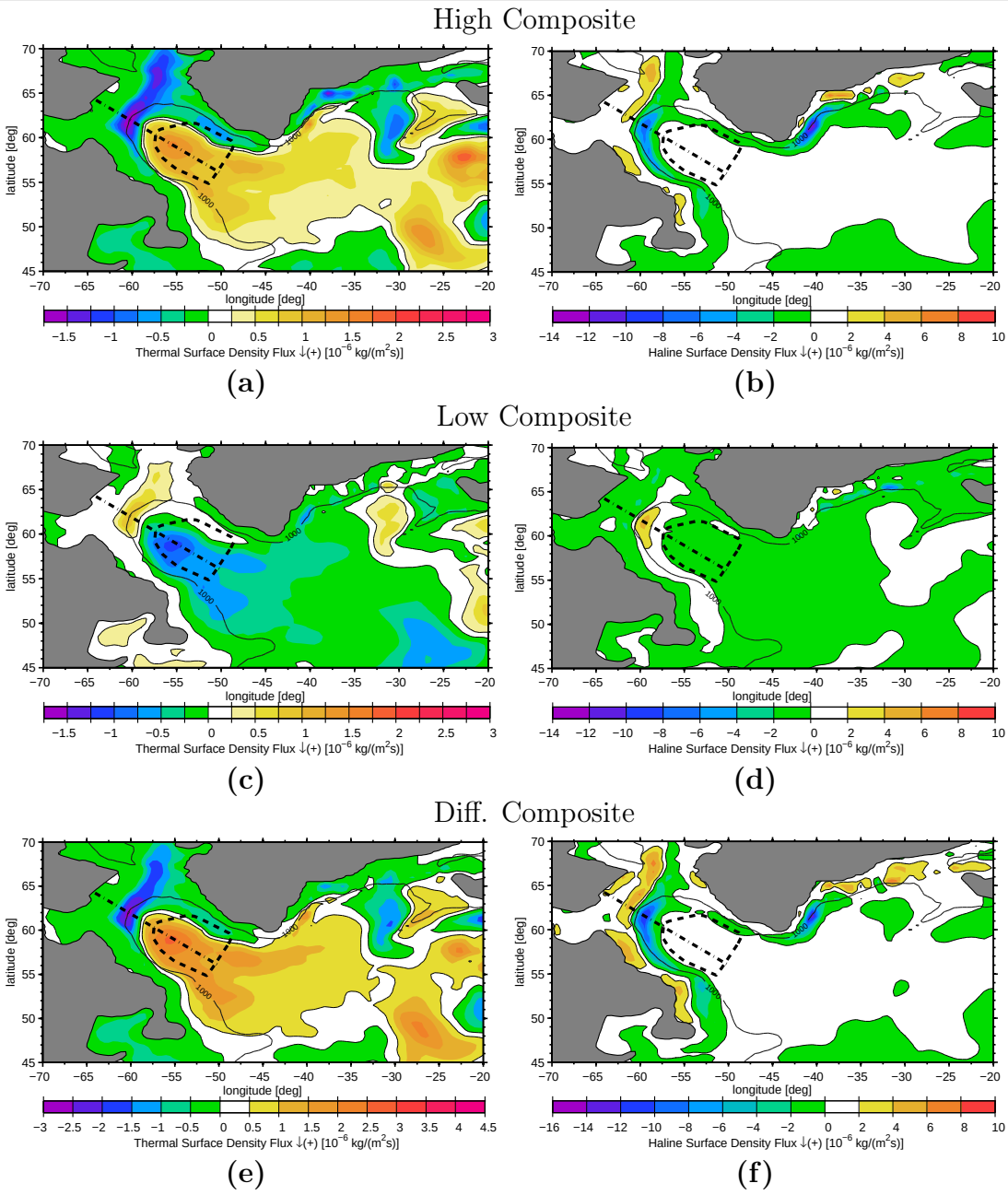

Fig. 6.10: *Composite maps of the winter (DJF) seasonal thermal (left column) and haline (right column) surface density flux (downward density flux positive) with the winter dLSW index. (a)-(b): high composite maps, (c)-(d): low composite maps, and (e)-(f): difference between high and low composite maps (units are* $10^{-6}\ kg/(m^2 s)$*). The dashed and dashed-dotted lines mark the area of the LSW index definition and the cross-section used in Fig. 6.11b, respectively. The* 1000 *m bathymetry is indicated by a solid contour line.*

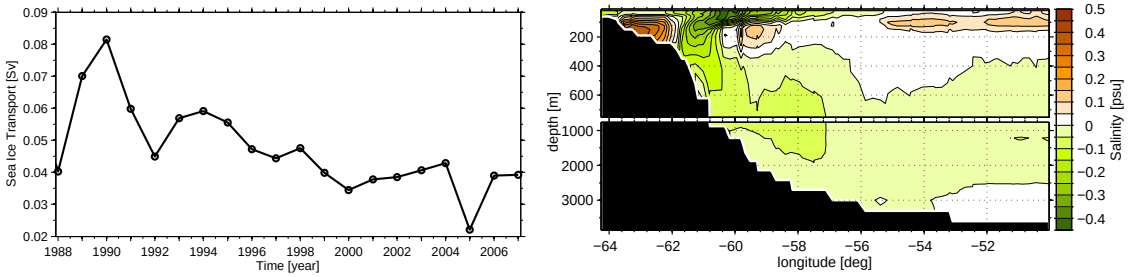

Fig. 6.11: *(a): Time evolution of winter (DJF) seasonal sea ice transport through Davis Strait for the period from* 1988-2007. *(b): difference composite map of the winter (DJF) salinity of a northwest to southeast vertical cross section through the Labrador Sea (Fig. 6.10) with the winter seasonal dLSW index.*

response time of the ocean in the Labrador Sea to changes in the atmospheric forcing. A winter lag-correlation analysis between the dLSW and the atmospheric NAO index (Fig. 6.4) covering the period from 1958-2007 shows a maximum correlation of 0.5, with a significance of 99.979%, when NAO leads dLSW variability by one year. The 0.75 above/below standard deviation composite maps between the winter dLSW index and the winter atmospheric surface temperature and net heat flux to the ocean are shown in Fig. 6.8. For the calculation of the composite maps, a lag of -1 year between the oceanic index and the atmospheric field is considered (atmosphere leads). The left column of Fig. 6.8 shows the high (Fig. 6.8a), low (Fig. 6.8c) and difference (Fig. 6.8e, high minus low) composite maps of atmospheric surface temperature with respect to the dLSW index. In years with a high dLSW index the mean surface temperature shows a strong negative anomaly of -3 °C to -6 °C in the northwestern Labrador Sea and a weak positive anomaly of 1 °C northeast of Iceland. During low dLSW years, the pattern is reversed: positive temperature anomalies are found in the Labrador Sea and negative anomalies northeast of Iceland. The difference composite map shows, in summary, that the atmospheric surface temperature in the northwest Labrador Sea cools down by up to 10 °C between a low and a high dLSW formation event. Additionally, a warming of 4 °C occurs northeast of Iceland. The right column of Fig. 6.8 displays the composite maps of the net heat flux to the ocean (downward heat flux positive). The heat flux shows a strong negative anomaly of -120 W m^{-2} over the central Labrador Sea during

events with a high dLSW formation rates. The positive anomaly that extends southwards from the northwest coast of Greenland is caused by an increased sea-ice transport through Davis Strait (57.7°W, 66.9°N, Fig. 6.11a). During low dLSW, the Labrador Sea shows a positive net heat flux of 60 $\mathrm{W\,m^{-2}}$. The net heat flux reveals a strong negative anomaly of -200 $\mathrm{W\,m^{-2}}$ over the Labrador Sea between high and low dLSW formation events (Fig. 6.8f). This strong negative anomaly triggers a further cooling of the sea surface temperature and the formation of denser water masses. Additionally, we find that the net heat flux is mainly reflecting the changes in the sensible heat flux, while the latent heat flux is only in the order of 20% of the sensible heat flux (not shown).

The contour lines in Fig. 6.8 show furthermore the high, low and difference composite maps between the dLSW index and the sea level pressure (SLP). In the high and low composite maps (Fig. 6.8 (a)-(d)), the Azores High and Icelandic Low pressure systems are indicated by red and black contour lines, respectively. The difference composite maps of the SLP show a clear dipole structure with a negative center of -4 hPa close to Iceland and a less expressed positive center of 1 hPa over the central North Atlantic. This dipole-like structure resembles to a large degree the fingerprint of the NAO [*Hurrell*, 1995]. During increased dLSW formation (Fig. 6.8a, high composite map) the Icelandic Low is deepened. Due to the increased pressure gradient between the Azores High and the Icelandic Low, the northwesterly winds are intensified and they bring very strong and cold winds from North Canada and the Canadian Archipelago to the Labrador Sea. These winds lead to a strong cooling of the surface and increase the net heat loss of the ocean, which can be seen in the high composite maps of the surface temperature and the net heat flux (Fig. 6.8a, 6.8b).

To further distinguish the influence of the surface winds in the Labrador Sea, we applied in Fig. 6.9 a CMA between the winter dLSW index and the winter surface Ekman velocity w_{ekman}. The Ekman velocity w_{ekman} is calculated as:

$$w_{ekman} = \frac{1}{\rho \cdot f} \cdot \nabla \times \overrightarrow{\tau}, \tag{6.1}$$

where f and ρ is the Coriolis parameter and surface density, respectively. During high dLSW the Ekman velocity in Fig. 6.9a features mainly negative values in the

entire northwest Atlantic Ocean with a maximum negative value of $-30 \cdot 10^{-6}$ m/s in the northeastern part of the central Labrador Sea. This negative Ekman velocity is associated to a downwelling process due to wind stress curl induced Ekman pumping. Local coastal upwelling regions (positive Ekman velocity) are featured at the east coast of Greenland, southwest of Iceland and in Davis Strait. During low dLSW formation the composite map of the Ekman velocity (Fig. 6.9b) reveals a positive anomaly of $15 \cdot 10^{-6}$ m/s in the central and southern Labrador Sea as well as a negative anomaly of $-5 \cdot 10^{-6}$ m/s in the northern Labrador Sea and southern Irminger Sea.
To analyse the influence of the buoyancy forcing, we applied a CMA to the surface density flux to the ocean (calculation follows *Josey* [2003]). We distinguish here between the thermal and haline related contributions to the surface buoyancy forcing in the Labrador Sea. Fig. 6.10 shows the composite map between the winter dLSW index and the winter thermal (left column) and haline (right column) surface density flux. The thermal surface density flux takes into account the contributions of sensible, latent and radiative heat fluxes, respectively. The haline surface density flux includes the contributions of precipitation, snow, evaporation and sea-ice formation. The left column of Fig. 6.10 shows the high (Fig. 6.10a), low (Fig. 6.10c) and difference (Fig. 6.10e) composite maps of the dLSW index and the thermal surface density flux. Positive values indicate an increase in the surface density of the ocean. During years with a high dLSW formation activity, the thermal contribution of the surface density flux is positive in the central Labrador Sea and Irminger Sea as well as southwest of Iceland with a maximum value of $2 \cdot 10^{-6}\,\mathrm{kg/(m^2 s)}$ in the central Labrador Sea. The gain of surface density is mainly related to an increased heat loss by sensible heat during years with high dLSW formation. The coastal areas of the Labrador and Irminger Sea show however a negative thermal surface density flux. Here, the major influence is given by the coverage of the sea ice which largely reduces the heat exchange between ocean and atmosphere. The negative thermal density flux in the northwestern Labrador Sea is related to a massive sea ice export through Davis Strait (57.7°W, 66.9°N, Fig. 6.11a). In years with a low dLSW formation activity the central Labrador Sea shows a negative thermal surface density flux which is again mainly related to an increased sensible heat flux during that phase. The coastal areas of the Labrador Sea show a slightly positive thermal density flux which indicates a reduced sea ice coverage.

The haline surface density flux (Fig. 6.10, right column) is dominated by the formation and melting of sea ice. The contributions of precipitation, snow and evaporation are smaller by a factor of 10 (not shown). During years with high dLSW, the high composite map of the haline surface density flux (Fig. 6.10b) features a decrease in the surface density in the area of the LSBC, as well as with an extreme value of $-12 \cdot 10^{-6}\,\mathrm{kg/(m^2 s)}$ in the Irminger Sea. This high decrease in the surface density is related to an intensified transport and subsequent melting of sea ice through Davis Strait. The high formation rate of sea ice can be seen in positive surface density fluxes of $\sim 6 \cdot 10^{-6}\,\mathrm{kg/(m^2 s)}$ at the shelf areas and the associated extraction of freshwater. This is proven by the time evolution of the sea ice transport through a Davis Strait cross section at 61.7°W, 66.6°N - 53.7°W, 67.2°N (Fig. 6.11a). Due to intense westerly winds, during the high dLSW phase, sea ice is transported towards the position of the LSBC. The melting of sea ice releases large quantities of freshwater at the surface and causes a high negative haline surface density flux. One can ask why this high negative haline surface density flux from the sea ice melting has a minor influence on the central Labrador Sea. Fig. 6.11b shows the difference composite map of the winter salinity of a northwest to southeast vertical cross section through the Labrador Sea with the winter dLSW index. This section has a positive surface salinity anomaly of ~ 0.25 psu on the shelf at around 62°W which is caused by intensified sea-ice formation during high dLSW phases. The negative salinity anomaly of ~ -0.4 psu at around 60°W is related to the melting of sea ice and the release of fresh water. It is also detected that on this cross-section the negative anomaly is mostly confined to the position of the LSBC. We observe only a minor interaction between the LSBC and the central Labrador Sea caused by horizontal mixing (see Fig. 6.3). In years with a low dLSW formation (Fig. 6.10d) the whole central Labrador Sea shows a slightly negative surface density flux which is mostly related to precipitation (not shown). Only the western part of the LSBC and the eastern coast of Greenland feature positive values in the low composite map of the haline surface density flux. This is again related to an increased sea ice formation.

6.6 Discussion of the modelled Labrador Sea Water variability

In this study we have investigated the deep-water formation in the Labrador Sea using a FESOM model setup that has an increased but non-eddy-resolving resolution in the deep water formation areas of the North Atlantic Ocean. The layer thicknesses of dLSW and uLSW, which are formed during the winter and spring deep convection, were analyzed for the period 1988-2007. It is shown that the model is able to reproduce the well known temporal evolutions of the potential density, temperature and salinity since the late 1980s as shown by *Yashayaev* [2007]; *Yashayaev and Loder* [2009]. The temporal evolution features two different phases of LSW formation which differ significantly from each other. The first phase (1988-1995) is characterized in the model by a rapid increase in the production of spring dLSW mode water in the first two years of the period. After that, the Labrador Sea remained in a stable cold and fresh deep convection phase with a maximum convection depth of > 2000 m. The time evolution of the temperature shows a similar abrupt drop of ~ 0.7 °C, which is associated to a sudden onset of deep convection and downward ventilation of cold surface waters. This trend in the ocean temperature of the Labrador Sea of the 1990s is also documented by observational studies [*Curry et al.*, 1998], which refer this strong trend to an exceptional high positive NAO. In contrast, the time evolution of the salinity shows a more gradually decrease of ~ 0.04 psu. Analysis of a Davis Strait cross section (Fig. 6.11a) revealed that the period from 1989-1995 is characterized in the model by an increased sea ice export from Baffin Bay. Sea ice is transported by surface winds to the position of LSBC and leads there to a high fresh water input caused by sea ice melting (Fig. 6.10). So, the slow decrease in salinity seems to originate from a horizontal mixing process with a fresh LSBC. Further, we can observe a freshening trend between 1988-1996 in a depth below 2000 m. This freshening trend has its origin already in the late 1960s (not shown). From 1969 until 1996, the salinity decreased gradually by 0.04 psu. This value is comparable to other model results (*Wu et al.* [2004]). Observational studies [e.g., *Dickson et al.*, 2002; *Curry et al.*, 2003] confirm a similar decrease in the salinity evolution since 1960s in the deep Labrador Sea and the entire deep North Atlantic Ocean. They account this salinity decrease to a continuously freshening of the overflow

water masses due to an intensified freshwater input from sea ice melting. Analysis of different cross sections within our model (e.g. Denmark Strait, Iceland Scotland Ridge) (not shown) support this theory.

The second phase (1996-2007), dominated by an increased production of the uLSW is initiated by the isolation of dLSW mode water from the supply of cold and fresh surface waters. This goes along with a drop in the NAO-index at the beginning of 1995-1997 (Fig. 6.4). The downward ventilation of the surface water and the renewal of dLSW mode water in the winter time convection ceased. The previously formed homogeneous dLSW body starts to slowly degenerate due to horizontal mixing with a warmer and saltier LSBC. This leads to a gradual increase in temperature and salinity which extends over the entire second phase. Also the deep ocean levels below 2500 m, which mainly originate from the overflow water masses, show a moderate increase in the salinity. This slight increase is also documented by *Yashayaev and Loder* [2009].

Yashayaev and Loder [2009] have used observations to identify a period of "dense and voluminous" LSW mode water between 1987-1994. Their mode of LSW extends into a depth of 2400 m and is equivalent to the dLSW formation event captured by our model. A second event, from 2000 to 2003, was described by *Kieke et al.* [2006] and *Yashayaev and Loder* [2009] which reached into depths of $\sim$ 1300 m. This event is the analogue to the increased formation of the uLSW mode water in our model between 1999 to 2007 (Fig. 6.3).

Major changes of the model mixed layer depth of the deep-water formation areas were observed: i) the mixed layer depth in the central Labrador Sea is reduced by $\sim$ 50% from one phase to the other and ii) the decrease in the mixed layer depth of the Irminger Sea is even more drastic ($\sim$ 80%). The main deep convection cell in the Labrador Sea in our model is shifted to the northwest. This shift might be due to a lack of eddy induced mixing with the West Greenland Current in the Labrador Sea caused by the limited horizontal resolution as described by *Chanut et al.* [2008]. They argued that the existence of eddies that mix with the warm Irminger Current, the so-called Irminger Rings, can limit the northward extend of the main deep convection area.

The results for the layer thickness of the LSW mode waters (Fig. 6.4) are also in good agreement with observations [*Curry et al.*, 1998; *Kieke et al.*, 2006, 2007; *Yashayaev*, 2007; *Yashayaev et al.*, 2007a; *Rhein et al.*, 2011]. The offset in the transition rate from

the low uLSW formation to the high uLSW formation between model and observations might give a hint regarding a missing feedback mechanism from the ocean surface to the atmosphere within the model that could be related to the relatively sparse resolution of the atmospheric reanalysis forcing data. Our simulated dLSW data reveal further that the system that was "charged with dense water" in the period from 1990-1995, does afterwards not react instantaneous to a change in the NAO index. Based on observational data *Curry et al.* [1998] suggest a general time lag of $2-4$ years between the NAO index and dLSW index. Our model results indicate a smaller time lag of not more than $1-2$ years. If the system is once "charged with dense water" and a massive dLSW body with a corresponding strong density stratification is built up, like in the period from 1990-1995, then also a lower surface buoyancy forcing can be sufficient enough to further produce dLSW as mentioned by *Lazier et al.* [2002]. In this case the system acts as a filter to short time fluctuations in the atmospheric forcing until the dLSW body further degenerates due to reduced surface buoyancy flux and mixing with the LSBC. Different authors [e.g., *Marshall and Schott*, 1999; *Lazier et al.*, 2002; *Pickart et al.*, 2002, 2003] assume that there is a set of conditions that have to be fulfilled in order to favor deep convection in the ocean: a weakly stratified water mass, a closed cyclonic circulation to trap the water masses and to prevent the surface waters from being advected, and the most important condition is a strong atmospheric winter time buoyancy forcing [*Pickart et al.*, 2003]. To verify the atmospheric forcing condition within our model we have applied a CMA between the dLSW index and the SLP field. We could clearly identify in the model that a pattern in the SLP field which has a low pressure center over Iceland is one of the main triggers for the variability in the model LSW formation. *Dickson et al.* [1996] already assumed that the variability in the Labrador Sea Water formation, on longer time scales, is mainly influenced by the atmospheric forcing. Based on CMA it is shown that a high dLSW index (Fig. 6.7) in our model setup is associated with a SLP pattern which resembles the positive phase of NAO: a deepened Icelandic Low and a strong Azores High. Associated to this SLP dipole-like structure is the advection of dry and cold polar air from the Canadian landmass over the relatively warm Labrador Sea, which induces an enhanced heat loss, leading to the formation of dense surface water masses and increased deep convection as described by a variety of authors [e.g., *Dickson et al.*, 1996; *Pickart et al.*, 2003].

The heat loss induced deep water formation is not the only mechanism which favours the production of dLSW. Additionally, we show on the basis of a CMA of the Ekman velocity that during high dLSW and positive NAO conditions the deep-water formation in the central Labrador Sea further benefits from surface wind induced Ekman pumping. There, an Ekman convergence is caused on the surface by an adequate surface wind stress, which leads to an improved downstream of the cold surface water masses. This further amplifies the mixing within the Ekman layer which promotes the breakup of the surface stratification to favor the ventilation of deep ocean layers.
Further, we show with the analyse of the surface density flux that our index definition area which is marked by the dashed lines in Fig. 6.10, is mostly dominated by the thermal contribution of the surface density flux, where the sensible heat flux is the main contributor. In our simulation, the haline contributions, especially in the high dLSW phase, are determined largely by regional contribution of sea ice melting. This is in contradiction to the explanations of *Dickson et al.* [1988], who suggested that the Labrador Sea is strongly influenced by propagating negative salinity anomalies induced by melting of sea-ice from the Arctic Ocean. We showed that within our model setup the central Labrador Sea is mostly shielded from the haline contributions of the surface density flux by the LSBC. We detect only a minor interaction between the central Labrador Sea and the LSBC by lateral mixing. The lack of lateral mixing with the LSBC could be caused by an absence of eddy induced mixing with the west Greenland Current as mentioned by *Katsman et al.* [2004], due to an insufficient eddy resolving resolution in the model Labrador Sea. *Katsman et al.* [2004] described in an idealized regional model study that the existence of eddies, especially the so called Irminger Rings are crucial for the lateral mixing and restratification process in the central Labrador Sea.

6.7 Conclusions of the modelled LSW variability and analysis

We demonstrate that the FESOM approach in conjunction with the here used model setup can be a suitable tool to simulate the spatio-temporal evolution of the layer thicknesses of the LSW mode waters. The model is suitable to simulate the evolution

of LSW indices that is in agreement with observed time series of *Curry et al.* [1998]; *Kieke et al.* [2006, 2007] and *Rhein et al.* [2011]. Based on these indices we show that the Labrador Sea, in our global model setup can act as a low-pass filter to fluctuations in the NAO index, so that only persistent NAO events correlate with the dLSW index. Our global model setup also confirms a dominance of the atmospheric circulation as one of the main triggers for the variability in the dLSW and uLSW index, which affects the deep water formation by increased heat loss and by intensified mixing of the Ekman layer. Our analysis of the thermal and haline surface density flux indicate that the central Labrador Sea is dominated by the thermal contributions of the surface density flux, while the haline contributions, that are dominated by the effects of sea ice melting, are limited in our model setup to the area of the LSBC.

AWI Alfred-Wegener-Institut für Polar- und Meeresforschung in der Helmholtz-Gemeinschaft

7

Interannual to Decadal variability in the North Atlantic Ocean

There is a growing effort in describing and understanding the climate variability in the North Atlantic sector [*Curry and McCartney*, 2001]. This region is strongly influenced by the strength and pathway of the westerly wind system, which forms due to the gradient between the Azores and Icelandic pressure centers under geostrophic adjustment [*Gill*, 1982; *Curry and McCartney*, 2001]. The intensity of the westerlies can be described in terms of the North Atlantic Oscillation (NAO), which is defined as the normalized pressure gradient between the Azores High and the Icelandic Low [*Hurrell*, 1995]. These winds determine to a large degree the subpolar and subtropical gyres [*Böning et al.*, 2006]. Around these anticyclonic and cyclonic pressure centers major recirculation regimes in the ocean develop due to frictional forces in form of the subpolar and subtropical gyre. Both gyre systems contain important branches of the global thermohaline circulation (THC) [*Böning et al.*, 2006].

The system of the subpolar gyre (SPG) contains in the eastern part the northward flowing North Atlantic Current (NAC) which is essential for the supply of the northeastern Atlantic with warm and saline waters [*Böning et al.*, 2006]. The northern and western part of the gyre branch comprises strong boundary currents that extends along the continental slope like the East Greenland Current, West Greenland Current and Labrador Current. These currents carry cold and fresh waters of Arctic origin southward. The subpolar gyre is an important region for the atmosphere ocean heat exchange [*Pickart et al.*, 1997, 2002]. The resulting surface buoyancy forcing and the formation of deep water masses are crucial for the downwelling limb of the of Atlantic meridional overturning circulation (AMOC) [*Yashayaev et al.*, 2007b; *Rhein et al.*, 2011]. The subtropical gyre (STG) system is dominated on the western side by the Gulf Stream current, which

transports major amounts of heat and salt of subtropical origin northward.
A certain amount of variability in the strength of the STG and in particular of the SPG has been associated to the NAO [*Brauch and Gerdes*, 2005; *Böning et al.*, 2006; *Lohmann et al.*, 2009]. *Curry and McCartney* [2001] introduced a baroclinic mass transport index from hydrographic observations that describes the baroclinic pressure difference between the centers of the STG and SPG. The time evolution of this index suggest a certain decadal variability of the North Atlantic gyre circulation, with a weakening gyre circulation until the late 1960s, followed by a strengthening in the subsequent decades [*Curry and McCartney*, 2001].
The determination of important modes of climate variability especially on interannual to decadal and longer time-scales is a topic of ongoing relevance. These modes are crucial for the deeper understanding of the climate system on human time-scales as well as for the extrapolation of future climate evolutions. Different modes of climate variability have been identified in observational data by stochastic climate modeling [*Dima and Lohmann*, 2004]. There are a variety of publications [e.g., *Deser and Blackmon*, 1993; *Mann and Park*, 1994; *Dima and Lohmann*, 2004] that identified a quasi-decadal mode of 12-15 years which describes a considerable amount of the surface temperature variability in the North Atlantic sector. Further climate modes on decadal time-scales that are related to the accumulation of salinity anomalies have been identified in general ocean circulation models (OGCM) by *Weisse et al.* [1994]. An approved method for the identification of stable climate modes, base upon the stochastic climate model of principal oscillation pattern (POP) analysis as introduced by *Hasselmann* [1988] and further discussed in detail by *von Storch et al.* [1995].
In this chapter we use the global FESOM setup introduced in section 2.2 under realistic sea surface forcing (see section 2.3). In order to analyse the variability of the North Atlantic gyre circulation as well as the response time to the NAO. This model run will be referred as normal COREv2/SODA run. To be able to assign the underlying variability to the atmospheric forcing or to internal modes of the ocean we employ another model run under random forcing condition which will be referred in this chapter as random COREv2/SODA run (see section 2.4).
To determine and visualize the important oscillatory modes in the North Atlantic Ocean we apply a Principal Oscillation Pattern (POP) analysis (see chapter 3) to a 3D tem-

perature field which takes into account the entire simulation period from 1958-2004. This gives us the opportunity to isolate horizontally but also vertically propagating patterns of important oscillatory modes in the full 3D structure of the North Atlantic Ocean.

7.1 Variability of North Atlantic Deep Water formation

In this section we analyse the variability in the deep-water mass formation in terms of the North Atlantic Deep Water (NADW) index of the last spinup cycle for the the normal (Fig. 7.1a) and random (Fig. 7.1b) forced COREv2/SODA run. The NADW index is defined via the meridional velocity $v(x, y, z, t)$ and the corresponding meridional transport $V(x, y, z, t)$:

$$V(x, y, z, t) = [v(x, y, z, t)\Delta x]$$

The NADW index is then calculated as the maximum value of the local surface to bottom integrated meridional transport:

$$\text{NADW}(t) := \max \left[\int_{top}^{z} V(x, y, z', t)\, dz' \right]$$

The maximum value is extracted in the range of: $x \in [80^{\circ}\text{W}, 60^{\circ}\text{W}]$, $y \in [20^{\circ}\text{N}, 40^{\circ}\text{N}]$ and $z > 500$ m. With the later condition, we to exclude the meridional surface transport.

Fig. 7.1a shows the time evolution of the monthly NADW index (orange) and the 3 year-running-mean filtered index (red) of the normal forced COREv2/SODA run. The monthly index features a distinct seasonal cycle that varies between ~ 8 Sv to ~ 13 Sv with an underlying pronounced decadal variability. It has a maximum variance of ~ 1.5 Sv with a decreasing amplitude towards the end of the simulation period. The time evolution of the filtered index has maxima around 1964, 1976, 1991 and 1998, respectively. To analyse the NADW index underlying variability, we apply a Fast Fourier Transformation (FFT) (Fig. 7.1c), which transfers the time into the frequency domain. We applied a standard FFT (black) as well as a Welch-Method FFT (window FFT)

(red) algorithm to be able to better highlight the most important periodicities. The Welch-Method FFT was carried out with 3 FFT windows and a window overlap of 50%. The highest peak in the standard FFT and Welch spectrum is the obvious seasonal cycle, followed by a decadal periodicity of 14.2 years. The standard FFT spectra has further periodicities at 7.8, 4.7, 2.6 and 0.5 years. Also the 7.8 year periodicity is conceal in the Welch-Method spectra due to the dominance of a 14.2 year peak.
To determine if these periodicities are caused by the atmospheric forcing or originate from internal modes of the ocean, we applied the same analysis to the random forced COREv2/SODA run. For this run the forcing has a white noise character which has no distinct frequencies. In Fig. 7.1b, the time evolution of the monthly NADW index (orange) and the 3 year-running-mean filtered index (red) of the random forced COREv2/SODA run are displayed. The amplitude in the variation of the seasonal cycle and in the decadal variability are comparable with the results from the normal COREv2/SODA forced run. But in the decadal time evolution of the 3 year-running-mean filtered NADW index an obviously shorter periodicity with a slightly increasing amplitude is dominating for the first half of the simulation period until 1982. The time evolution of the filtered random forced NADW index features maxima around 1962, 1969, 1972 and 1986 as well as a trend to an increasing NADW index after 1992. The FFT and Welch-Method spectra of the random forced NADW index (Fig. 7.1d) features again as the highest peak the annual cycle followed by the peak of the interannual variability of 7.1-8.3 years. The standard FFT spectra shows further minor periodicities at 14.2, 3.9 and 0.5 years.
To further analyse the significance of the most important decadal to interannual periodicities of 14.2 and 7.1 years in the FFT and Welch-Method spectrum of the normal (Fig. 7.1c) and random (Fig. 7.1d) forced COREv2/SODA run we applied a singular spectrum analysis (SSA) to the corresponding NADW indices. Fig. 7.2 shows the original (black) and reconstructed (red) time series of the normal and random forced NADW index.
The reconstruction of the normal forced NADW time series in Fig. 7.2a consist of three modes each with a period between 12-15 years. They account together for 28.67% of the explained variance. The decreasing amplitude in the variability of the reconstructed time evolution of the normal forced NADW index, indicates that this periodicity losses

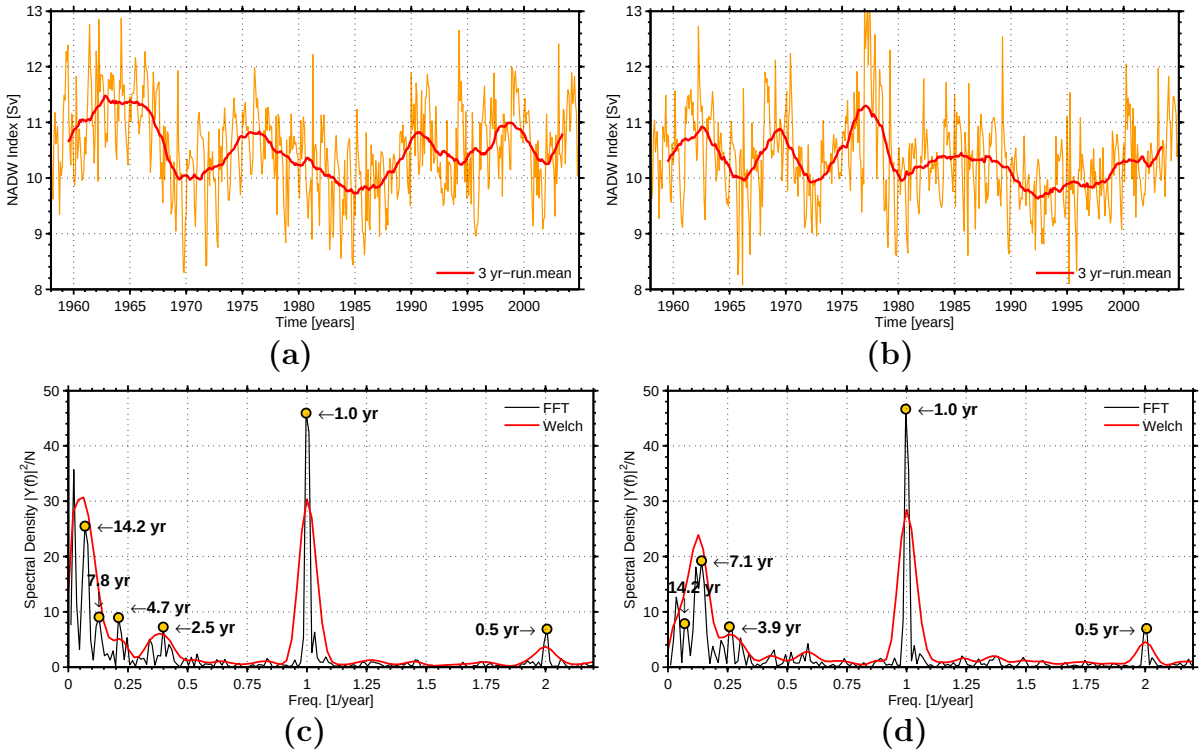

Fig. 7.1: *(a)-(b):Time evolution of monthly (orange) and 3 year-running-mean filtered (red) normal (a) and random (b) forced NADW index.*
(c)-(d): Normal Fast Fourier Transformed (FFT, black) and Welch-FFT (red) frequency spectra of the normal (c) and random (d) forced NADW index. The spectra of the normal and random forced NADW index shows besides the 1 year periodicity a strong decadal and interannual variability of 14.2 *and* 7.1 *years, respectively.*

slowly its dominance over the entire simulation period.

Fig. 7.2b shows the SSA reconstruction of the random forced NADW time series. The reconstruction consist also of three modes, with periodicities between 6-8 years. This 3 modes account together for 23.61% of the variance. The reconstructed time evolution of the random forced NADW index revealed that the 6-8 years modes features a stable variability in the first half of the simulation period from 1958-1982. After that the variability ceases strongly in the second half of the simulation period.

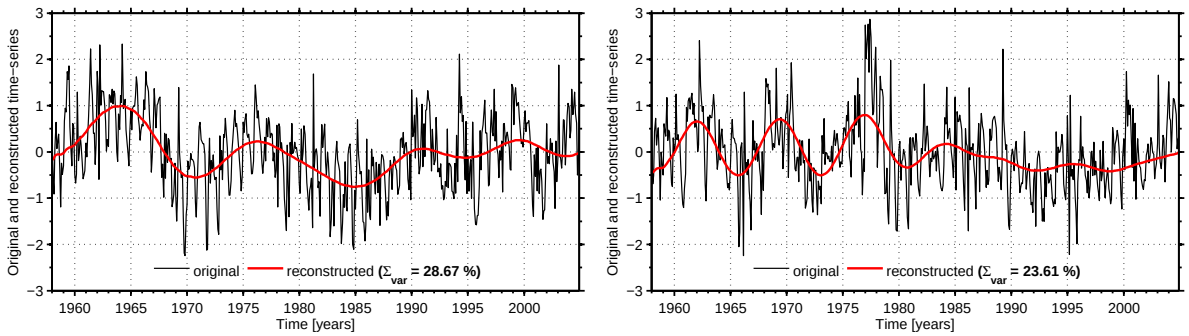

Fig. 7.2: *Singular spectrum analysis (SSA) of the normal (a) and random (b) forced NADW index. Black and red lines mark the original and reconstructed time-series. The reconstruction of the normal and random time-series consists each of three modes, for the normal run with a period of* 12-14 *years and for the random run with a period of* 6-8 *years. The reconstructions of the normal and random time series account for* 28.7% *and* 23.6% *of the variance.*

7.2 Variability of subpolar and subtropical gyre index

The anticyclonic subtropical gyre (STG) and cyclonic subpolar gyre (SPG) include large recirculation regimes in the North Atlantic that contains strong boundary currents and represents an important part of the global ocean circulation [*Häkkinen and Rhines*, 2004; *Hatun et al.*, 2005; *Böning et al.*, 2006]. The region of the SPG is characterized by a strong heat exchange between the ocean and the atmosphere that results in a deep convection and vertical ventilation of water masses [*Rhein et al.*, 2002, 2011; *Pickart et al.*, 2002; *Yashayaev et al.*, 2007a].

The west flank of the STG regime, that is dominated by the Gulf Stream, is the main pathway for warm and saline water into the polar branch of the North Atlantic Ocean. The strength of the SPG and STG can be defined via the horizontal barotropic streamfunction.

In the following sections all results will be related to the normal COREv2/SODA forcing run. Fig. 7.3 shows the horizontal barotropic streamfunction (HBS) in the North Atlantic Ocean and Arctic Ocean averaged for the interval 1958-2004. The HBS in the North Atlantic is characterized by two major anticyclonic (positive, reddish colors)

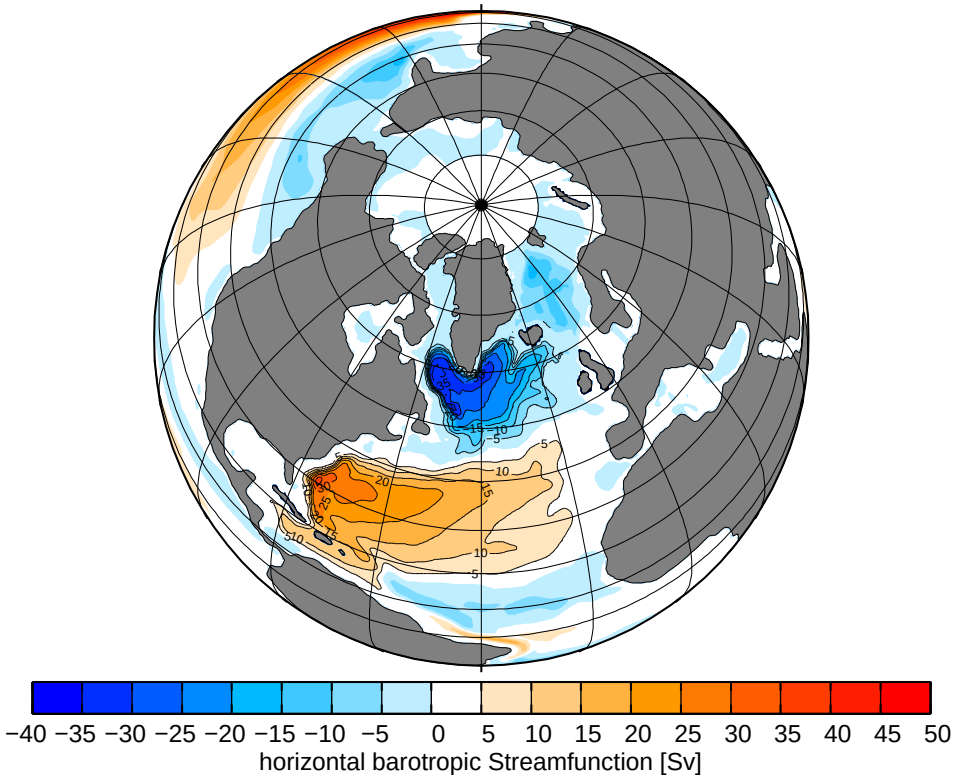

Fig. 7.3: *Mean horizontal barotropic streamfunction in the North Atlantic averaged over a period from 1958-2004. Positive values: anticyclonic circulation, negative values: cyclonic circulation. The position of the subtropical and subpolar gyre are highlighted by black contour lines. The maximum mean streamfunction of the subtropical gyre is* 45 *Sv at* 75.25° *W,* 30.5° *N, the minimum streamfunction of the subpolar gyre is* −35 *Sv at* 53.75° *W,* 56.5° *N.*

and cyclonic (negative, blueish colors) circulation regimes, which describe the branch of the STG and SPG gyre. The region of the STG extends between 14°N-48°N from the American east coast westward until 16°W and features a maximum value of 45 Sv at 75.25°W, 30.5°N. The negative cyclonic circulation cell of the SPG reaches from 45°N until 65°N and extends from the north western Labrador Sea (60°W) eastward until 12°W and reveals a magnitude of −35 Sv at 53.75°W, 56.5°N. The strength of the STG and SPG is defined as the magnitude of the monthly horizontal barotropic streamfunction of the anticyclonic circulation cell between 15°N-45°N and cyclonic cir-

culation cell between 45°N-65°N, respectively.

Fig. 7.4 shows the time evolution of the 3 year-running mean filtered SPG (blue, Fig. 7.4a) and STG (red, Fig. 7.4b) index, respectively. Furthermore, in analogy to the baroclinic mass transport (BMT) index of *Curry and McCartney* [2001], we calculated a ΔGyre index (green, Fig. 7.4c), which is defined via the difference between STG and SPG indices. The BMT and ΔGyre index serve as an estimator for the strength of the eastward baroclinic mass transport between the subpolar and subtropical gyre boundary.

The time evolution of the filtered SPG index (Fig. 7.4a, blue curve) reveals a pronounced decadal variability around a mean value of −40.9 Sv. We find four distinct maxima in the SPG index around 1965, 1977, 1985 and 1995, where the strongest subpolar gyre maxima is around 1994-1995 with a value of −47 Sv. From the early 1970s until the end of the simulation period the SPG index features a slight increase in the variability and activity of the subpolar gyre.

The red curve in Fig. 7.4b shows the filtered time evolution of the STG index with a mean value of 37.6 Sv. Also here we find a pronounced decadal variability with four maxima around 1963, 1976, 1990 and 1999, where the strongest event in the activity of the subtropical gyre is in 1993 with a value of 41 Sv. Furthermore, we observe a slight decreasing trend in the strength of the subtropical gyre from the beginning of the simulation period until 1995. After 1995 the strength of the subtropical gyre is slightly increasing until the end of the simulation period.

The ΔGyre index (Fig. 7.4c, green curve), which includes the variability of the subpolar and subtropical gyre index, features a mean value of 78.5 Sv. The first half of the simulation period indicates a slight decreasing trend in the ΔGyre index, while the second half shows an increasing trend which is caused by the increasing subpolar gyre strength in that time interval. The ΔGyre index features as well as the subpolar and subtropical gyre four distinct maxima, where the maxima of 1963 and 1995 are the strongest events with 84 Sv and 83 Sv, respectively.

To further analyse the response time of the gyre indices relative to the atmospheric forcing we calculated the lag-correlation analysis between the gyre indices and the North Atlantic Oscillation (NAO) index. The NAO index is an estimator for the variability of the westerly winds of the atmospheric forcing and is defined as the normalized pressure

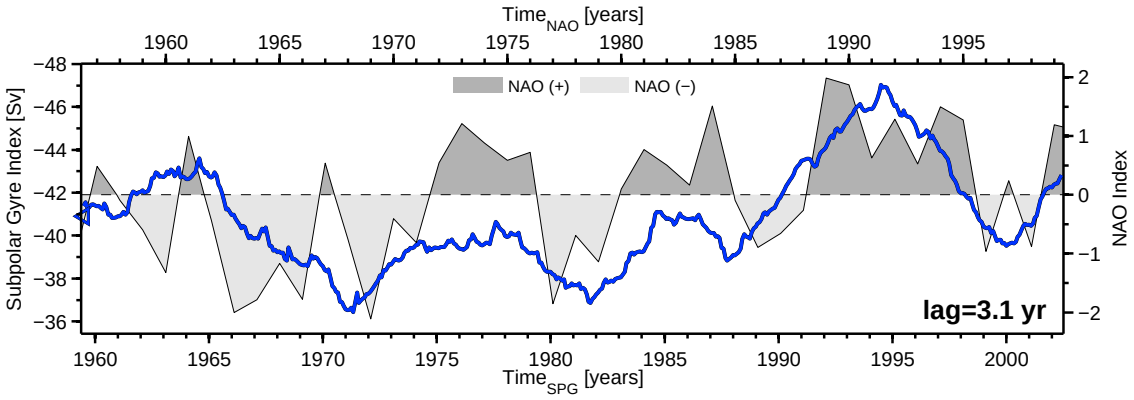

(a)

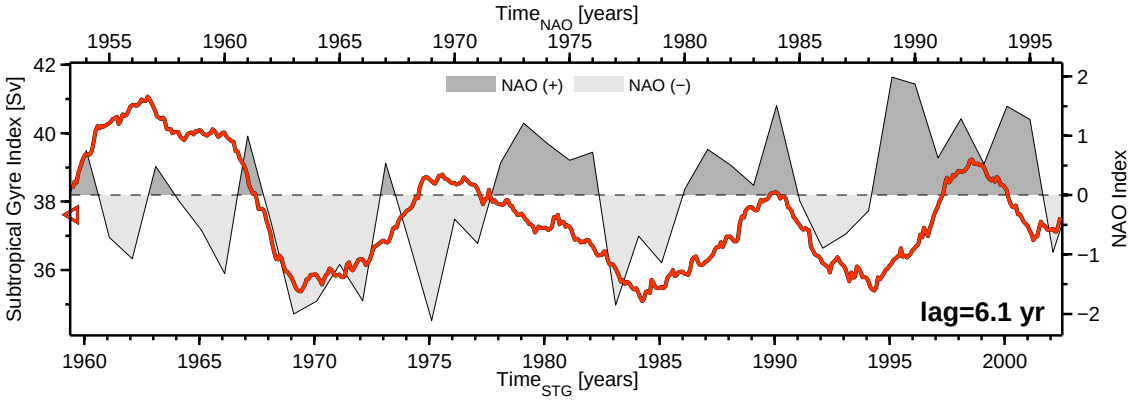

(b)

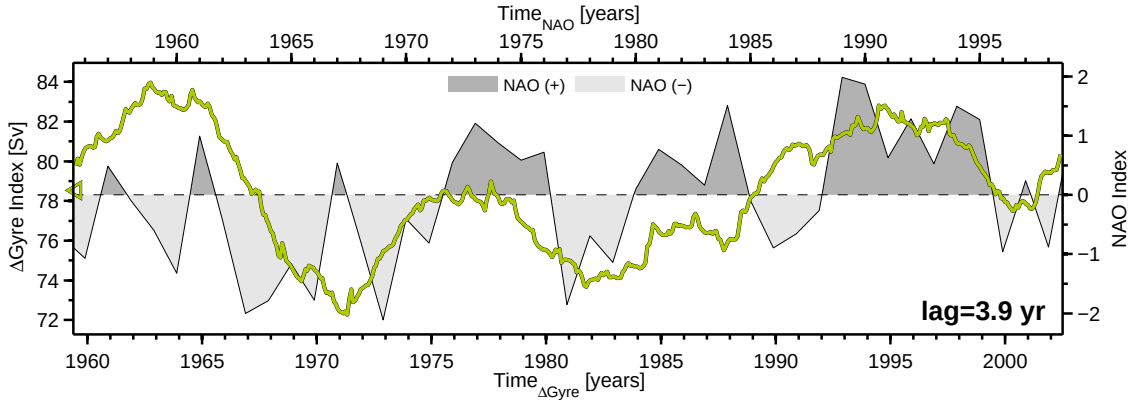

(c)

Fig. 7.4: *Time evolution of the 3 year-running-men filtered subpolar gyre (SPG) index (a), subtropical gyre (STG) index (b) and ΔGyre index (c) (subtropical minus subpolar gyre index). Triangles indicate the mean values of the gyre indices. The lag shifted time evolution of the winter (DJF) NAO index is superimposed, where the positive and negative phase of the NAO is indicated as dark and light grey areas, respectively.*

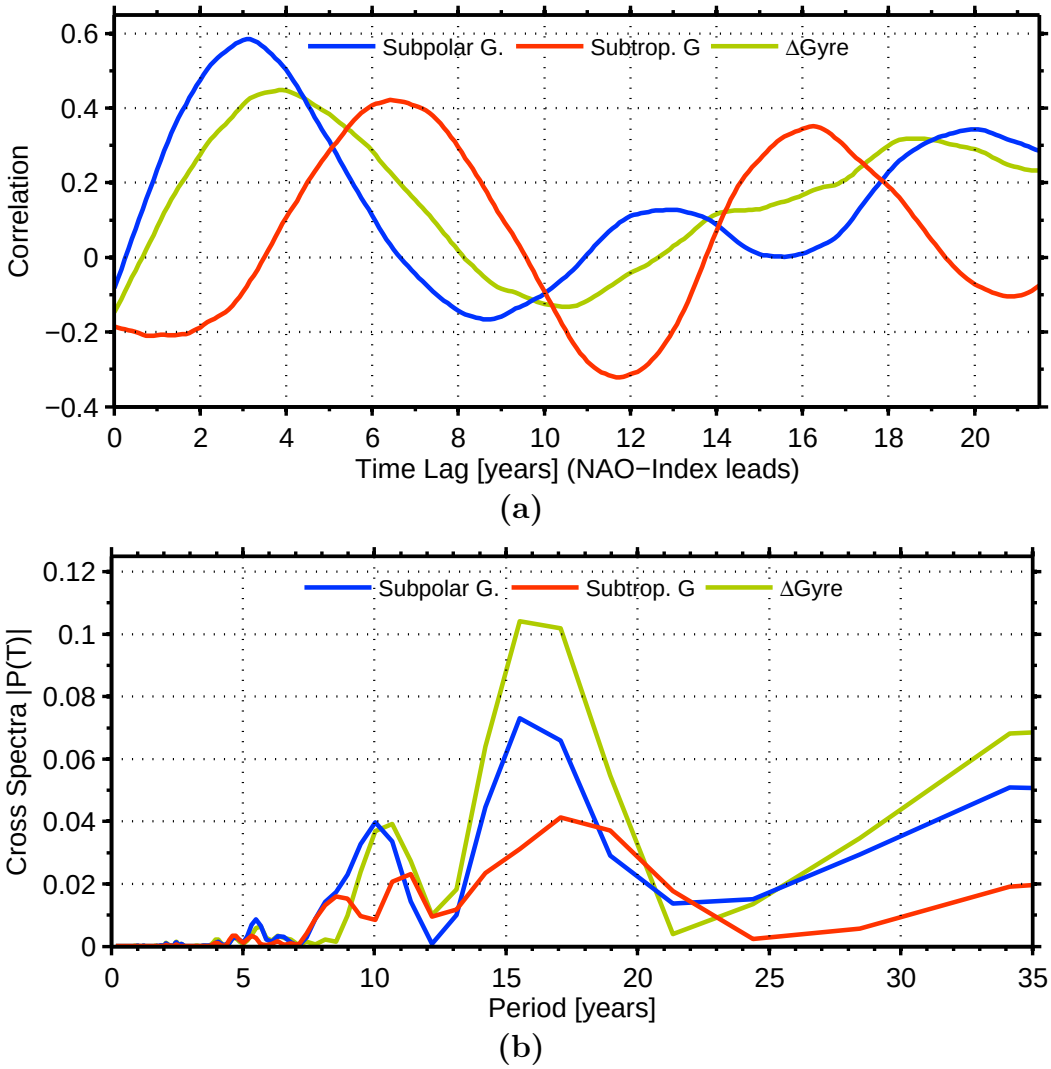

Fig. 7.5: *Lag correlation analysis (NAO leads) (a) and cross spectra analysis (b) of the subpolar gyre (blue), subtropical gyre (red) and ΔGyre (green) index with the NAO index. The time-series are smoothed with a 3 year-running-mean filter.*

gradient between the Azores High and the Icelandic Low [*Hurrell*, 1995].

Fig. 7.5a shows the lag-correlation analysis of the 3 year-running mean filtered time series of SPG (blue), STG (red) and ΔGyre (green) indices with the filtered NAO index, which leads in the lag-correlation analysis. The results show that the SPG index and the NAO index (Fig. 7.5a, blue curve) have a maximum correlation of 0.58 at a lag of

3.1 years and two more significant but weaker correlation maxima at a lag of 13 and 20 years, respectively. The lag-correlation between the filtered STG index and the NAO index (Fig. 7.5a, red curve), features a maximum correlation of 0.42 at a lag of 6.4 year. Another correlation maxima of 0.35 is at a lag of 16.25 years, as well as a t-test verified significant anti-correlation peak of -0.32 at a lag of 11.75 years. The results of the lag-correlation analysis between the ΔGyre and NAO index feature the highest correlation of 0.45 at lag of 3.9 years as well as a weaker correlation maxima at a lag of 18.7 years. We superimposed in Fig. 7.4 the winter (DJF) seasonal NAO index, shifted by the lag with the highest correlation for all three gyre indices. It shows that the STG, SPG and ΔGyre index correlates only on interannual to decadal time-scales with the NAO index.

Fig. 7.5b shows the cross-spectra analysis of the SPG, STG and ΔGyre indices relatively to the NAO index. The cross-spectrum between the SPG and NAO index, as well as between the ΔGyre index and the NAO index features a maximum peak at a period of $\sim$ 16 years, as well as a weaker peak at a period of $\sim$ 10 years. The $\sim$ 16 years periodicity in the cross-spectrum of the ΔGyre index is more pronounced. The cross spectrum of the STG index shows a broad peak at a period of $\sim$ 17 years and two weaker periodicities at a period of 8.5 and 11.4 years.

7.3 Comparison of modelled and observation based baroclinic mass transport index

To validate the model results of the gyre indices, we compare in Fig. 7.6 the baroclinic mass transport (BMT) index calculated from observations by *Curry and McCartney* [2001] to an analogue model ΔGyre index. The baroclinic mass transport index (red) in Fig. 7.6a features a mean value of $\sim$ 56 Sv, while the model ΔGyre index shows a mean value of 78.5 Sv. The model tends to overestimate the magnitude of the BMT index by a factor of 1.4. To compare the variability of the modelled ΔGyre and observational BMT index we look at the normalized indices (Fig. 7.6b). The normalized ΔGyre index and observational BMT index feature a correlation of 0.53 with a significance of 99.986% (t-test). Both time series reveal a maximum in the early 1960s, where the variability of the modelled ΔGyre index (green) is overestimated. The observational

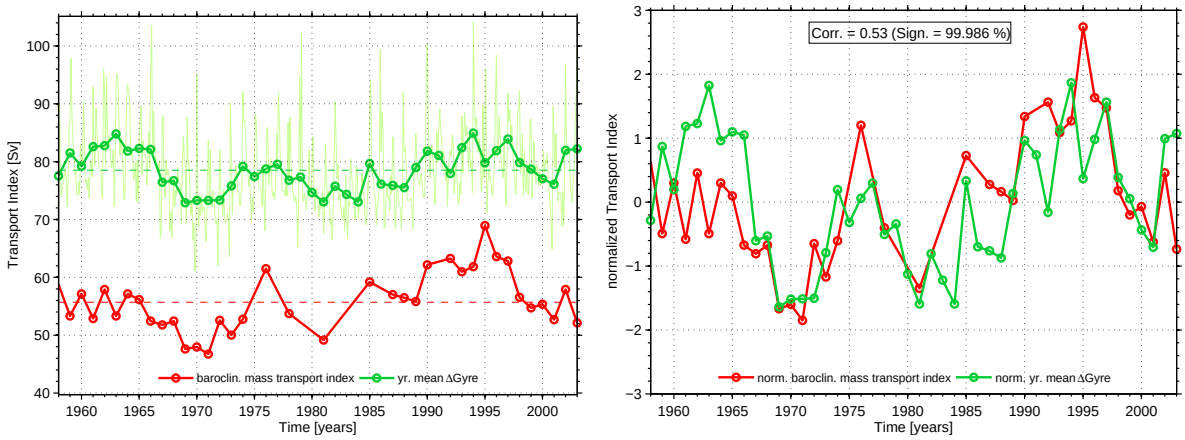

Fig. 7.6: *Comparison between the annual ΔGyre index (green) and observational-based baroclinic mass transport index (red) of Curry and McCartney [2001]. (a): absolute values, (b): normalized values. The normalized time series of the ΔGyre and baroclinic mass transport index show a correlation of* 0.53 *(significance=* 99.996%*).*

time series features another two maxima in the middle of the 1970s and 1980s, whose variability is sufficiently well reproduced by the model ΔGyre index. In the middle of the 1990s the normalized observational BMT index shows a broad maximum with its highest amplitude. Also the model ΔGyre index features in this time interval a broad maximum, where the amplitude is slightly below the observational values.

7.4 3D POP analysis of ocean temperature

In order to identify the important oscillatory modes in the North Atlantic Ocean we applied a POP analysis to a 3D temperature field of the normal forced FESOM run in the North Atlantic sector (100°W-45°E, 0°-80°N) for 20 levels between 10 m and 3600 m. The space-time temperature data that extends over the time period 1958-2004 were detrended, normalized and their monthly cycle was removed. Furthermore, we filtered the model data with a 3 year-running-mean filter. To reduce the size of the problem and to limit the degrees of freedom we applied an EOF analysis, where only the 12 leading EOFs, that account for 96.58% of the explained variance, were maintained

POP Nr.	stability	period T [yr]	e-fold τ [yr]	coherence	phase Φ [deg]
1	9.8	8.7	85.7	1.0	90.3
2	8.0	6.7	54.1	1.0	86.5
3	2.7	11.1	30.3	1.0	89.3
4	2.3	14.1	32.9	0.8	90.1
5	0.7	23.7	17.0	0.3	97.1
6	0.6	30.5	18.0	0.1	81.3

Table 7.1: *Results of the 3D temperature POP analysis of 20 vertical levels from 10 m to 3600 m. Prior the POP analysis the data are detrended and normalized, the monthly cycle is removed and a 3 year-running-mean filter is applied. Further an EOF analysis is performed, were the 12 leading EOFs are used, which describe 96.78% of the variance.*

for the POP-analysis. The characteristic parameters (stability, period T, damping time τ, phase angle Φ and coherence) of the 3D temperature POP analysis, ordered by the stability parameter, are listed in table 7.1. The POP analysis reveals 6 complex POP modes, from which 4 turned out to be *stable*. The POP modes with periods of 8.7 and 6.7 years, feature an exceptional high stability parameter of 9.8 and 8.0, respectively. In the following subsections we will describe each of the stable POP modes.

1st POP mode

Fig. 7.7a and 7.7b shows the real Re$\{\mathbf{p_1^i}\}$ and imaginary Im$\{\mathbf{p_1^i}\}$ POP pattern of the most stable mode $\mathbf{p_1^i}$ with a period of 8.75 yr and a damping time of 85.68 yr, respectively. We show the horizontal patterns for 6 different depth levels between 50 m-3600 m. The time evolution of the corresponding real and imaginary POP coefficient $\mathbf{z_1^i}$ is presented in Fig. 7.8.

The 50 m depth layer of the real part Re$\{\mathbf{p_1^i}\}$ (Fig. 7.7a) of this POP pattern shows a slight positive loading in the entire east and subtropical North Atlantic Ocean as well as in the central Labrador Sea and Irminger Sea with weak negative loadings in the Boundary Current system of the Labrador Sea, Baffin Bay, Norwegian Sea as well as at the location of the northern Gulf Stream branch. The latter negative loading anomaly in the pathway of the Gulf Stream extends through all subjacent layers. Further, the real pattern of this POP mode reveals in the western North Atlantic Ocean at

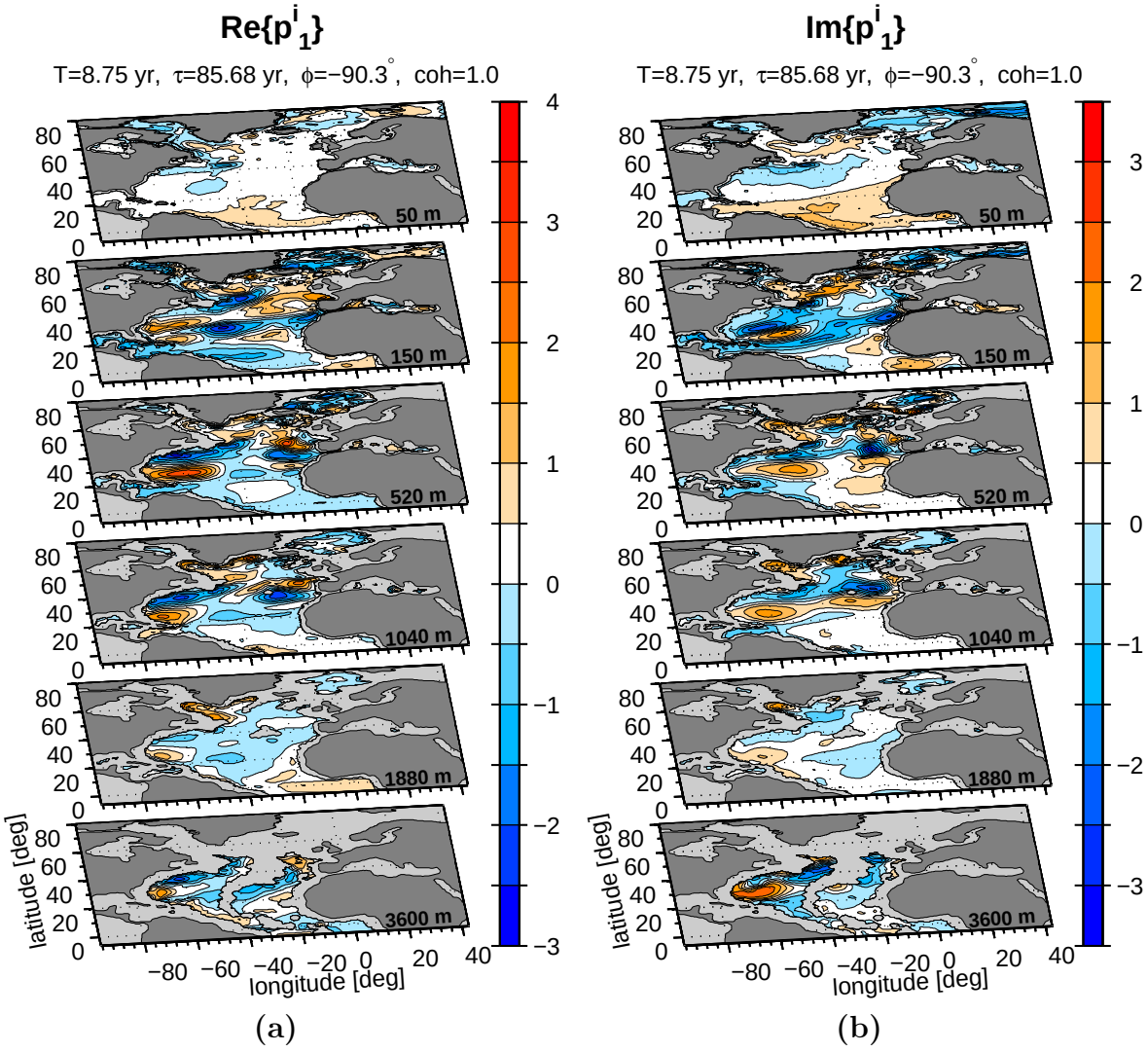

Fig. 7.7: *Real part (a) and imaginary part (b) of POP-pattern* $\mathbf{p_1^i}$ *for the depths* 50 *m*, 150 *m*, 520 *m*, 1040 *m*, 1880 *m and* 3600 *m. Period* T *and damping time* τ *of this pattern are* 8.7 *yr and* 85.7 *yr, respectively.*

$\sim 25^{\circ}$N a positive loading anomaly that extends with decreasing amplitude from 150 m-3600 m. The 150 m depth layer features positive loadings in the central Labrador Sea and Irminger Sea that reach until the 1880 m depth layer. The real pattern shows at the North Atlantic east coast a positive loading anomaly at around 45°N and a negative loading anomaly at around 30°N which extends from 150 m-1040 m.

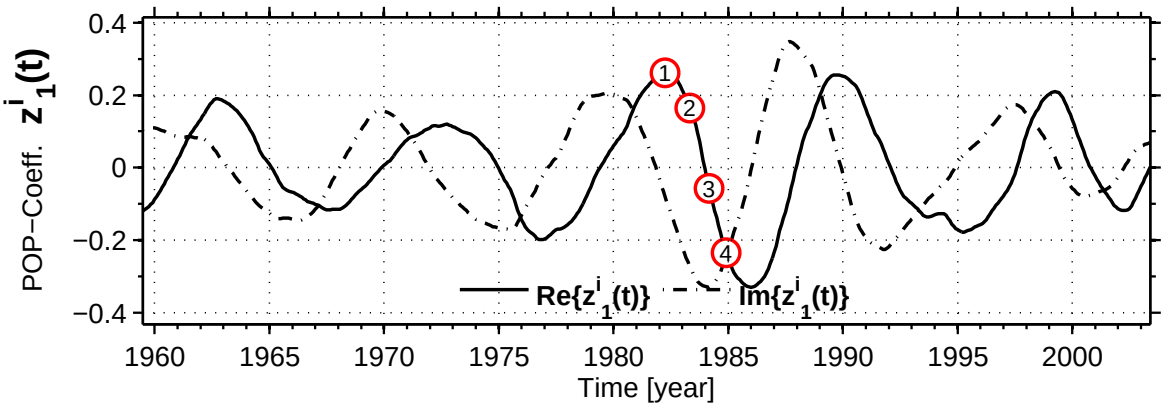

Fig. 7.8: *Real Re*$\{\mathbf{z}_1^i\}$ *(solid line) and imaginary part Im*$\{\mathbf{z}_1^i\}$ *(dashed dotted line) of the corresponding POP-coefficient. Numbered red circles mark the used time slices in Fig. 7.9.*

The imaginary part Im$\{\mathbf{p}_1^i\}$ of this pattern (Fig. 7.7b) features in the 50 m layer positive loadings in the Labrador Sea and subtropical North Atlantic Ocean as well as negative loadings in the pathway of the Gulf Stream, Greenland Sea and Norwegian Sea. The imaginary pattern of the subsequent layers display further a negative loading anomaly in the pathway of the Gulf Stream which extends through all layers as well as positive loadings in the Labrador Sea and subtropical North Atlantic Ocean that extends until 1040 m. Further the imaginary pattern of this POP mode shows a local positive loading anomaly in the North Atlantic at around 60°W, 25°N, which reaches until 3600 m.

Fig. 7.9 shows the time evolution of the $\mathbf{p}_1^i$ POP pattern over half a POP cycle at four distinct time points t_1 to t_4, that are indicated by the red circles in Fig. 7.8. The time evolution in the surface layers (10 m - 50 m) of this POP mode is dominated by a periodically eastward extending and retreating loading anomaly in the subtropical North Atlantic Ocean (not shown). The time evolution of the subsequent layers of this POP mode features a propagating loading anomaly in form of a Rossby wave that has its origin at the North Atlantic east coast at around 10°W, 30°N in a depth between 100 m - 240 m and propagates southeastward in the direction of the Greater Antilles. While the loading anomaly is propagating southeastward, it extends vertically until it reaches a depth of 3600 m at the western continental slope. There, the loading

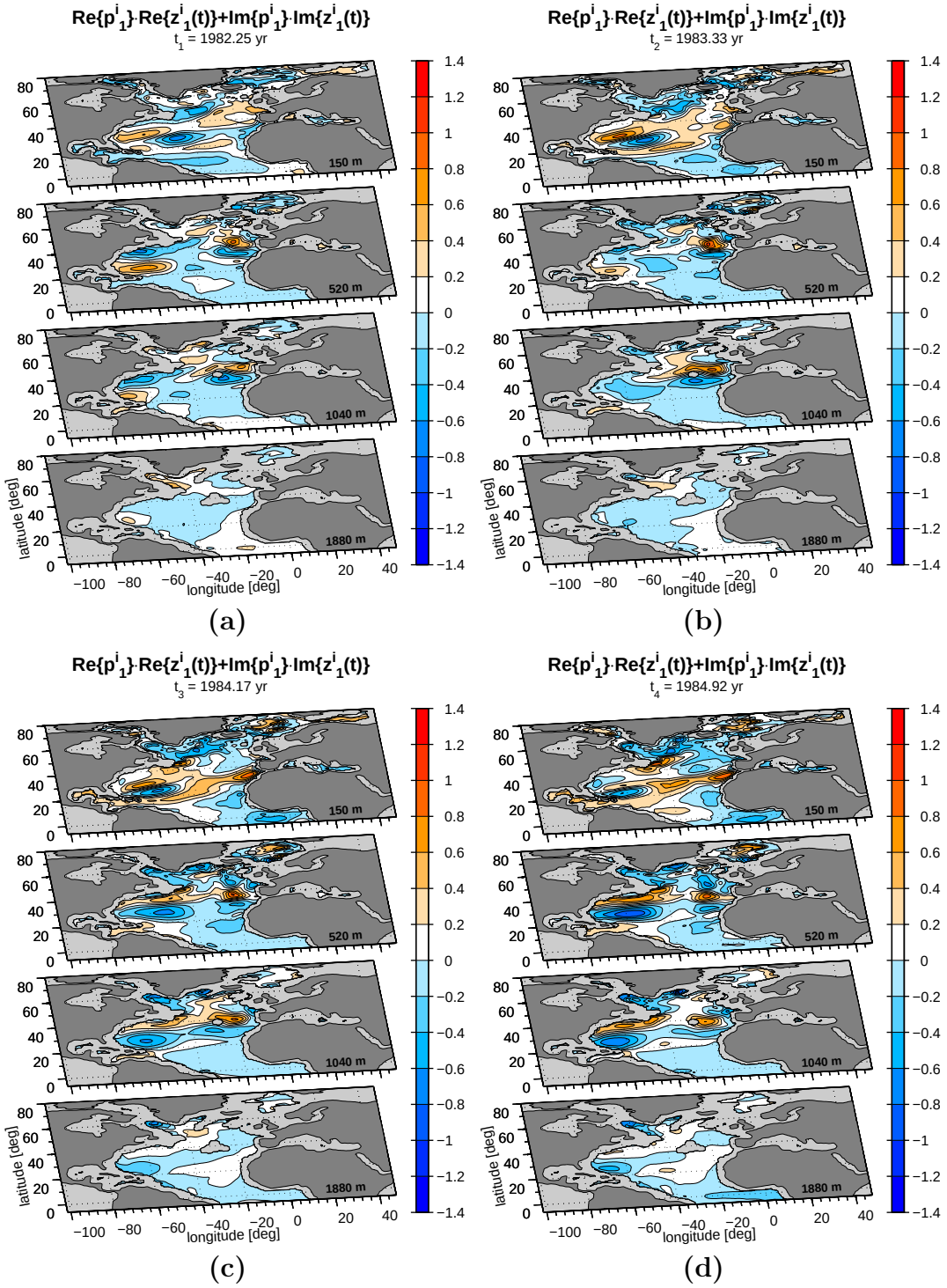

Fig. 7.9: *(a)-(d): Time evolution, over half a period, of POP-pattern* $\mathbf{p_1^i}$, $\mathbf{z_1^i(t)}$ *at the time steps* $t_1 = 1982.25$ *yr,* $t_2 = 1983.3$ *yr,* $t_3 = 1984.17$ *yr and* $t_4 = 1984.92$ *yr, which are indicated by labeled red circles in Fig. 7.8.*

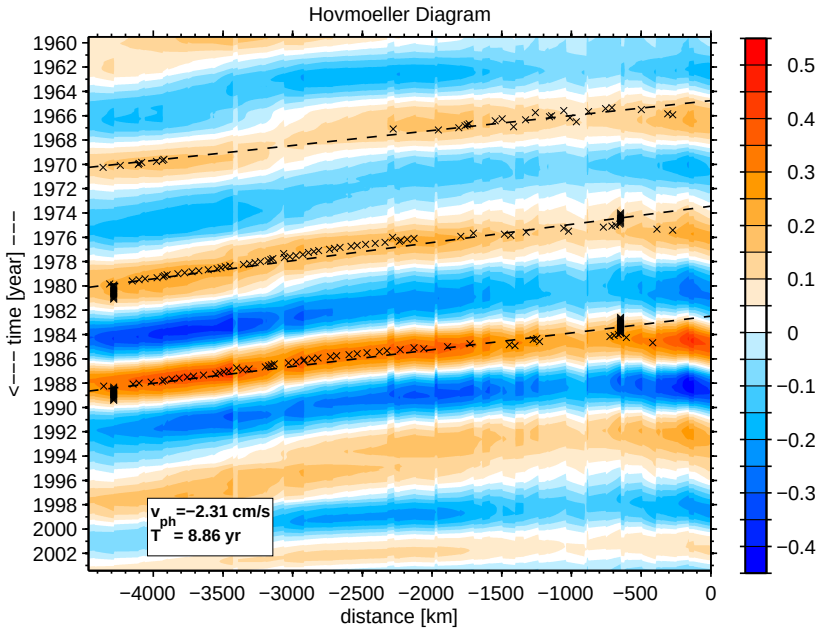

Fig. 7.10: *Hovmöller Diagram of the time evolution of the POP-pattern* $\mathbf{p_1^i}$ *averaged over the depth layers* 100 *m* - 340 *m, at a cross section from* 15° *W,* 32° *N to* 60° *W,* 22° *N. Dashed lines indicate the linear fit of the wave crest points that is used to determine the phase velocity of* $v_{ph} = -2.31$ *cm s*$^{-1}$ *and period of* $T = 8.86$ *yr of the Rossby wave.*

anomaly enters the branch of the Western Boundary Current and follows northward the pathway of the Gulf Stream and North Atlantic Current. From there, we can track how the loading anomaly enters the recirculation regimes of the subpolar and subtropical gyre and recirculates within the subtropical gyre southward.

Fig. 7.10 shows the Hovmöller Diagram for the time evolution of the $\mathbf{p_1^i}$ POP pattern averaged between the depth layers 100 m-350 m at a cross section that reaches from the North Atlantic Ocean east coast at 15°W, 32°N until 60°W, 22°N. The Hovmöller diagram reveals for the time evolution of this pattern an eastward traveling Rossby wave structure with a period of $T = 8.86$ yr. The slope of the wave crest points reveals a westward phase velocity of -2.31 cm s^{-1} which is in the typical order of a baroclinic Rossby wave [*Gill*, 1982; *Chelton and Schlax*, 1996; *Killworth et al.*, 1997].

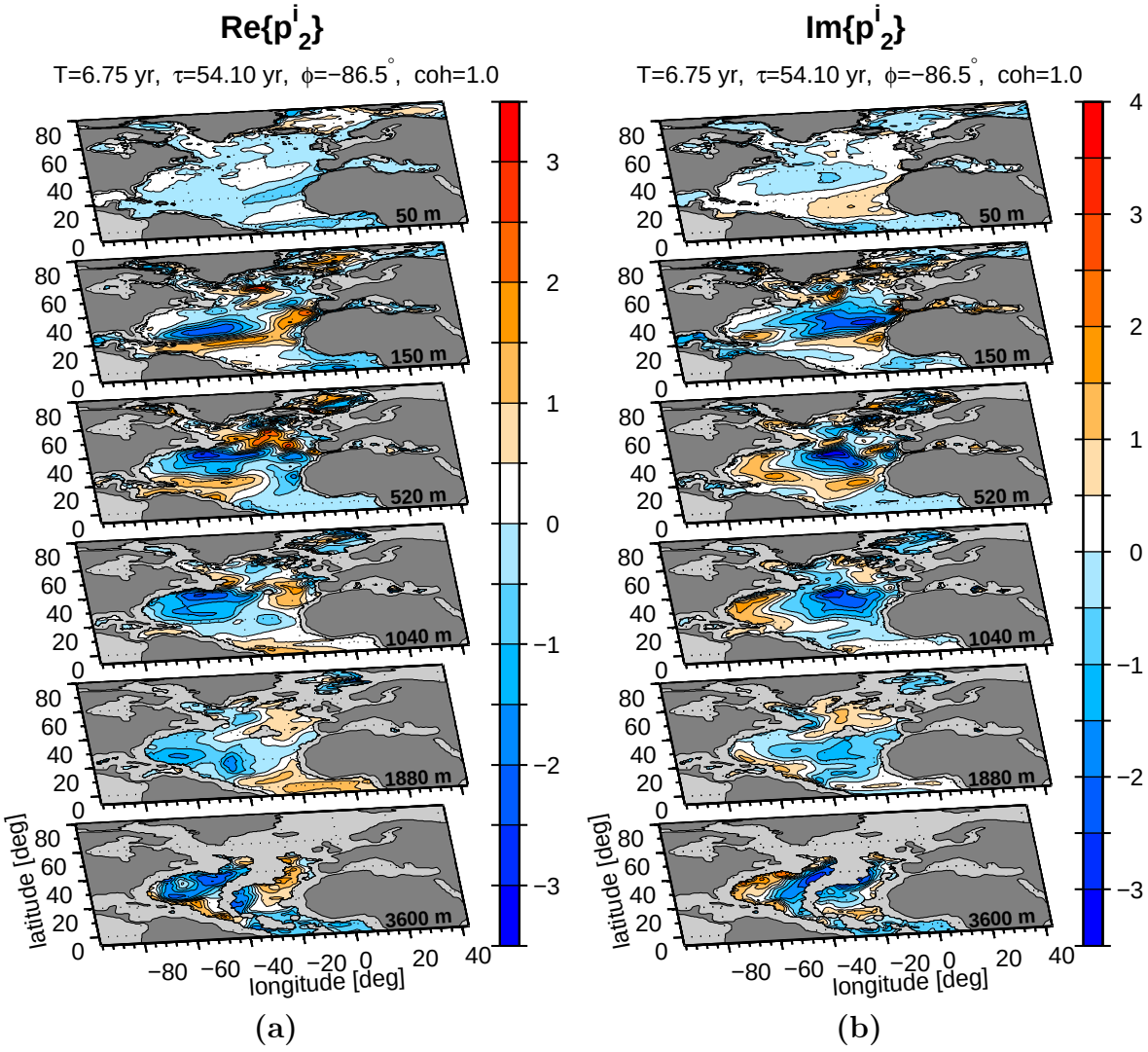

Fig. 7.11: *Real part (a) and imaginary part (b) of POP-pattern* $\mathbf{p_2^i}$ *for the depths* 50 *m*, 150 *m*, 520 *m*, 1040 *m*, 1880 *m and* 3600 *m. Period* T *and damping time* τ *of this pattern are* 6.75 *yr and* 54.1 *yr, respectively. Thus the stability of this pattern is with a value of* 8.0 *exceptional high.*

2nd POP mode

Fig. 7.11a and 7.11b show the real Re$\{\mathbf{p_2^i}\}$ and imaginary Im$\{\mathbf{p_2^i}\}$ POP pattern of the second most stable mode $\mathbf{p_2^i}$ with a period of 6.75 yr and a damping time of 54.68 yr, respectively. Shown are the horizontal patterns for 6 different depth levels between

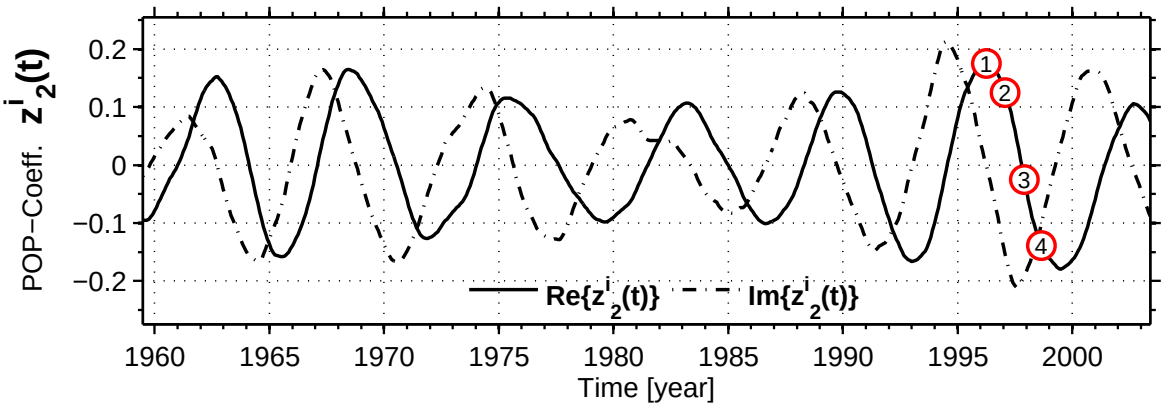

Fig. 7.12: *Real $Re\{\mathbf{z_2^i}\}$ (solid line) and imaginary part $Im\{\mathbf{z_2^i}\}$ (dashed dotted line) of the corresponding POP-coefficient. Numbered red circles mark the used time slices in Fig. 7.13.*

50 m-3600 m. Fig. 7.12 presents the time evolution of the corresponding real and imaginary coefficient $\mathbf{z_2^i}$ is shown in.

The main features of this POP mode are high negative loadings of the real and imaginary part in a zonal corridor between 20°N-40°N of the central North Atlantic Ocean. These loading anomalies reach from the surface through all considered depth layers. The real part has in the 150 m and 520 m depth layer positive loadings in the subtropical North Atlantic Ocean as well as in the Irminger Sea. The deeper layers (1040 m-1880 m) of the real part reveals positive loadings in the equatorial Atlantic Ocean. The imaginary part feature additionally positive loadings along the western continental slope that reaches from 520 m up to 3600 m.

The time evolution of the real and imaginary part of the POP coefficient $\mathbf{z_2^i}$ (Fig. 7.12) shows more pronounced amplitudes in the first and last third of the simulation period. The red numbered circles in Fig. 7.12 mark the time points that are used to illustrate in Fig. 7.13 the time evolution of the 6.7 year POP mode $\mathbf{p_2^i}$ over a half POP cycle. The considered time steps t_1 to t_4 are separated by $\sim$ T/8.

The time evolution of this pattern is dominated by a large scale westward propagating loading anomaly in a zonal band $\sim$ 36°N, that extends through the whole considered water column in the North Atlantic Ocean. We associated this large-scale propagating loading anomaly to a Rossby wave that originates from the European continental shelf

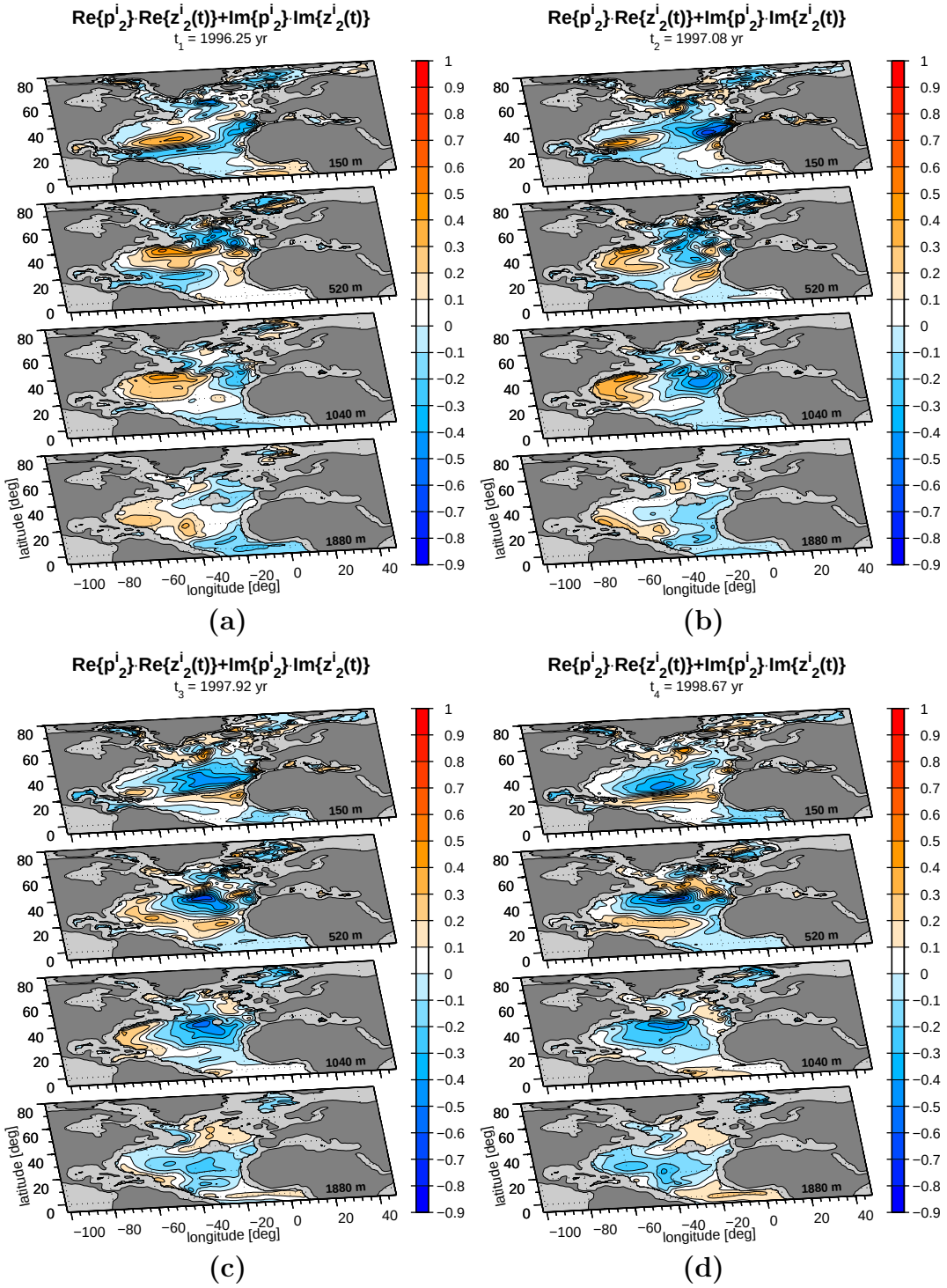

Fig. 7.13: *(a)-(d): Time evolution of POP-pattern* $\mathbf{p_2^i}$, $\mathbf{z_2^i(t)}$ *at the time steps* $t_1 = 1996.25$ *yr,* $t_2 = 1997.08$ *yr,* $t_3 = 1997.92$ *yr and* $t_4 = 1998.67$ *yr, which are indicated by labeled red circles in Fig. 7.12.*

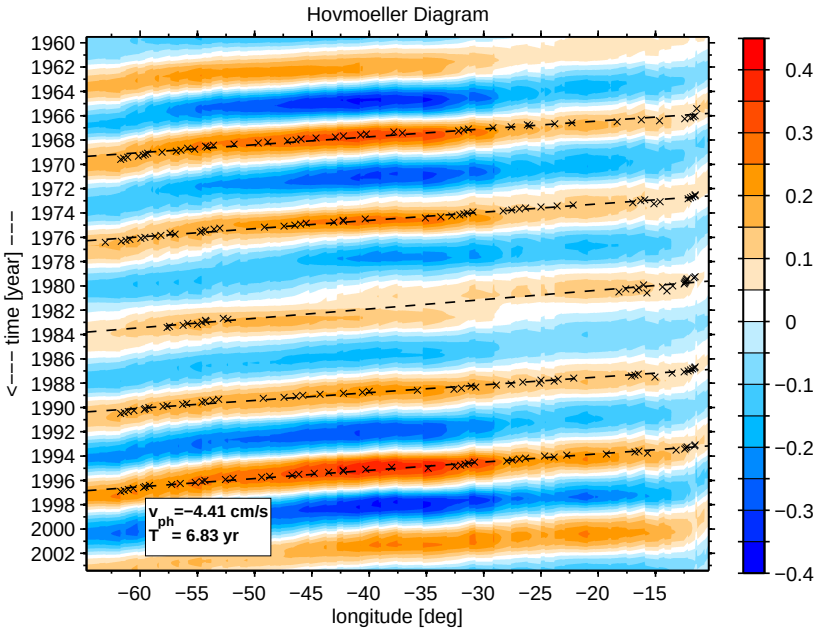

Fig. 7.14: *Hovmöller Diagram of the time evolution of the POP-pattern* $\mathbf{p_2^i}$ *averaged over all 20 vertical levels, at a latitude of* $36^\circ N$ *and a longitude range from* $65^\circ W$-$10^\circ W$. *Dashed lines indicate the linear fit of the wave crest points that is used to determine the phase velocity of* $v_{ph} = -4.41\ cm\,s^{-1}$ *and period of* $T = 6.83\ yr$ *of the Rossby wave.*

at around 35°N. At the North Atlantic west coast the resulting loading anomaly follows the continental slope and turns southward in a Kelvin wave-like structure. The time evolution of this pattern features further an eastward traveling equatorial Kelvin wave-like structure below a depth of 1040 m. Another loading anomaly in form of a Rossby wave, that is in antiphase to the previous described Rossby wave structure around $\sim 36^\circ$N propagates westward at around 20°N. This loading anomaly reaches only into a depth of around 520 m. The equatorial Atlantic features an eastward extending loading anomaly that could be related to a equatorial Kelvin wave.

To further analyse the Rossby wave structure at $\sim 36^\circ$N in the $\mathbf{p_2^i}$ POP mode, we averaged the real part $\mathrm{Re}\{\mathbf{p_2^i}\}$ and imaginary part $\mathrm{Im}\{\mathbf{p_2^i}\}$ of the POP pattern over all 20 vertical depth layers. Then, we calculated for the time evolution of the depth averaged POP mode for a zonal cross-section between 60°W, 36°N-10°W, 36°N, the zonal Hovmöller diagram (Fig. 7.14). The Hovmöller diagram features a clear westward

traveling Rossby wave structure. The linear fit of the wave crest points (dashed lines in Fig. 7.14) reveals that the wave structure has a period of 6.83 years and a phase velocity of −4.41 cm/s, which also links to a baroclinic Rossby wave structure [*Gill*, 1982; *Chelton and Schlax*, 1996; *Killworth et al.*, 1997].

3rd POP mode

The real and imaginary POP pattern $\mathbf{p_3^i}$ of the 3rd most stable POP mode with a period of 11.09 yr and a damping time of 30.30 yr is shown in Fig. 7.15a and 7.15b, respectively. Fig. 7.16 displays the time evolution of the corresponding real and imaginary coefficient $\mathbf{z_3^i}$.

The real part of this POP pattern is characterized in the 150 m depth layer by negative loadings in the region of the Western Boundary current, North Atlantic Current, Norwegian Sea as well as at the west coast of Africa at around 20°N. Positive loadings in the real part are present in the central North Atlantic Ocean as well as in the Irminger Sea and Labrador Sea. The subsequent layers (520 m-3600 m) have negative loadings in the central and western North Atlantic Ocean around 20°N and positive loadings in the Labrador Sea. The 520 m depth layer of the real part of this POP mode has positive loadings at the entire North Atlantic west coast as well as in the equatorial Atlantic Ocean. The deeper layers (1040 m- 3600 m) feature positive loadings in the subtropical North Atlantic as well as negative loadings around the equator. The maximum of the positive subtropical loading anomaly is shifted in the 3600 m depth layer to the western continental slope.

The imaginary part of this pattern is characterized in the 150 m-1880 m depth layer by positive loadings in a zonal band around 20°N-∼ 30°N as well as negative loadings at the continental slope around Newfoundland and in the subtropical North Atlantic Ocean. The deeper layers (1040 m-1880 m) of the imaginary part present positive loadings in the equatorial North Atlantic Ocean. The 3600 m depth layer shows positive loadings at the western continental slope as well as negative loadings in the central North Atlantic Ocean.

The time evolution of the third POP mode (Fig. 7.17) is characterized by a Rossby wave-like loading anomaly that extends eastward in a zonal band around 25°N. This loading anomaly has high amplitudes between 240 m-1040 m. While it is propagat-

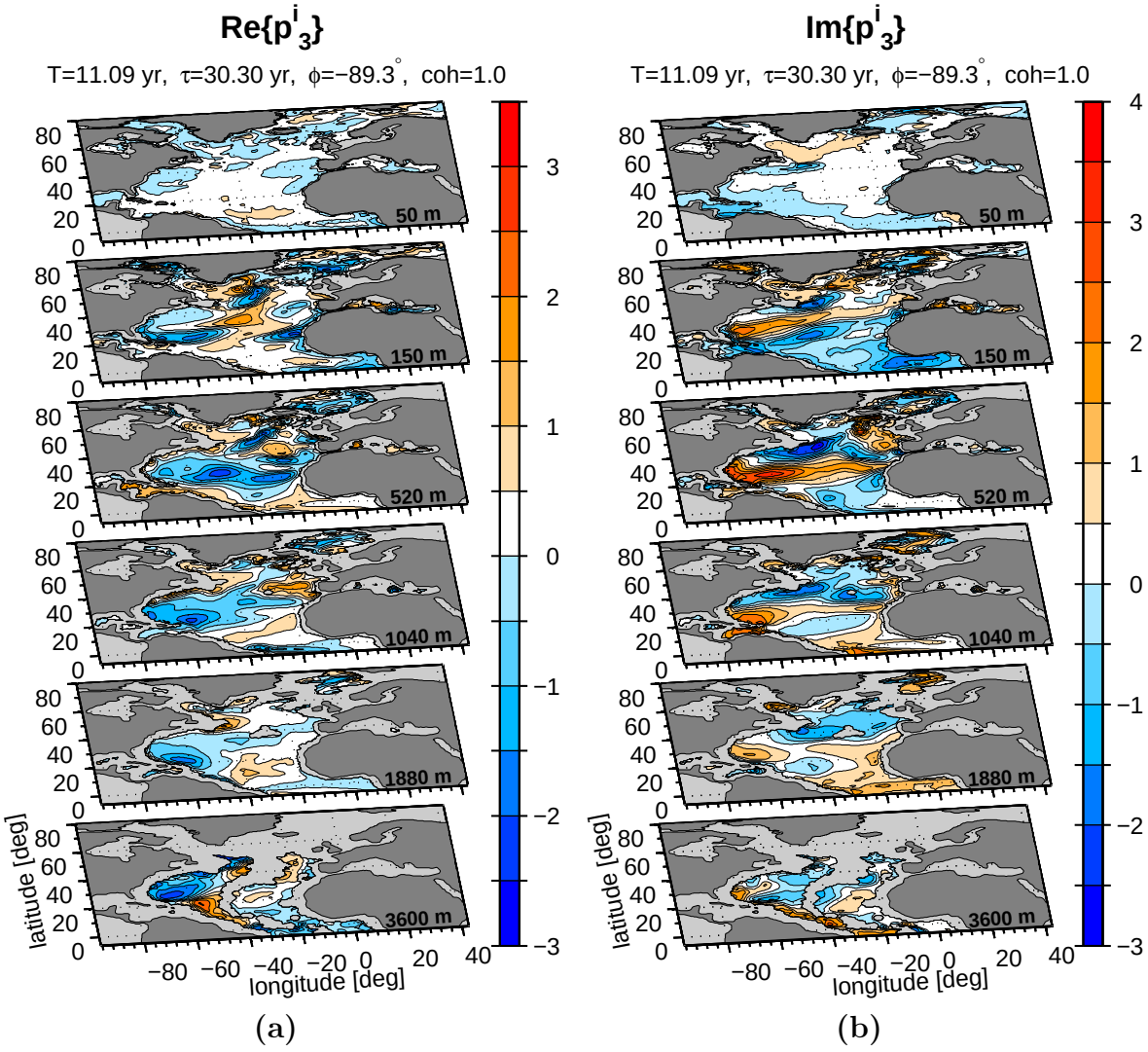

Fig. 7.15: *Real part (a) and imaginary part (b) of POP-pattern* $\mathbf{p}_3^{\mathbf{i}}$ *for the depths* 50 *m*, 150 *m*, 520 *m*, 1040 *m*, 1880 *m and* 3600 *m. Period* T *and damping time* τ *of this pattern are* 11.1 *yr and* 30.3 *yr, respectively.*

ing eastward it extends vertically until 3600 m on the western continental slope. This Rossby-like anomaly seems to originate from two locations at the North Atlantic east coast at $\sim 40^{\circ}$N and at $\sim 20^{\circ}$N. When the Rossby-like loading anomaly strikes the continental slope, the time evolution of the POP features a topographic Kelvin wave that travels southward along the continental slope and results in a equatorial Kelvin

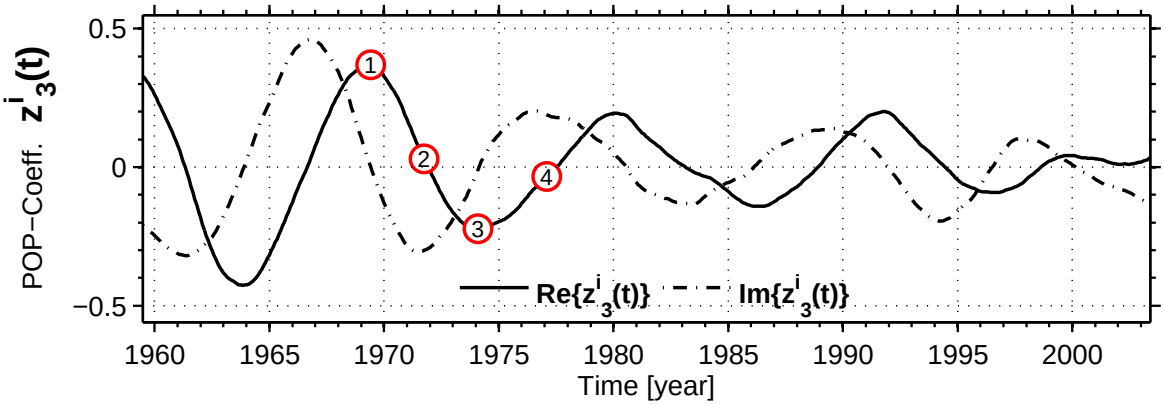

Fig. 7.16: *Real $Re\{\mathbf{z_3^i}\}$ (solid line) and imaginary part $Im\{\mathbf{z_3^i}\}$ (dashed dotted line) of the corresponding POP-coefficient. Numbered red circles mark the used time slices in Fig. 7.17.*

wave that travels westward below a depth of 1040 m. The time evolution of this mode has also a propagating loading anomaly south of Newfoundland that follows the pathway of the Gulf Stream and North Atlantic current and recirculates then within the subpolar and subtropical gyre.

4th POP mode

Different authors like *Deser and Blackmon* [1993] and *Dima and Lohmann* [2004] discussed a fundamental climate mode in the Atlantic Ocean with a period of $12-15$ years, that describes a certain amount of the variability in this region. The 3D temperature POP analysis of our model data reveals also a quasi-decadal mode with a period of 14.1 yr. The damping time of this POP mode ($\tau = 32.9$ yr) indicates also a sufficiently stable mode, with a stability parameter of 2.3. Fig. 7.18 displays the real part (Fig. 7.18a) and imaginary part (Fig. 7.18b) of POP mode $\mathbf{p_4^i}$ averaged over the upper 3 considered layers between 10 m - 100 m. The time evolution of the real part and imaginary part of the corresponding POP coefficients $\mathbf{z_4^i(t)}$ is presented in Fig. 7.18c.
The period and the averaged surface spatial structure of this POP mode resembles well the fundamental quasi-decadal pattern of 13.1 yr described by *Dima and Lohmann* [2004]. The averaged surface real part (Fig. 7.18a) of our quasi-decadal POP mode features a positive loading anomaly that extends from the Labrador Sea over the Irminger

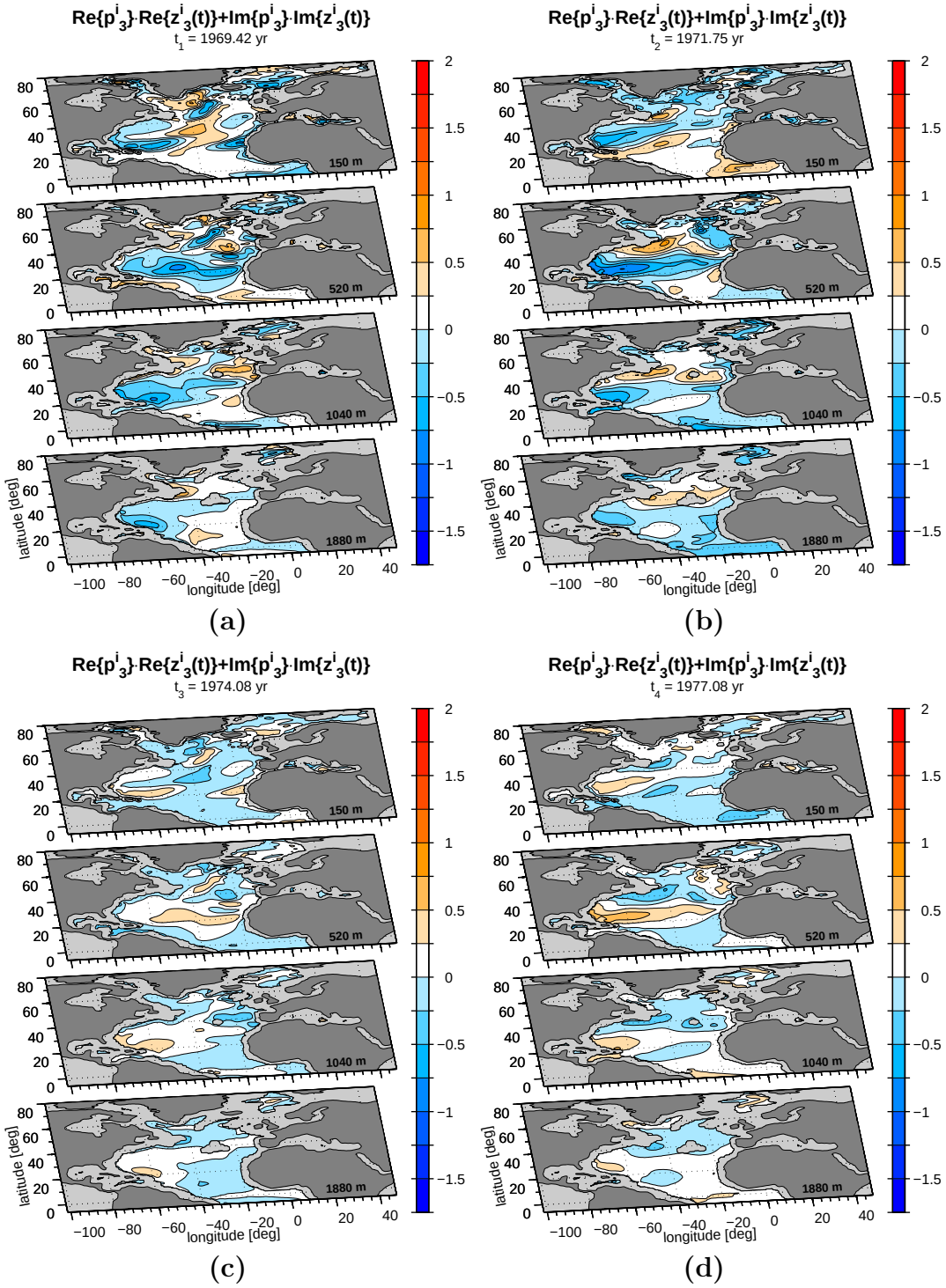

Fig. 7.17: *(a)-(d): Time evolution of POP-pattern* $\mathbf{p_3^i}$, $\mathbf{z_3^i(t)}$ *at the time steps* $t =$ 1969.42 *yr*, 1971.75 *yr*, 1974.08 *yr and* 1977.08 *yr, which are indicated by labeled red circles in Fig. 7.16.*

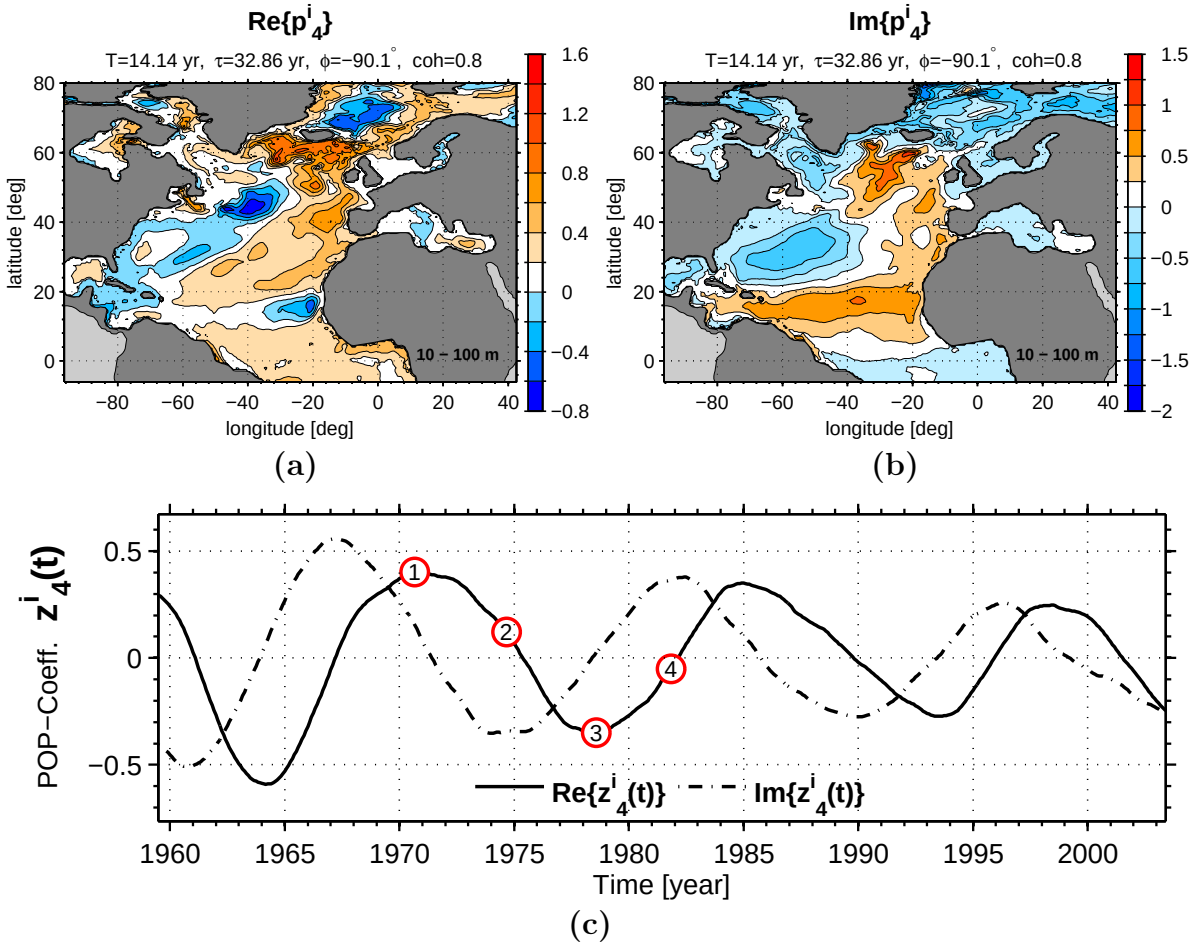

Fig. 7.18: *(a)-(b): Real part (a) and imaginary part (b) of POP-pattern* $\mathbf{p_4^i}$ *averaged over the upper 3 considered layers (10 m-100 m). The period* T *and damping time* τ *of this pattern are 14.1 yr and 32.9 yr, respectively. (c): Real part (solid line) and imaginary part (dashed dotted line) of the corresponding POP-coefficient* $\mathbf{z_4^i(t)}$*. Numbered red circles mark the used time slices in Fig. 7.20.*

Sea and the entire southeast North Atlantic Ocean. Negative loadings are present in the central Greenland Sea as well as in the pathway of the Gulf Stream and at the west coast of Africa. The surface averaged imaginary part (Fig. 7.18b) of the quasi-decadal pattern is characterized by a positive "horseshoe" like temperature anomaly pattern that extends from the Irminger Sea along the Atlantic east coast and the subtropical North Atlantic Ocean. Pronounced negative loadings are featured in the western and

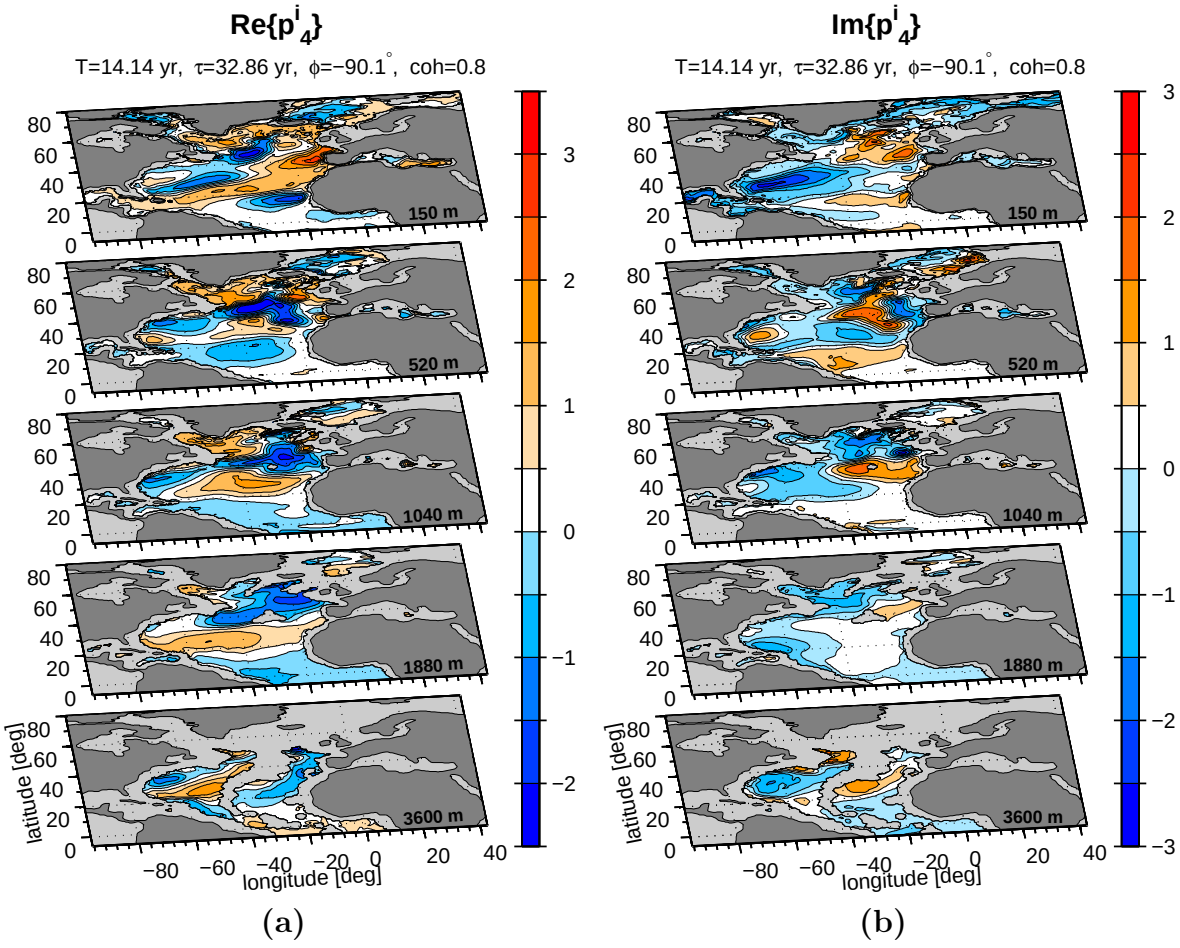

Fig. 7.19: *Real part (a) and imaginary part (b) of POP-pattern* $\mathbf{p}_4^{\mathbf{i}}$ *for the depths* 150 *m,* 520 *m,* 1040 *m,* 1880 *m and* 3600 *m. The period* T *and damping time* τ *of this pattern are* 13.9 *yr and* 20.6 *yr, respectively.*

central North Atlantic Ocean, Labrador Sea as well as Greenland Sea and Norwegian Sea. The surface time evolution of this pattern (not shown) describes the propagation of a loading anomaly that follows the pathway of Gulf Stream and North Atlantic Current. From there, the loading anomaly enters the recirculation regimes of the subtropical and subpolar gyres. A loading anomaly is then propagating southward in the eastern recirculation regime of the subtropical gyre.

The 3D POP analysis gives us the opportunity to have a look on the depth behavior of the quasi-decadal POP mode within our model. Up to now only a surface examination

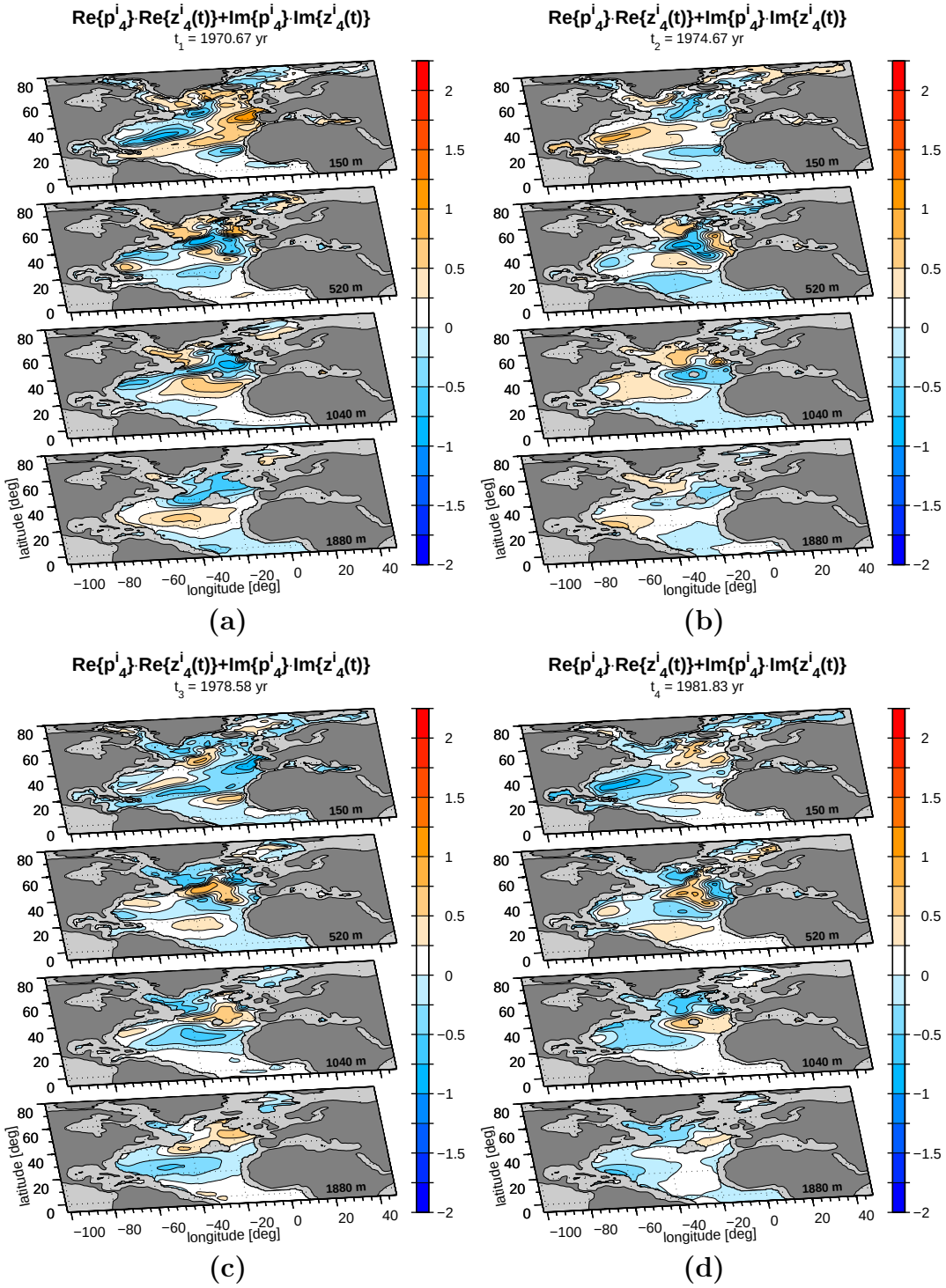

Fig. 7.20: *(a)-(d): Time evolution of POP-pattern* $\mathbf{p_4^i}$, $\mathbf{z_4^i(t)}$ *at the time steps* $t =$ 1970.67 *yr*, 1974.67 *yr*, 1978.58 *yr and* 1981.83 *yr, which are indicated by labeled red circles in Fig. 7.18c.*

of this mode was done. Fig. 7.19 shows the real part Re$\{\mathbf{p}_4^{\mathbf{i}}\}$ and imaginary part Im$\{\mathbf{p}_4^{\mathbf{i}}\}$ of the quasi-decadal POP for the depth layers 150 m, 520 m, 1040 m, 1880 m and 3600 m. The real POP pattern of the surface layer averaged POP (Fig. 7.18a) continues almost unmodified in the 150 m depth layer (Fig. 7.19a). In this layer, the negative loading anomaly at the west coast of Africa features an increased westward extent. With increasing depth (520 m-1880 m) in the real POP pattern (Fig. 7.19a) the negative loading anomaly in the pathway of the Gulf Stream dominates and extends eastward. This disconnects the positive loading anomalies of the Labrador Sea and the central North Atlantic Ocean. The negative loading anomaly in front of the African West Coast is further extending westward in the 520 m depth layer. The 1880 m layer shows a more tripole like structure in the North Atlantic with negative loading anomalies in the Northeast Atlantic Ocean and Irminger Sea as well as in the tropical Atlantic Ocean and positive loading anomalies in a zonal band at $\sim 23^{\circ}$N. The real part of the last considered depth layer of 3600 m features negative loading anomalies east of the Mid-Atlantic Ridge that extend southward, as well as on the western continental shelf. Positive loading anomalies are present west of the Mid-Atlantic Ridge.
The negative loading anomaly in the imaginary part of surface layer averaged POP $\mathbf{p}_4^{\mathbf{i}}$ in the central North Atlantic Ocean continues in the 150 m depth layer and extends more eastward with an amplitude which is twice as high than in the surface layers. With increasing depth (520 m-1880 m) the northern positive loading anomaly is shifting to the south due to an extending negative loading anomaly in the Irminger Sea. The negative loading anomalies in the central Atlantic Ocean at $\sim 25^{\circ}$N is extending more eastward in the 520 m depth layer, while in all subsequent layers this anomaly is retreating in favor of a positive loading that extends westward from the central North Atlantic east coast. The imaginary part of the 520 m depth layer features a local positive loading anomaly at the central North Atlantic west coast. The imaginary POP pattern in the deepest considered layer (3600 m) features a positive loading anomaly east of the Mid-Atlantic Ridge that extends to the southeast, as well as negative loading anomalies west of the Mid-Atlantic Ridge and in the subtropical North Atlantic Ocean. The time evolution (Fig. 7.20) of the deeper layers ($\geq$ 520 m) of this POP mode show a westward traveling loading anomaly at around 30°N. This loading anomaly seem to be directly connected to the surface anomaly that recirculates within the eastern branch

of the subtropical gyre.

7.5 Discussion of the interannual to decadal variability

In this chapter we described the decadal variability in the North Atlantic basin in a global FESOM setup that is designed to resolve the deep water formation areas in the Labrador Sea and Greenland Sea with a local refined resolution. We analysed the variability of different indices like NADW-, STG-, SPG- and ΔGyre index, under different forcing conditions (normal, random COREv2/SODA).
We calculated the NADW index for a normal and random COREv2/SODA forced FESOM setup run and determined the FFT spectra for both time series. The FFT spectra of the normal COREv2/SODA forced NADW index features, beside the annual peak, a pronounced variability around 14.2 yr, as well as periodicities around 7.8 yr and 4.7 yr, respectively. The improved Welch spectrum shows that the dominant periodicity in the normal forced COREv2/SODA run is the quasi-decadal periodicity of 14.2 yr. While the FFT and Welch spectrum of the random forced COREv2/SODA run, is dominated by an interannual periodicity of 7.1 yr, while the quasi-decadal periodicity of 14.2 yr almost vanishes. A SSA revealed that the quasi-decadal and interannual modes describes 28.7% and 23.6% of the total variance of the normal and random forced NADW index, respectively. The absence of the quasi-decadal periodicity in the random forced COREv2/SODA run allows the conclusion that the quasi-decadal periodicity of 14.2 yr is mostly connected to the external atmospheric forcing, while the interannual periodicity of 7.1 yr can be seen as an internal mode of the ocean or at least as a superposition of internal and external mode.
Further, we calculated for the normal COREv2/SODA forced run a ΔGyre index as the difference between the subtropical gyre (STG) and subpolar gyre (SPG) index. This index is calculated in analogy to the baroclinic mass transport (BMT) index of *Curry and McCartney* [2001] which is derived from observational data. The observational BMT and modelled ΔGyre serve as a kind of "oceanic NAO index" [*Curry and McCartney*, 2001]. The atmospheric NAO index [*Hurrell*, 1995] can be regarded as an estimator for the strength of the westerlies winds. The "oceanic NAO index" can be regarded as an

estimator for the strength of the eastward baroclinic flow along the boundary between the subpolar and subtropical gyre [*Curry and McCartney*, 2001].
We compared the modelled SPG, STG and ΔGyre index to the atmospheric NAO index and calculated the lag-correlation between the gyre indices and the NAO index. We found in the time evolution of the SPG index four maxima around 1965, 1977, 1985 followed by a strong increase between 1988 and 1995, when the index reaches its maximum value. Afterwards the SPG index declines by ~ 7 Sv until 2000. A similar behavior in 90s is mentioned by *Häkkinen and Rhines* [2004], who found a substantial decline in their observational sea surface height based subpolar gyre index after 1994. They suggested that this decline can be linked to a drop in the deep convection of the central Labrador Sea in the middle of the 1990s. A regional high resolution model study of *Böning et al.* [2006] and coarser model study of *Lohmann et al.* [2009] showed that a large part of the long term variability of the gyre transport is driven by changes in heat flux and wind stress. The lag-correlation between the modelled SPG and NAO index reveals a maximum correlation when the NAO index leads the SPG index by 3 yr, while the lag correlation of the STG and NAO index features a maximum significant correlation at a lag of 6.4 yr. *Curry and McCartney* [2001] determined that the baroclinic mass transport index lags the atmospheric NAO index by perhaps one or two years. The lag-correlation of our modelled ΔGyre index with the NAO index reveals a maximum lag of 3.9 yr when the NAO index leads, which indicates a twice as higher lag than estimated by *Curry and McCartney* [2001].
The cross spectra analysis between the three gyre indices and the NAO index revealed that the SPG, STG and ΔGyre index share the same ~ 16 yr periodicity with the NAO index. Furthermore, the SPG and ΔGyre index share a weaker ~ 10 yr periodicity with the NAO index. The cross spectrum of the STG index shows weaker periodicities of ~ 8 yr and $11 - 12$ yr, respectively.
We also performed a direct comparison between the absolute and normalized annual observational BMT index of *Curry and McCartney* [2001] with the annual modelled ΔGyre index for the interval 1958-2004. The comparison of the absolute indices revealed that our model tends to overestimate the BMT index of *Curry and McCartney* [2001] by a factor of 1.4. However, from the comparison of the normalized indices we can conclude that the overall time evolution and variability of the modelled ΔGyre

index is in very good agreement with the BMT index.

Principal Oscillation Pattern (POP) analysis introduced by *Hasselmann* [1988] and *von Storch et al.* [1995] has been applied to a 3D temperature field of the North Atlantic Ocean. The POP analysis is a widely used tool in climate science to study the 2D surface spatio-temporal structure of important oscillatory modes in the climate system [*Dima and Lohmann*, 2004; *Park and Latif*, 2010; *Ding et al.*, 2010]. In this study we extended the common POP analysis to a three dimensional data field to visualize not only the horizontal structure but also the vertical structure of the dominant oscillatory modes over the North Atlantic Ocean. The POP analysis of our 3D temperature field revealed 4 stable modes with periods of 6.7 yr, 8.7 yr, 11.1 yr and 14.1 yr, respectively. The POP modes with a period of 6.7 yr and 8.7 yr revealed to be exceptional persistent with high damping times of 51.1 yr and 85.7 yr, respectively. The stable periodicities identified by the POP analysis are in the range of values described by different authors [e.g., *Moron et al.*, 1998; *da Costa and de Verdiere*, 2002; *Dima and Lohmann*, 2004]. The most stable POP mode with a period of 8.7 yr is dominated by a Rossby wave-like structure in the intermediate depths that propagates westward from the Atlantic west coast of North Africa towards the Greater Antilles as well as a temperature anomaly that travels northward in the branch of the Gulf Stream and North Atlantic Current. The Rossby wave that is connected with this POP mode features a phase speed of $-2.31\ \mathrm{cm\,s^{-1}}$, which identifies this wave as a baroclinic Rossby wave. On the western continental slope a temperature anomaly follows the pathway of the Gulf Stream northward. A similar connection between a westward traveling Rossby wave and a propagating temperature anomaly in the branch of the Gulf Stream is described by *da Costa and de Verdiere* [2002] with a periodicity of 7.7 yr.

Also the 6.7 yr POP mode is characterized by a westward propagating Rossby wave-like structure in a zonal waveguide around 36°N, where the oscillation goes this time through the whole considered water column. The phase speed of this Rossby wave ($-4.41\ \mathrm{cm\,s^{-1}}$) verifies its baroclinic character. *Cipollini et al.* [1997] and *Cromwell* [2001] found a similar Rossby waveguide in the North Atlantic Ocean around 34°N in TOPEX/POSEIDON satellite altimeter data, although the time length of their data did not allow them to verify Rossby wave with a period longer than four years. Furthermore, this POP mode features a southward propagating temperature anomaly at the

western continental slope that features the characteristics of a coastal trapped Kelvin wave. The equatorial region of this mode shows, below a depth of 1040 m, an eastward propagating temperature anomaly that could be related to an equatorial Kelvin wave [*Gill*, 1982; *Katz*, 1987].

We applied the same 3D temperature POP analysis, also to the random forced FESOM run which was not shown in this study. However, the POP analysis of the random forced run revealed also two exceptional stable modes with an interannual variability in the range of $7-9$ yr and with a comparable variability than the here described 8.7 yr and 6.7 yr POP modes. This allows the conclusion that these two POP modes can be attributed to internal modes of the ocean which supports our findings from the spectral analysis of the normal and random forced NADW index regarding the interannual variability of 7.1 yr.

The 11.1 yr POP mode features also a Rossby-like loading anomaly in the intermediate depth range, where the source region is not clearly defined. Also, for this mode we could identify a southward propagating Kelvin wave-like structure at the western continental slope as well as an equatorial Kelvin wave-like structure that connects the western and eastern equatorial Atlantic below a depth of 1040 m. Additionally, we identify a propagating temperature anomaly that has its origin south of Newfoundland and follows the pathway of the Gulf Stream and North Atlantic current and enters the recirculation regime of the subpolar and subtropical gyre.

The surface pattern of the quasi-decadal POP mode with a period of 14.14 yr agrees well with the fundamental mode described by *Deser and Blackmon* [1993] and *Dima and Lohmann* [2004]. *Dima and Lohmann* [2004] described for this mode a propagating SST anomaly in the branch of the Gulf Stream that enters the recirculation systems of the subpolar and subtropical gyres. Their mechanism agrees well with the surface time evolution of our quasi-decadal mode. To our knowledge, no paper has mentioned how this mode could continue in the deeper ocean layers. Our 3D temperature POP analysis revealed that especially the loading anomaly that recirculates in the eastern branch of the subtropical gyre reaches until the deep ocean layers.

7.6 Conclusions of the North Atlantic Ocean variability in the FESOM setup

In this chapter we show different interannual to decadal variabilities that are present in a normal and random forced COREv2/SODA run of a global FESOM setup that has a local increased resolution in the deep water formation areas. We analyse the variabilities based on the definition of a NADW, STG, SPG and ΔGyre index. The variability in the model can be driven either by: (i) the atmospheric forcing, (ii) internal modes of the ocean or (iii) by superpositions of atmospheric and internal ocean modes. Based on the analysis of the normal and random forced NADW index we identify a quasi-decadal mode, with a periodicity of 14.2 yr that has to be connected to the atmospheric forcing or atmosphere-ocean feedbacks. Further, we identified a 7 yr periodicity that is mainly present in the random forced COREv2/SODA run and so related to a internal mode of the ocean or at least a superposition of internal ocean and atmospheric mode.
We could proof that the model is able to reproduce the variability of the BMT index calculated by *Curry and McCartney* [2001], although the model tends to overestimate the strength of the BMT index.
By employing the POP analysis of a 3D temperature POP field we identify a variety of stable POP modes from which two turned out to be exceptional stable. We show that some of these POP modes are related to westward propagating Rossby waves as well as propagating temperature anomalies in the branch of the Gulf Stream and north Atlantic Current. The 3D POP analysis revealed a stable quasi-decadal mode of 14.1 yr, whose surface patterns agrees well with the quasi-decadal POP modes described by *Deser and Blackmon* [1993] and *Dima and Lohmann* [2004].

AWI Alfred-Wegener-Institut für Polar- und Meeresforschung in der Helmholtz-Gemeinschaft

8 Conclusions and future perspectives

This PhD project targets to model the last five decades of the ocean variability by employing the FESOM model approach to get new insights into to the deep water formation variability as well as into the interdecadal to decadal variability of the internal ocean. For this purpose we took advantage of the unstructured mesh functionality of the FESOM model approach, that allows us to faithfully resolve coastlines and to increase the local resolution in the equatorial and in the deep water formation areas (e.g., Labrador Sea, Greenland Sea, Weddell Sea and Ross Sea) in an otherwise global setup. The key findings of this thesis can be summarized as follows:

- The validation of the model setup used in this thesis revealed that the setup is capable to reproduce large scale features of the ocean circulation as well as the main characteristics of the deep water formation.
  We showed that the sea-ice model produces realistic sea ice concentration on both hemispheres and is able to generate a sea ice variability that is in good agreement with observational data [*Schmith and Hansen*, 2003; *Fetterer et al.*, 2002, updated 2009], although the model tends to slightly underestimate the observed decreasing trend in the Northern Hemispheric sea ice extent.
  On the basis of a comparison with OWS data, we prove that the model setup performs very well in areas with a high resolution. The analysis of the temperature and salinity evolution of the Denmark Strait and Iceland-Scotland Ridge cross section indicates a pronounced variability and a freshening trend of the last four decades in the North Atlantic as its shown in observational data by *Dickson et al.* [2002]. Although the model tends to underestimate absolute strength and salinity of the Nordic Sea overflows. The model features the fingerprint of several GSA events in the vertical that are also documented in observational data by several

authors [*Dickson et al.*, 1988; *Belkin et al.*, 1998; *Belkin*, 2004]. Further the model results have a pronounced variability in the AMOC which is accompanied by a corresponding fluctuation in the deep water formation of the Labrador Sea and Greenland Sea.

- The detailed validation of the deep water formation in the Labrador Sea demonstrates that the model approach used in this thesis is a suitable tool to simulate the spatio-temporal evolution of the layer thicknesses of the LSW mode waters. We show that we are able to model the evolution of LSW indices that is in a good agreement with the observed time series of *Curry et al.* [1998]; *Kieke et al.* [2006, 2007] and *Rhein et al.* [2011]. Based on these indices we present that the Labrador Sea, in our global model setup, can act as a low-pass filter to fluctuations in the NAO index, so that only persistent NAO events correlate with the dLSW index as its mentioned for observational data by *Lazier et al.* [2002].
  Our global model setup confirms the dominance of the atmospheric circulation as one of the main triggers for the variability in the dLSW and uLSW indices, which affects the deep water formation by increased heat loss and by intensified mixing of the Ekman layer. The analysis of the thermal and haline surface density flux indicates that the central Labrador Sea is dominated by the thermal contributions of the surface density flux, while the haline contributions, that are dominated by the effects of sea ice melting, are limited in our model setup to the area of the West Greenland Current and Labrador Current.

- The variability in the model can be driven either by: (i) the atmospheric forcing, (ii) internal modes of the ocean or (iii) by superpositions of atmospheric and internal ocean modes and related feedbacks. Based on the definition of a NADW index for the normal and random forced FESOM run and the analysis of the corresponding spectra we could identify a quasi decadal mode, with a periodicity of 14.2 yr which is connected to the atmospheric forcing. Additionally, we identified a 7 yr periodicity that is mainly present in the random forced COREv2/SODA run and so related to a internal mode or at least a superposition of internal and atmospheric mode.
  By the definition of a model $\Delta Gyre$ index we prove that the model is able to

reproduce the variability of the BMT index calculated from observational data by *Curry and McCartney* [2001]. It shows that the model tends to overestimate the strength of the observational BMT index.

By employing the POP analysis of a 3D temperature POP field we could identify a variety of stable POP modes from which two turned out to be exceptional stable. We show that some of these POP modes are related to an westward propagating Rossby wave as well as propagating temperature anomalies in the branch of the Gulf Stream and North Atlantic Current. The 3D POP analysis revealed a stable quasi decadal mode of 14.1 yr, whose surface patterns agrees well with the quasi decadal POP modes described by *Deser and Blackmon* [1993] and *Dima and Lohmann* [2004].

Outlook

As a next logical step we will use this setup for further studies regarding the deep water formation in Greenland Sea, Irminger Sea and determine their influence on the large-scale ocean circulation.

The FESOM setup introduced in this thesis can be used in conjunction with the 20th century forcing [*Compo et al.*, 2011] to cover the whole period from 1871-2008. This would allow us to study the climate mode variability not just on interdecadal or decadal time-scales, but also on bi-decadal or even longer time-scales. Further, this model setup can be employed for different time slice experiment such as the 6k time slice, which will examine the ocean response to a warmer climate in the North Atlantic ocean. The necessary sea surface forcing data will be provided by ECHAM-T106 simulations, where the FESOM simulations could serve as a dynamical downscaling in sensitive regions.

In order to improve the lateral mixing processes in the deep water formation areas, such as Labrador Sea, one needs to further increase the local resolution to be able to resolve the eddy processes that could affect the deep-water formation in the Labrador Sea [*Eden and Willebrand*, 2001; *Katsman et al.*, 2004], which was beyond the scope of this study.

The 3D POP analysis will be applied to a fully coupled atmosphere ocean general circulation model to test if similar outstanding stable modes, that are related to a

Rossby wave dynamic can be found.

Bibliography

Arakawa, A., and V. R. Lamb, Computational design of the basic dynamical processes of the UCLA general circulation model, *Methods in Computational Physics*, *17*, 173–265, 1977.

Belkin, I., Propagation of the "Great Salinity Anomalies" of the 1990s around the northern North Atlantic, *Geophys. Res. Lett.*, *31*, L08,306, 2004.

Belkin, I., S. Levitus, J. Antonov, and S. Malmberg, "Great Salinity Anomalies" in the North Atlantic, *Prog. Oceanog.*, *41*(1), 1–68, 1998.

Biastoch, A., C. W. Böning, J. Getzlaff, J. M. Molines, and G. Madec, Causes of Interannual-Decadal Variability in the Meridional Overturning Circulation of the Midlatitude North Atlantic Ocean, *J. Climate*, *21*(24), 6599–6615, 2008.

Böning, C. W., F. O. Bryan, W. R. Holland, and R. Döscher, Deep-Water Formation and Meridional Overturning in a High-Resolution Model of the North Atlantic, *J. Phys. Oceanogr.*, *26*(7), 1142–1164, 1996.

Böning, C. W., M. Scheinert, J. Dengg, A. Biastoch, and A. Funk, Decadal variability od subpolar gyre transport and its reverberation in the North Atlantic overturning, *Geophys. Res. Lett.*, *33*, L21S01, 2006.

Boyer, T. P., et al., World Ocean Database 2009. S. Levitus, Ed., NOAA Atlas NESDIS 66, *U.S. Gov. Printing Office, Wash., D.C., 216 pp., DVDs.*, 2009.

Brandt, P., A. Funk, L. Czeschel, C. Eden, and C. W. Böning, Ventilation and Transformation of Labrador Sea Water and Its Rapid Export in the Deep Labrador Current, *J. Phys. Oceanogr.*, *37*(4), 946–961, 2007.

Brauch, J. P., and P. Gerdes, Response of the northern North Atlantic and Arctic oceans to a sudden change of the North Atlantic Oscillation, *J. Geophys. Res.*, *110*, C11,018, 2005.

Broecker, W. S., The great ocean conveyor, *Oceanography*, *4*, 79–89, 1991.

Broecker, W. S., Thermohaline circulation, the archillis heels of our climate system: Will man-made co2 upset the current balance, *Science*, *278*, 1582–1588, 1997.

Bryan, K., and M. D. Cox, The Circulation of the World Ocean: A numerical Study. Part 1, A Homogeneous Model, *J. Phys. Oceanogr.*, *2*, 319–335, 1972.

Bryden, H. L., H. R. Longworth, and S. A. Cunningham, Slowing of the Atlantic meridional overturning circulation at 25° N, *Nature*, *438*, 655–657, 2005.

Campin, J. M., and H. Goose, Parameterization of density-driven downsloping flow for a coarse-resolution ocean model in z-coordinate, *Tellus A*, *51*(3), 412–430, 1999.

Carton, J. A., and B. S. Giese, A Reanalysis of Ocean Climate Using Simple Ocean Data Assimilation (SODA), *Mon. Wea. Rev.*, *136*(8), 2999–3017, 2008.

Cavalieri, D., C. Parkinson, P. Gloersen, and H. J. Zwally, Sea ice concentration from Nimbus-7 SMMR and DMSP SSM/I-SSMIS Passive microwave data, January 1979-June 2006, *National Snow and Data Center, Boulder, CO., USA, (Digital Media)*, 1996, updated 2007.

Chanut, J., B. Barnier, W. Large, L. Debreu, T. Penduff, J. M. Molines, and P. Mathiot, Mesoscale Eddies in the Labrador Sea and Their Contributions to Conversion and Restratification, *J. Phys. Oceanogr.*, *38*(8), 1617–1643, 2008.

Chelton, D. B., and M. G. Schlax, Global Observations of Oceanic Rossby Waves, *Science*, *272*(5259), 234–238, 1996.

Cipollini, P., D. Cromwell, M. S. Jones, G. D. Quartly, and G. Challenor, Concurrent altimeter and infrared observations of Rossby wave propagation near 34°N in the Northeast Atlantic, *Geophys. Res. Lett.*, *24*(8), 889–892, 1997.

Compo, G. P., et al., The Twentieth Century Reanalysis Project, *Quarterly Journal of the Royal Meteorological Society*, *137*(654), 1–28, 2011.

Cromwell, D., Sea surface height observations of the 34°N waveguide in the North Atlantic, *Geophys. Res. Lett.*, *28*(19), 3705–3708, 2001.

Curry, R., and M. S. McCartney, Ocean Gyre Circulation Changes Associated with the North Atlantic Oscillation, *J. Phys. Oceanogr.*, *31*(12), 3374–3400, 2001.

Curry, R., M. S. McCartney, and T. M. Joyce, Oceanic transport of subpolar climate signals to mid-depth subtropical waters, *Nature*, *391*, 575–577, 1998.

Curry, R., B. Dickson, and Y. I., A change in the freshwater balance of the Atlantic Ocean over the past four decades, *Nature*, *426*, 826–829, 2003.

da Costa, E. D., and A. C. de Verdiere, The 7.7-year North Atlantic Oscillation, *Q. J. R. Meteorol. Soc.*, *128*(581), 797–817, 2002.

Danilov, S., G. Kivman, and J. Schröter, A finite element ocean model: principles and evaluation, *Ocean Modell.*, *6*(2), 125–150, 2004.

Danilov, S., G. Kivman, and J. Schröter, Evaluation of an eddy-permitting finite-element ocean model in the North Atlantic, *Ocean Modell.*, *10*(1-2), 35–49, 2005.

de Boyer Montegut, C., G. Madec, A. S. Fischer, A. Lazar, and D. Iudicone, Mixed layer depth over the global ocean: an examination of profile data and a profile-based climatology, *J. Geophys. Res.*, *109*, C12,003, 2004.

Deser, C., and M. L. Blackmon, Surface Climate Variations over the North Atlantic Ocean during Winter: 1900-1989, *J. Climate*, *6*, 1743–1753, 1993.

Dickson, B., I. Yashayaev, J. Meincke, B. Turrell, S. Dye, and J. Holfort, Rapid freshening of the deep North Atlantic Ocean over the past four decades, *Nature*, *416*, 832–837, 2002.

Dickson, R., and J. Brown, The production of North Atlantic deep water: Sources, rates and pathways, *J. Geophys. Res.*, *99*, 12,319–12,341, 1994.

Dickson, R., J. Meincke, S. A. Malmberg, and A. J. Lee, The Great Salinity Anomaly in the Northern North Atlantic 1968-1982, *Prog. Oceanog.*, *20*(2), 103–151, 1988.

Dickson, R., J. Lazier, J. Meincke, P. Rhines, and J. Swift, Long-term coordinated changes in the convective activity of the North Atlantic, *Prog. Oceanog.*, *38*(3), 241–295, 1996.

Dima, M., and G. Lohmann, Fundamental and derived modes of climate variability: concept and application to interannual time-scales, *Tellus A*, *56*(3), 229–249, 2004.

Ding, H., N. S. Keenlyside, and M. Latif, Equatorial Atlantic interannual variability: the role of heat content, *J. Geophys. Res.*, *115*, C09,020, 2010.

Döscher, R., and R. Redler, The Relative Importance of the Northern Overflow and Subpolar Deep convection for the North Atlantic Thermohaline Circulation, *J. Phys. Oceanogr.*, *25*, 1894–1901, 1997.

Eden, C., and J. Willebrand, Mechanism of Interanual to Decadal Variability of the North Atlantic Circulation, *J. Climate*, *14*(10), 2266–2280, 2001.

Edwards, M. O., Global gridded elevation and bathymetry (ETOPO5), Digital raster data on a 5-minute geographic (lat/lon) 2160'4320 (centroid-registered) grid, *NOAA Natl. Geophys. Data Cent., Boulder, Colo.*, 1989.

Eldevik, T., J. E. O. Nilsen, K. Anders Olsson, A. B. Sando, and H. Drange, Observed sources and variability of Nordic seas overflow, *Nature Geosci.*, *2*(6), 406–410, 2009.

Fetterer, F., K. Knowles, W. Meier, and M. Savoie, Sea ice index, *National Snow and Data Center, Boulder, CO. <www.ndsic.org/data/seaice_index/>, (Digital Media)*, 2002, updated 2009.

Fix, G. J., Finite-Element models for ocean circulation problems, *SIAM J. Appl. Math.*, *29*(3), 371–387, 1975.

Ford, R., C. C. Pain, M. D. Piggott, A. J. H. Goddard, C. R. E. de Oliveira, and A. P. Umpleby, A nonhydrostatic finite-element model for three-dimensional stratified oceanic flows. Part I: Model formulation , *Mon. Wea. Rev.*, *132*(12), 2816–2831, 2004.

Gallagher, F., H. von Storch, and G. Schnur, R. Hannoschöck, *The Pop Manual* , Deutsches Klimarechenzentrum, 1991.

Ganachaud, A., Large-scale mass transports, water mass formation, and diffusivities estimated from World Ocean Circulation Experiment (WOCE) hydrographic data, *J. Geophys. Res.*, *108*(C7), 3213, 2003.

Ganachaud, A., and C. Wunsch, Improved estimates of global ocean circulation, heat transport and mixing from hydrographic data, *Nature*, *408*, 453–457, 2000.

Gill, A., *Atmosphere-Ocean Dynamics*, Academic Press, Inc., 1982.

Girton, J. B., and T. B. Sanford, Synoptic sections of the Denmark Strait Overflow, *Geophys. Res. Lett.*, *28*(8), 1619–1622, 2001.

Griffies, S. M., et al., Coordinated Ocean-ice Reference Experiments (COREs), *Ocean Modelling*, *26*(1-2), 1–46, 2009.

Haak, H., J. Jungclaus, and M. Latif, Formation and propagation of great salinity anomalies, *Geophys. Res. Lett.*, *30*(9), 1473, 2003.

Häkkinen, S., Freshening of the Labrador Sea surface waters in the 1990s: Another great salinity anomaly?, *Geophys. Res. Lett.*, *29*(24), 2232, 2002.

Häkkinen, S., and P. B. Rhines, Decline of subpolar North Atlantic circulation during the 1990s, *Science*, *304*(5670), 555–559, 2004.

Hasselmann, K., PIPs and POPs: The Reduction of Complex Dynamical Systems Using Principal Interaction and Oscillation Patterns, *J. Geophys. Res.*, *93*(D9), 11.015–11.021, 1988.

Hatun, H., A. B. Sando, H. Drange, B. Hansen, and H. Valdimarsson, Influence of the Atlantic Subpolar Gyre on the Thermohaline Circulation, *Science*, *309*(16), 1841–1844, 2005.

Huang, B., Y. Xue, A. Kumar, and D. W. Behringer, AMOC variations in 1979-2008 simulated by NCEP operational ocean data assimilation system, *Clim. Dyn.*, *38*(3-4), 513–525, 2012.

Hurrell, J. W., Decadal Trends in the North Atlantic Oscillation: Regional Temperatures and Precipitation, *Science*, *269*(5224), 676–679, 1995.

Johnson, S. D., D. S. Battisti, and E. S. Sarachik, Seasonality in an Empirically Derived Markov Model of Tropical Pacific Sea Surface Temperature Anomalies, *J. Climate*, *13*(18), 3327–3335, 2000.

Josey, S. A., Changes in the heat and freshwater forcing of the eastern Mediterranean and their influence on deep water formation, *J. Geophys. Res.*, *108*(C7), 3237, 2003.

Katsman, C. A., M. A. Spall, and R. S. Pickard, Boundary Current Eddies and their Role in the Restratification of the Labrador Sea, *J. Phys. Oceanogr.*, *34*(9), 1967–1983, 2004.

Katz, E. J., Equatorial Kelvin Waves in the Atlantic, *J. Geophys. Res.*, *92*(C2), 1849–1898, 1987.

Kieke, D., M. Rhein, L. Stramma, W. M. Smethie, D. A. Lebel, and W. Zenk, Changes in the CFC Inventories and Formation Rates of Upper Labrador Sea Water, 1997-2001, *J. Phys. Oceanogr.*, *36*(1), 64–86, 2006.

Kieke, D., M. Rhein, L. Stramma, W. M. Smethie, D. A. Lebel, and W. Zenk, Changes in the pool of Labrador Sea Water in the subpolar North Atlantic, *Geophys. Res. Lett.*, *34*, L06,605, 2007.

Killworth, P. D., D. B. Chelton, and R. A. de Szoeke, The Speed of Observed and Theoretical Long Extratropical Planetary Waves, *J. Phys. Oceanogr.*, *27*(9), 1946–1966, 1997.

Kuhlbrodt, T., A. Griesel, M. Montoya, A. Levermann, M. Hofmann, and S. Rahmsdorf, On the driving processes of the Atlantic Meridional Overturning Circulation, *Rev. Geophys.*, *45*, RG2001, 2007.

Kwok, R., and D. A. Rothrock, Variability of Fram Strait ice flux and North Atlantic Oscillation, *J. Geophys. Res.*, *104*(C3), 5177–5189, 1999.

Large, W. G., and S. G. Yeager, The global climatology of an interannually varying air-sea flux data set, *Clim. Dyn.*, *32*(2), 341–364, 2008.

Large, W. G., and S. G. Yeager, The global climatology of an interannually varying air-sea flux data set, *Clim. Dyn.*, *33*(2-3), 341–364, 2009.

Latif, M., C. Böning, J. Willebrand, A. Biastoch, J. Dengg, N. Keenlyside, and U. Schweckendier, Is the Thermohaline Circulation Changing ?, *Geophys. Res. Lett.*, *19*(18), 4631â4637, 2006.

Lazier, J., R. Hendry, A. Clarke, I. Yashayaev, and R. Rhines, Convection and restratification in the Labrador Sea, 1990-2000, *Deep-Sea Research I*, *49*(10), 1819–1835, 2002.

Lazier, J. R. N., Oceanographic conditions at Ocean Weather Ship Bravo, 1964-1974, *Atmosphere-Ocean*, *18*(3), 227–238, 1980.

Levitus, S., J. I. Antonov, and T. P. Boyer, Interannual Variability of Temperature at a Depth of 125 Meters in the North Atlantic Ocean, *Science*, *266*(5182), 96–99, 1994.

Lohmann, G., H. I. Haak, and J. H. Jungclaus, Estimating trends of Atlantic meridional overturning circulation from long-term hydrographic data and model simulations, *Ocean Dynamic*, *58*(2), 127–138, 2008.

Lohmann, K., H. Drange, and M. Bentsen, Response of the North Atlantic subpolar gyre to persistent North Atlantic oscillation like forcing, *Clim. Dyn.*, *32*(2-3), 273–285, 2009.

Macrander, A., U. Send, H. Valdimarsson, S. Jonsson, and R. H. Käse, Interannual changes in the overflows from the Nordic Seas into Atlantic Ocean through Denmark Strait, *Geophys. Res. Lett.*, *32*, L06,606, 2005.

Macrander, A., R. H. Käse, U. Send, H. Valdimarsson, and S. Jonsson, Spatial and temporal structure of the Denmark Strait Overflow revealed by acoustic observations, *Ocean Dynamics*, *57*, 75–89, 2007.

Mann, M. E., and J. Park, Global-scale modes of surface temperature variability on interannual to century timescales, *J. Geophys. Res.*, *99*(D12), 25,819–25,833, 1994.

Marshall, J., and F. Schott, Open-ocean convection: observations, theory, and models, *Review of Geophysics*, *37*, 1–64, 1999.

Meier, W., F. Fetterer, K. Knowles, M. Savoie, and M. J. Brodzik, Sea ice concentration from Nimbus-7 SMMR and DMSP SSM/I passive microwave data, July-December 2006, *National Snow and Data Center, Boulder, CO., USA, (Digital Media)*, 2006, updated 2007.

Moron, V., R. Vautard, and M. Ghil, Trends, interdecadal and interannual oscillations in global sea-surface temperature, *Clim. Dyn.*, *14*(7-8), 545–569, 1998.

Park, W., and M. Latif, Pacific and Atlantic multidecadal variability in the Kiel Climate Model, *Geophys. Res. Lett.*, *37*, L24,702, 2010.

Pickart, R. S., M. A. Spall, and J. R. Lazier, Mid-depth ventilation in the western boundary current system of the sub-polar gyre, *Deep Sea Research Part I*, *44*(6), 1025–1054, 1997.

Pickart, R. S., D. J. Torres, and R. A. Clarke, Hydrography of the Labrador Sea during Active Convection, *J. Phys. Oceanogr.*, *32*(2), 428–456, 2002.

Pickart, R. S., F. Straneo, and G. W. K. Moore, Is Labrador Sea Water formed in the Irminger Sea ?, *Deep-Sea Research Part 1*, *50*(1), 23–52, 2003.

Rahmsdorf, S., On the freshwater forcing and transport of the Atlantic thermohaline circulation, *Clim. Dyn.*, *412*, 799–811, 1996.

Rhein, M., J. Fischer, W. M. Smethie, D. Smythe-Wright, R. F. Weiss, C. Mertens, D. H. Min, U. Fleischmann, and A. Putzka, Labrador Sea Water: pathways, CFC-inventory and formation rates, *J. Phys. Oceanogr.*, *32*(2), 648–665, 2002.

Rhein, M., D. Kieke, S. Hüttl-Kabus, A. Roessler, C. Mertens, R. Meissner, B. Klein, C. W. Böning, and I. Yashayaev, Deep water formation, the subpolar gyre, and the meridional overturning circulation in the subpolar North Atlantic, *Deep-Sea Research II*, *58*(17-18), 1819–1832, 2011.

Sarafanov, A., A. Falina, H. Mercier, P. Lherminier, and A. Sokov, Recent changes in the Greenland-Scotland overflow-derived water transport from hydrographic observations in the southern Irminger Sea, *Geophys. Res. Lett.*, *36*, L13,606, 2009.

Schlosser, P., G. Bönisch, M. Rhein, and R. Bayer, Reduction of Deepwater Formation in the Greenland Sea During the 1980s: Evidence from Tracer Data, *Science*, *251*(4997), 1054–1056, 1991.

Schmith, T., and C. Hansen, Fram Strait Ice Export during the Nineteenth and Twentieth Centuries Reconstructed from a Multiyear Sea Ice Index from Southwestern Greenland, *J. Climate*, *16*(16), 2782–2791, 2003.

Scholz, P., G. Lohmann, Q. Wang, and S. Danilov, Validation of a Finite-Element Sea-Ice ocean model (FESOM) setup to study the interannual to decadal variability in the deep-water formation rates, *Ocean Dynamic*, submitted, 2012.

Sidorenko, D., S. Danilov, Q. Wang, A. Huerta-Casas, and J. Schröter, On computing transports in finite-element models, *Ocean Modelling*, *28*(1-3), 60–65, 2009.

Sidorenko, D., Q. Wang, S. Danilov, and J. Schröter, FESOM under coordinated ocean-ice reference experiment forcing, *Ocean Dynamic*, *61*(7), 881–890, 2011.

Stephens, C., J. I. Antonov, T. P. Boyer, M. E. Conkright, R. A. Locarnini, T. D. OBrien, and H. E. Garcia, *World Ocean Atlas 2001, Volume 1: Temperature. S. Levitus, Ed.*, NOAA Atlas NESDIS 49, U.S. Government Printing Office, Wash., D.C., 167 pp., CD-ROMs., 2002.

Stewart, R. H., *Introduction to Physical Oceanography*, Department of Oceanography Texas A and M University, 2008.

Stramma, L., D. Kieke, M. Rhein, F. Schott, I. Yashayaev, and K. P. Koltermann, Deep water changes at the western boundary of the subpolar North Atlantic during 1996 to 2001, *Deep-Sea Research I*, *51*(8), 1033–1056, 2004.

Timmermann, R., S. Danilov, J. Schröter, C. Böning, D. Sidorenko, and K. Rollenhagen, Ocean circulation and sea ice distribution in a finite element global sea ice-ocean model, *Ocean Modelling*, *27*(3-4), 114–129, 2009.

von Storch, H., and G. Hannoschöck, Comments on "Empirical orthogonal function-analysis of wind vectors over the tropical Pacific region", *Bull. Amer. Meteor. Soc.*, *65*, 162, 1984.

von Storch, H., and F. W. Zwiers, *Statistical Analysis in Climate Research*, Cambridge University Press, 2003.

von Storch, H., G. Bürger, R. Schnur, and J. S. von Storch, Principal Oscillation Patterns: A Review, *J. Climate*, *8*(3), 377–400, 1995.

Walker, G. T., and E. W. Bliss, World weather V , *Mem. Roy. Met. Soc*, *4*, 53–84, 1932.

Wang, Q., S. Danilov, and J. Schröter, Finite Element Ocean Circulation Model based on triangular prismatic elements, with application in studying the effect of topography representation, *J. Geophys. Res.*, *113*, C05,015, 2008a.

Wang, Q., S. Danilov, and J. Schröter, Comparison of overflow simulations on different vertical grids using the Finite Element Ocean circulation Model, *Ocean Modelling*, *20*(4), 313–335, 2008b.

Warren, B. A., and C. Wunsch, *Deep circulation of the world ocean, in Evolution of physical oceanography, chapter 1*, 6-41 pp., Massachusetts Institute of Technology: MIT Open Course Ware, 2007.

Weisse, R., U. Mikolajewicz, and E. Maier-Reimer, Decadal variability of the North Atlantic in an ocean general circulation model, *J. Geophys. Res.*, *99*(C6), 12,411–12,421, 1994.

White, L., E. Deleersnijder, and V. Legat, A three-dimensional unstructured mesh finite element shallow-water model, with application to the flows around an island and in a wind-driven, elongated basin, *Ocean Modelling*, *22*(1-2), 26–47, 2008.

WOCE Data Product Committee, WOCE Global Data, Version 3.0, WOCE International Project Office, WOCE Report No. 180/02, Southampton, UK, 2002.

Wu, P., R. Wood, and P. Stott, Does the recent freshening trend in the North Atlantic indicate a weakening thermohaline circulation?, *Geophys. Res. Lett.*, *31*, L02,301, 2004.

Yashayaev, I., Hydrographic changes in the Labrador Sea, 1960-2005, *Prog. Oceanog.*, *73*(3-4), 242–276, 2007.

Yashayaev, I., and W. Loder, Enhanced production of Labrador Sea Water in 2008, *Geophys. Res. Lett.*, *36*, L01,606, 2009.

Yashayaev, I., M. Bersch, and H. M. van Aken, Spreading of the Labrador Sea Water to the Irminger and Iceland basins, *Geophys. Res. Lett.*, *34*, L10,602, 2007a.

Yashayaev, I., H. M. van Aken, N. P. Holliday, and M. Bersch, Transformation of the Labrador Sea Water in the subpolar North Atlantic, *Geophys. Res. Lett.*, *34*, L22,605, 2007b.

Zhang, R., T. L. Delworth, A. Rosati, W. G. Anderson, K. W. Dixon, H. C. Lee, and F. Zeng, Sensitivity of the North Atlantic Ocean Circulation to an abrupt change in the Nordic Sea overflow in a high resolution global coupled climate model, *J. Geophys. Res.*, *116*, C12,024, 2011.

AWI Alfred-Wegener-Institut für Polar- und Meeresforschung in der Helmholtz-Gemeinschaft

Acknowledgements

First, I would like to thank my supervisor Prof. Dr. Gerrit Lohmann for giving me the opportunity to perform the PhD study in his research group. I am very thankful for his continuous support and guidance throughout my PHD study and his helpful expert advice.

Many thanks to Dr. Qiang Wang and Dr. Sergey Danilov for their participation in my PhD committee and there invaluable help with the FESOM model and sharing their great expertise with me.

Many thanks to Prof. Dr. Monica Rhein and Dr. Dagmar Kieke for their fruitful suggestions and comments. I also want to thank my colleagues from the Paleoclimate Dynamic group, for the inspiring working environment.

I am infinitely grateful to my wife Monica, for discussing, reading and correcting my thesis. Without her continuous moral support, encouragement and love i could have never completed this dissertation. I am also grateful to my little daughter Alessia, which motivated me with her enduring smile and love. This PhD thesis is dedicated to both of them. Finally I am thankful to the rest of my family for their patience and moral support.